Hydrodynamic transport and viscous flow in ultra-high mobility Corbino rings

Sujatha Vijayakrishnan

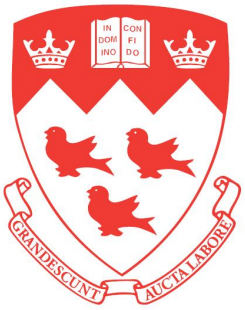

Department of Physics

McGill University

Montréal, Québec, Canada

December 2024

First published on December 5, 2025

A thesis submitted to McGill University in partial fulfilment of the requirements of the degree of Doctor of Philosophy

To my Amma, You have been my unwavering support, my rock, and my confidante throughout this journey. Your patience, love, and encouragement have carried me through the late nights, the doubts, and the challenges. For every sacrifice you made, and for every silent prayer you offered, I dedicate this thesis to you.

Acknowledgements

First and foremost, I would like to express my gratitude to my supervisor, Prof. Guillaume Gervais, whose guidance and expertise have been instrumental in completing this thesis. I appreciate the numerous opportunities you have provided me to grow as a young and aspiring researcher. I enjoyed every minute I spent in the Lab, which has strengthened my skills. I am confident that these experiences will be immensely beneficial in facing any future challenges.

I want to express my gratitude to Prof. Thomas Szkopek for his invaluable insights and collaboration during this project's pivotal moments. I also thank Dr. Mike Lilly (Sandia National Lab) and Dr. Lloyd W. Engel (National High Magnetic Field Laboratory) for their invaluable contributions through effective discussions and comments, which helped in significantly improving our work. I sincerely thank Dr. L. N. Pfeiffer and K. W. West for providing the high-quality wafers essential to my experiments.

Thank you, Zachary Berkson-Korenberg, for your dedication to this project, mastering it within a year and performing the numerical simulations that helped confirm the conclusion. I hope this work lays a strong foundation for your PhD—best of luck! To my lab mates and friends—Frederik Poitevin, Matei Petrescu, Talia Martz-Oberlander, Oulin Yu, Frédéric Boivin, Renée Goodman, Nick Wicklund, and Dawson Willerton, thank you for your friendship and support, which made tough days bearable. I also appreciate the contributions of the undergraduate students, especially Justin Mainville, for his early work on numerical simulations.

Special thanks to Frederik Poitevin for sharing the Triton system and making long measurement days more enjoyable during the pandemic, Matei for your invaluable mentorship, Talia for your guidance during my onboarding, and Frédéric Boivin for your insightful thesis and paper reviews, which greatly improved my work.

I would like to express my gratitude to John Smeros, Richard Talbot, Robert Gagnon, and Juan Gallego for their invaluable technical support. I also appreciate Pascal Bourseguin and the entire physics department at McGill for enriching my research experience and making my time here enjoyable. Keyan, thank you for believing in me and supporting my journey from India to Canada. Your guidance in device fabrication and foundational teachings have been essential to my research.

To my cherished friends, Quinn, Riya, Mohit, Sreelakshmi, Arya, Vishnunarayanan, and Vijith, my support system and the treasures I found in my 20s—thank you for your unwavering encouragement and for always being there for me. To my Dad, I hope I make you proud and I know you are looking out for me from above. Lastly, to my mother and brother, who are living just for me, I owe everything to you. Your endless love, sacrifices, and belief in me have been the driving force behind all my achievements. This journey would have been impossible without your support, and I dedicate this work to you both.

This thesis is not just the result of my work, but the collective effort, love, and support of all of you. I am forever grateful.

Abstract

Hydrodynamic transport in Fermi liquids has recently garnered significant attention in condensed matter physics. This intriguing phenomenon, which relates electron transport to that of a collective fluid flow, was theorized by Gurzhi in 1963. To achieve hydrodynamic transport, momentum-conserving electron-electron ($e-e$) interactions must dominate over all other momentum-relaxing (MR) scattering mechanisms, such as scattering due to impurities or phonons. This sets a strict requirement of exceptionally high electron mobility for the material, a factor that historically posed significant challenges for the experimental observation of hydrodynamic transport. However, advancements in the growth of ultra-high mobility heterostructures, particularly GaAs/AlGaAs heterostructures, with large MR scattering lengths on the order of ~ 350 μm have enabled exploration of the hydrodynamic regime.

In this thesis, we investigate hydrodynamic electron transport in GaAs/AlGaAs two-dimensional electron gas systems (2DEGs) with mobilities exceeding 20×10^6 cm^2/Vs. Local and nonlocal transport measurements were performed on two multi-ring Corbino devices with different electron densities. The strength of electron-electron ($e-e$) interactions, often indicated by the interaction parameter r_s, is inversely proportional to the electron density. The lower-density sample exhibited non-monotonic temperature dependence of resistance with a sharp decrease of resistance above 500 mK akin to Gurzhi's prediction, while the higher-density sample showed contrasting behaviour. In the nonlocal configuration, a negative potential consistent with hydrodynamic flow was observed in the lower-density sample,

but not in the higher-density sample.

These experimental results, supported by numerical simulations of the Navier-Stokes equations, suggest the presence of hydrodynamic transport at temperatures below 1 K in the lower-density sample. The anomalous electronic transport behaviour observed in the higher-density sample remains an open question that warrants further investigation. These findings highlight the significance of $e - e$ interactions and offer new insights into electron transport in high-mobility 2DEGs.

Abrégé

Le transport hydrodynamique dans les liquides de Fermi a récemment fait l'objet d'une attention particulière en physique de la matière condensée. Ce phénomène intriguant, qui associe le transport d'électrons à l'écoulement collectif d'un fluide, a été proposé par Gurzhi en 1963. Pour obtenir le régime hydrodynamique, les interactions électron-électron ($e-e$) conservant la quantité de mouvement doivent dominer tous les autres mécanismes de diffusion non conservatifs (MR), tels que la diffusion causée par les impuretés ou les phonons. Cela impose au matériau de posséder une mobilité électronique exceptionnellement élevée, un facteur qui, historiquement, a posé des problèmes importants pour l'observation expérimentale du transport hydrodynamique. Toutefois, les progrès réalisés dans la croissance d'hétérostructures à mobilité ultra-élevée, en particulier les hétérostructures de GaAs/AlGaAs, avec de grandes longueurs de diffusion MR de l'ordre de ~ 350 μm ont permis d'explorer le régime hydrodynamique.

Dans cette thèse, nous étudions le transport hydrodynamique des électrons dans les systèmes de gaz d'électrons bidimensionnels (2DEGs) basés sur des hétérostructures de GaAs/AlGaAs ayant des mobilités dépassant 20×10^6 cm^2/Vs. Des mesures de transport locales et non locales ont été effectuées sur deux dispositifs de type Corbino à anneaux multiples ayant des densités d'électrons distinctes. L'intensité des interactions électron-électron ($e-e$), souvent dénotée par le paramètre d'interaction r_s, est inversement proportionnelle à la densité électronique. L'échantillon à faible densité présente une dépendance non monotone de la résistance en fonction de la température, avec une forte diminution de la résistance au-dessus de 500 mK, ce qui

s'apparente à la prédiction de Gurzhi, tandis que l'échantillon à densité plus élevée présente un comportement opposé. Dans la configuration non locale, un potentiel négatif expliqué par un écoulement hydrodynamique a été observé dans l'échantillon à faible densité, mais est absent dans l'échantillon à densité plus élevée.

Ces résultats expérimentaux, soutenus par des simulations numériques des équations de Navier-Stokes, suggèrent la présence d'un transport hydrodynamique à des températures inférieures à 1 K dans l'échantillon de faible densité. Le comportement distinct du transport électronique observé dans l'échantillon à plus haute densité reste une question ouverte qui requiert une étude plus approfondie. Ces résultats soulignent l'importance des interactions $e - e$ et offrent de nouvelles perspectives sur le transport des électrons dans les 2DEG à haute mobilité.

Contributions and Statement of Originality

This thesis represents the author's original and substantial contribution to the field of experimental condensed matter physics. The work has not been submitted for any other degree or diploma at any institution. It is a manuscript-based thesis, with Chapters 3 and 4 comprising manuscripts where the author is the first author and co-first author, respectively. The specific contributions made by the author to each work are outlined in detail below.

— *Apparatus:* The results presented in Chapters 3 and 4 were conducted in two different dilution refrigerator systems. One from Bluefors and another from Oxford Instruments. I was fortunate to benefit from the prior installation and calibration of the measurement apparatus, including the dilution refrigerator, magnet, experimental tail, and instrumentation. Matei Petrescu (MP) handled this for the Bluefors system, while Frederik Poitevin (FP) did so for the Oxford unit. The author, SV, made minor modifications to the low and room-temperature wiring.

— *Fabrication of Corbino and van der Pauw devices:* Dr. L.N. Pfeiffer and K.W. West, collaborators of Prof. Guillaume Gervais (GG), provided the high-mobility wafers for this project. Two van der Pauw (VdP) samples presented in this thesis were fabricated by SV. The Gervais Lab had prior expertise in Corbino geometry from other projects. Keyan Bennaceur (KB), together with Simon Bilodeau (SB), fabricated the single-ring Corbino samples shown in Appendix

A. KB also fabricated one of the multi-terminal devices, while SV fabricated the other under KB's guidance.

— *Anomalous local electronic transport:* Chapter 3 is based on the published manuscript *Anomalous electronic transport in high-mobility Corbino rings, S. Vijayakrishnan, F. Poitevin, O. Yu, Z. Berkson-Korenberg, M. Petrescu, M. P. Lilly, T. Szkopek, K. Agarwal, K. W. West, L. N. Pfeiffer, and G. Gervais, Nat. Commun.* ***14****, 3906 (2023)*, where SV is the first author. The devices were fabricated by SV, and all measurements were performed by SV at low temperatures using the dilution refrigerator system set up by MP and FP, whose expertise in low-temperature measurements was invaluable. KWW and LNP provided the ultra-high mobility wafers. OY contributed expertise in signal noise reduction. SV conducted the data analysis, with ZBK assisting in developing specific computer routines and maintaining the data collection software (LabGUI), originally written by Benjamin A. Schmidt (BAS) and Pierre-François Duc (PFD). MPL and TS provided key insights into semiconductor measurements and the interpretation of results. KA offered theoretical guidance. The manuscript and supplementary material were written by GG and SV, and all other authors commented on it.

— *Nonocal electronic transport and Numerical simulation:* Chapter 4 is based on the manuscript *Two-dimensional hydrodynamic viscous electron flow in annular Corbino rings, S. Vijayakrishnan, Z. Berkson-Korenberg, J. Mainville, L. W. Engel, M. P. Lilly, K. W. West, L. N. Pfeiffer, and G. Gervais, arXiv:2405.17588 (2024)*, which is currently under review, with SV as the first co-author. The manuscript reflects an equal contribution from both experimental and theoretical efforts. The concept of nonlocal transport was formulated by GG, and SV fabricated all devices and performed the measurements. The initial experimental discussion and interpretation of results, supported by the hydrodynamic reciprocity theorem, were conducted by GG and SV, leading to the results presented in Figures 1 and 2. The theoretical aspect, including device modeling and numerical simulations of the Navier-Stokes equation, was

performed by ZBK, whose work was essential for interpreting and concluding the results in this thesis. JM contributed to the initial background study on numerical analysis. Insightful discussions with LWE and MPL further aided in interpreting the results. The manuscript and supplementary material were co-written by SV, ZBK, and GG, with all other authors providing comments.

— *Hydrodynamic transport:* The conceptualization and experimental proposal of this project was by the author's supervisor, Guillaume Gervais (GG), along with the author (SV). The transport measurements that led to the discovery of anomalous transport in ultra-high 2DEG and the discovery of the signatures of hydrodynamic transport were conducted by SV with the guidance of GG. Significant contributions to the study of condensed matter physics include:

  — A novel experimental realization of hydrodynamic transport below 1 K.

  — Discovery of nonlocal potential in a radially confined geometry due to viscous flow.

Table des matières

Table des figures

List of Abbreviations

2DEG Two-dimensional electron gas.

DOS Density of states.

HEMT High electron mobility transistor.

IQHE Integer quantum Hall effect.

LL Landau level.

MBE Molecular beam epitaxy.

MC Momentum-conserving.

MR Momentum-relaxing.

MOSFET Metal-oxide semiconductor field-effect transistor.

QHE Quantum Hall effect.

QHS Quantum Hall state.

QW Quantum well.

SdH Shubnikov-de Haas.

VdP Van der Pauw.

1

Introduction

Hydrodynamic transport, a subset of fluid dynamics, is based on the relaxation of conserved fundamental quantities such as charge, mass, and momentum to a local equilibrium. Initially, the term hydrodynamics primarily referred to the dynamics of water flow. However, it now encompasses the extensive study of hydrodynamic transport in strongly correlated charged systems [1], phonons [2], and magnons [3] within condensed matter physics, as well as applications to electronic systems [4–13]. In the 1960s, scientists explored hydrodynamic transport descriptions for Fermi liquids such as in ^{3}He [14, 15] below 100 K, where particle interaction conserves momentum. However, studying similar behaviour in electronic systems proved to be more complex due to additional factors such as impurities and vibrations within the material. In 1960, the renowned Russian physicist R. N. Gurzhi predicted that under certain length scale conditions, the resistance in a material would decrease and reach a minimum with increasing temperature rather than the expected monotonic

behaviour. This indicates the presence of hydrodynamic transport, a phenomenon now known as the Gurzhi effect [16]. Creating the conditions necessary to observe this effect was challenging for a long time. However, recent advancements in materials science have made it possible.

This thesis focuses on the discovery and confirmation of hydrodynamic transport in ultra-high mobility two-dimensional electron gas systems (2DEGs) formed in the Corbino geometry fabricated on a GaAs/AlGaAs heterostructure. It emphasises the significance of selecting an ultra-clean material, choosing a suitable device geometry, conducting sensitive low-temperature transport measurements, and interpreting the experimental results in light of different length scales. We also explore the analytical solutions of the Navier-Stokes equations, as well as their numerical simulations, which were performed in collaboration with another member of the Gervais lab.

1.1 Thesis Outline

Chapter 2 provides the theoretical foundation for understanding hydrodynamic transport in 2DEGs. It covers the basic knowledge of ultra-high mobility 2DEGs, and phenomena such as the Shubnikov-de Haas oscillations, Hall effects, and quantum Hall effects are discussed. This chapter also explores measurement geometries and transport regimes and introduces electron hydrodynamics. It links these concepts to the study of an intriguing property known as Hall viscosity.

Chapter 3 presents the local transport study of electron hydrodynamics, as detailed in the published manuscript *"Anomalous Electronic Transport in High-Mobility Corbino Rings"* [17]. This chapter discusses the observation of non-monotonic resistance behaviour with increasing temperature and provides a detailed discussion of a possible Gurzhi effect.

Chapter 4 presents a further study of hydrodynamic electron transport based on

the manuscript *"Two-Dimensional Hydrodynamic Viscous Electron Flow in Annular Corbino Rings"* [18]. This chapter presents findings from both local and nonlocal measurements, it discusses the concept of electron viscosity and compares experimental data with Navier-Stokes simulation that corroborates the hydrodynamic behaviour observed in our 2DEG Corbino Samples.

Finally, I will conclude with Chapter 5 by offering a detailed discussion and summary of the work presented in this thesis and I will set the stage for possible future experiments based on the achievements of this thesis.

2

Theory and Background

This chapter will provide an in-depth overview of the key concepts used in the next chapters. We will begin by unravelling the intricacies of 2DEGs, with a particular focus on those based on GaAs/AlGaAs heterostructures. Then, we will review the effects of a magnetic field on a 2DEG system, including the Hall effect and Shubnikov-de Haas (SdH) oscillations. We will also discuss three different transport geometries, two of which were utilized in this work. The subsequent sections of this chapter will introduce electron hydrodynamics and the current state of the art on this topic.

2.1 Two-dimensional Electron Gas

The original method for creating 2DEG systems, pioneered by Shockley and Pearson in 1948, laid the foundation for metal-oxide-semiconductor field-effective

transistor (MOSFET) technology. Even though the first proposal of this technology dates from the 1930s [19], the first silicon MOSFET was developed in the 1960s [20,21]. This MOSFET technology utilizes an electric field to confine the electrons to reside at the interface of silicon and the impenetrable insulating silicon oxide as shown in Fig. 2.1a. This results in the electron being confined to a plane, making it an ideal implementation of the concept of a 2DEG system. Limitations of MOSFETs, such as undesired scattering of electrons due to the surface roughness, obscure the observation of a clean behaviour under the magnetic field. These limitations are resolved by creating a heterostructure of semiconductors : heterogeneous semiconductor structures made out of multiple semiconductors. The significant advancement in heterostructures occurred with the introduction of molecular beam epitaxy (MBE) as a practical crystal growth technology in the 1960s by Al Cho at Bell Laboratories. This development laid the foundation for a large industry manufacturing high-performance photonic and electronic devices. These semiconductor structures utilize the band gap energy, and by modifying the Fermi levels either by doping or by applying an electric field, we can tune the conduction from being hole-dominated to charge neutral to electron-dominated.

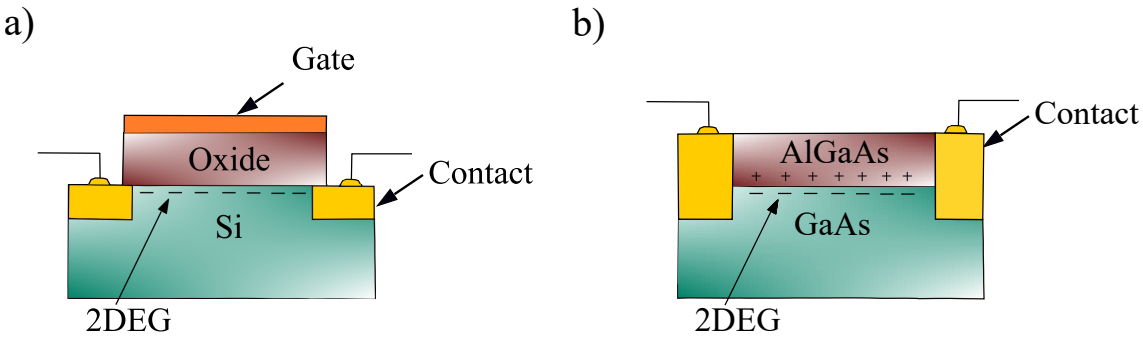

FIGURE 2.1 – Schematics of silicon metal-oxide-semiconductor field-effect transistors (MOSFETs) and modulation-doped GaAs/AlGaAs heterojunction. a) Two-dimensional electron system (2DES) formed at the interface between silicon and silicon oxide due to the electric field generated by the gate. The panel b) shows 2DES at the interface between GaAs and AlGaAs. Here, electrons are confined near the AlGaAs by the electric field from charged silicon dopants within the AlGaAs layer.

Our research focuses on a heterostructure formed by GaAs/AlGaAs. The 2DEG

in the MBE-grown GaAs/AlGaAs structure is located at the GaAs side of the interface Fig. 2.1b. During the heterostructure growth process, silicon (Si) impurities are introduced into the AlGaAs side [22]. This technique is known as modulation doping and was first introduced by Störmer *et al.* in 1978 [23], marking a turning point in semiconductor physics. The additional electrons in Si atoms become free and move to the lowest energy state, crossing the energy barrier and reaching the GaAs material. The electric fields generated by this migration are potent enough to induce band bending in the GaAs layer of the junction. At reduced temperatures, the stationary positively charged silicon ion (due to the loss of an extra electron) pulls the mobile electron through the AlGaAs barrier, thereby quantum mechanically binding the carrier to the interface. As a result, it allows the electrons to remain mobile in the $x - y$ plane [24]. In this case, it creates a triangular potential, forming the electron's confinement region, which is very narrow on the z-axis but only constrained by the boundaries of the sample in the x and y directions. This region is known as a quantum well (QW). The specific characteristics of each 2DEG are contingent on the particular growth conditions and can exhibit considerable variation across different samples.

2.1.1 Ultra-high Mobility 2DEG

Modulation doping led to the invention of high electron mobility transistors (HEMT) and the continuous improvement in electron mobility of 2DEG [25–36] has been instrumental in the experimental progress of quantum physics. This ranges from everyday field-effect transistors (FET) to probing more intricate quantum phenomena such as the quantum Hall effect, which we will discuss in the upcoming sections. Fig. 2.2 shows some of the 2DEG mobility landmarks, annotated with the specific innovation in MBE.

The quality of the 2DEG system is often assessed as a function of the mobility of the charge carrier (in our case, electrons are the charge carriers). In the Drude

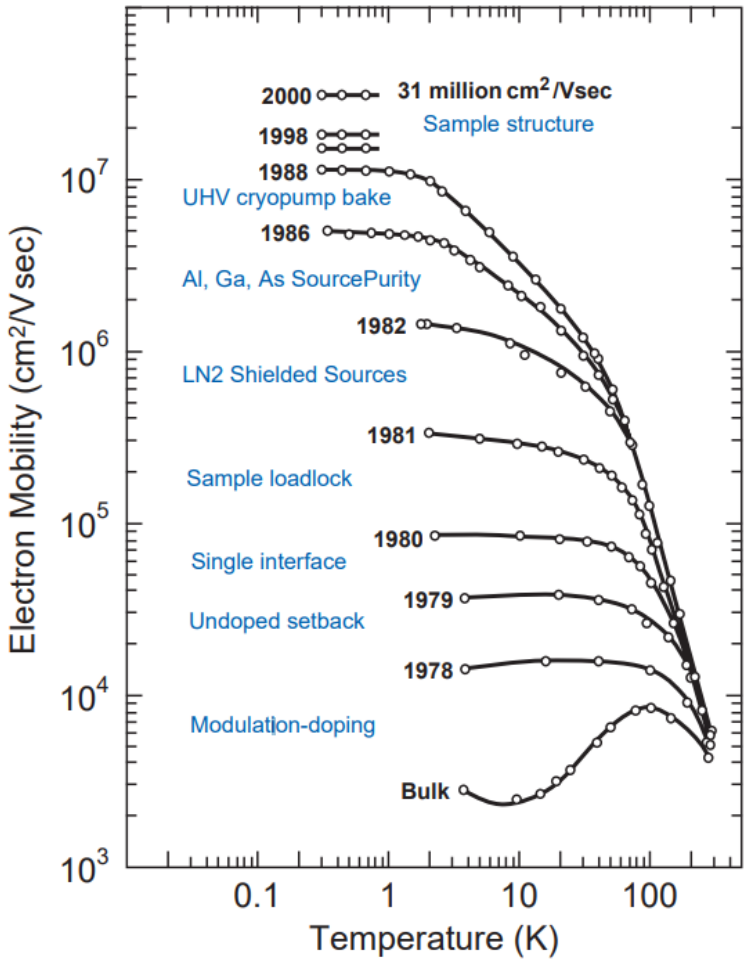

FIGURE 2.2 – The figure shows a historical overview of advancements in electron mobility in GaAs, highlighting the technical innovations that contributed to these improvements. The figure is from reference [37] and used with permission.

model, the electron mobility is given by

$$\mu = \frac{e\tau_{MR}}{m^*}, \tag{2.1}$$

where e is the fundamental electron charge, $m^* = 0.067m_e$ (for GaAs) is the effective mass of the electrons in terms of electron mass m_e, and τ_{MR} is the momentum-relaxing (MR) lifetime that represents the time an electron can travel before it undergoes a collision with impurities/defects or phonons. As we see in Eq. 2.1, mobility is directly affected by the scattering time. This scattering time τ_{MR} can be considered as a 'holistic' scattering time, which by Matthiessen rule can be represented

as,

$$\frac{1}{\tau_{MR}} = \sum \frac{1}{\tau_i}, \tag{2.2}$$

where each τ_i represents the scattering time of each momentum relaxing scattering event. Two main scattering events arising from the heterostructure are the residual background and the remote ionized impurity scattering. A finite amount of residual background impurities is unavoidable in a sample unless one has 100% pure material and the heterostructure is grown in an absolute vacuum with perfectly inert heating sources and chamber components. These residual impurities will act as scattering centres, and their effect on mobility depends on their distance from the QW, meaning this will increase scattering and lower the mobility.

The second scattering mechanism arises due to the remote ionized Si impurities used for creating a 2DEG system in the modulation doping technique. These are essential in forming an ultra-high mobility sample. The impurities are introduced in a δ function-like manner [38–41] at a certain distance called *setback distance*. This setback distance plays a role in determining the carrier density of a 2DEG device, and hence, density plays a vital role in determining the scattering time. A densely packed ionized remote impurity with a small setback distance contributes significantly to scattering, resulting in a smaller τ_{MR} value. This implies that there is a point at which mobility increases with density. After a certain density value, the sheet will have more ionized impurities, resulting in a decrease in mobility. These impurities become more prevalent as the dopant layer is closer to the QW. Another source of MR scattering occurs due to different types of phonon scattering at higher temperatures. However, as we lower the temperature below 1 K, and hence we can ignore the contributions from phonons [29], the processes mentioned above will dominate the MR scattering events. The highest achievable mobility has been an ongoing question that many experimentalists and theorists have tried to answer. A recent study by Dr. Loren Pfeiffer's group at Princeton reported a record high electron mobility of 57×10^6 cm^2(Vs)$^{-1}$ and addressed different cases that limit attaining a 100 million mobility [36]. In our study, we used heterostructures

from Dr. Pfeiffer with electron mobility in the range of 20×10^6 cm^2(Vs)$^{-1}$ to 30×10^6 cm^2(Vs)$^{-1}$.

2.2 Shubnikov-de Haas Oscillations and Classical Hall Effect

2.2.1 Resistivity Tensor and Hall Effect

For a homogeneous system, in the absence of an external magnetic field, the relationship between current density ($\vec{j}$) and electric field ($\vec{E}$) is described by the following scalar equations

$$\vec{j} = \sigma \vec{E}, \tag{2.3}$$

and

$$\vec{E} = \rho \vec{j}, \tag{2.4}$$

where σ and ρ represent the conductivity and resistivity, respectively. When the electric field is parallel to the current, ρ and σ exhibit an inverse relationship, denoted by $\rho = \frac{1}{\sigma}$ [42, 43]. In the presence of a magnetic field, the situation becomes more complex as the electric field is no longer parallel to the current. In this case, the scalar conductivity (resistivity) must be replaced by a conductivity (resistivity) tensor,

$$\vec{j} = \widehat{\sigma}\ \vec{E}, \quad \text{or} \quad \begin{pmatrix} J_x \\ J_y \end{pmatrix} = \begin{pmatrix} \sigma_{xx} & \sigma_{xy} \\ \sigma_{yx} & \sigma_{yy} \end{pmatrix} \begin{pmatrix} E_x \\ E_y \end{pmatrix}. \tag{2.5}$$

In this tensor, the diagonal elements are even functions of the magnetic field B, while the off-diagonal elements are odd functions of B. When the electron system is isotropic and has $\sigma_{xx} = \sigma_{yy}$, one can represent the tensor equation in the following form

$$\vec{j} = \widehat{\sigma}\ \vec{E}, \quad \text{or} \quad \begin{pmatrix} j_x \\ j_y \end{pmatrix} = \begin{pmatrix} \sigma_{xx} & \sigma_{xy} \\ -\sigma_{xy} & \sigma_{xx} \end{pmatrix} \begin{pmatrix} E_x \\ E_y \end{pmatrix}. \tag{2.6}$$

The off-diagonal elements represent the conductivity arising from a transverse charge accumulation known as the Hall conductivity. The classical Hall effect was first discovered by Edwin Hall in 1879, and it describes a transport phenomenon that occurs when a magnetic field is applied perpendicular to current flow in a thin film, such as in the case of a 2DEG. When this is the case, the Lorentz force acts on the charge carrier q as

$$F = q(\vec{v_d} \times \vec{B}), \tag{2.7}$$

where v_d is the drift velocity of the charge carrier, and B is the magnetic field applied perpendicular to the charge carrier flow. The Lorentz force compels the charged particle to move in a transverse direction, resulting in a potential build-up on one side of the sample, as shown in Fig. 2.3.

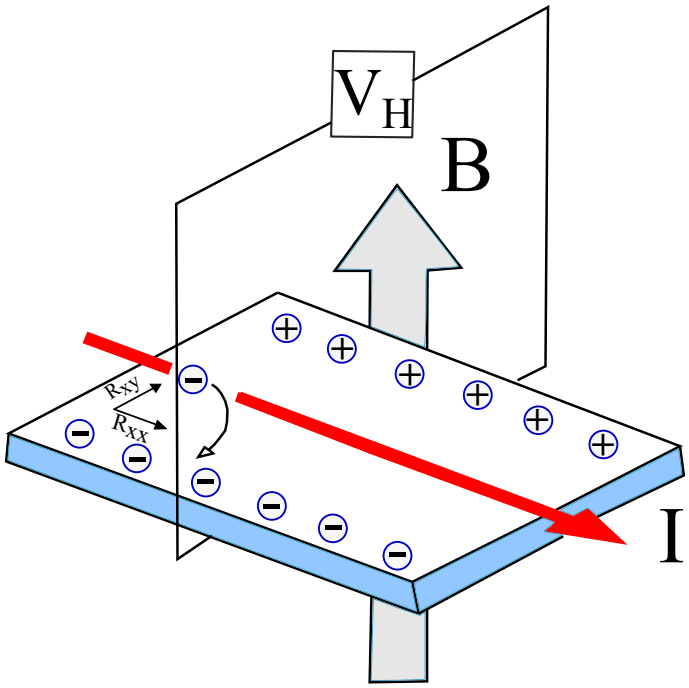

FIGURE 2.3 – A schematics of the Hall effect. Applying a magnetic field perpendicular to a sample causes charge to accumulate on one side of the sample due to the Lorentz force, resulting in a voltage difference along the transverse (Hall) direction. Figure reproduced from reference [44] with modifications.

The electric field force generated by this charge imbalance is given by $F_e = \frac{eV_H}{W}$, where V_H is the Hall voltage generated across a width w, balances out the Lorentz

force, *i.e.*,

$$\frac{eV_H}{w} = ev_dB. \tag{2.8}$$

The current I through the sample is given by

$$I = Nev_dA, \tag{2.9}$$

where N is the electron density per unit volume, and A is the cross-sectional area defined as $A = wd$ for a sample with thickness d. From Eq. 2.8 and Eq. 2.9, the Hall voltage can be written as

$$V_H = \frac{IB}{Ned} = \frac{IB}{ne}, \tag{2.10}$$

where $n = Nd$ is the 2D electron (or hole) density per unit area. Note that the transverse direction does not create any actual current flow. Instead, in the transverse direction, there will be a transverse conductivity that is given by dividing the Hall voltage V_H by the longitudinal current. Using the tensor in Eq. 2.5, one can write σ_{xy} as

$$\sigma_{xy} = \frac{E_y}{j_x} = \frac{V_H/W}{I_x/W} = \frac{V_H}{I_x}. \tag{2.11}$$

This equation implies that the Hall conductance (resistance) and conductivity (resistivity) are equal and have no geometric factors. It follows that the transverse Hall resistivity given by $R_H = \frac{V_H}{I} = \frac{B}{ne}$ and depends only on the size of the magnetic field and the electron density, *i.e.*, no other physical parameters such as sample geometry play a role. Finally, the relation between resistivity and conductivity is calculated from the tensor as,

$$\sigma_{xx} = \frac{\rho_{xx}}{\rho_{xx}^2 + \rho_{xy}^2}, \quad \rho_{xx} = \frac{\sigma_{xx}}{\sigma_{xx}^2 + \sigma_{xy}^2} \tag{2.12}$$

$$\sigma_{xy} = \frac{-\rho_{xy}}{\rho_{xx}^2 + \rho_{xy}^2}, \quad \rho_{xy} = \frac{-\sigma_{xy}}{\sigma_{xx}^2 + \sigma_{xy}^2}. \tag{2.13}$$

When the magnetic field is large, $\rho_{xy} \gg \rho_{xx}$, then the Eq. 2.13 can be written

approximated as

$$\sigma_{xx} \simeq \frac{\rho_{xx}}{\rho_{xy}^2}. \tag{2.14}$$

Below, we will investigate an extreme case of this phenomenon: an insulating state with zero resistance. One of the many fascinating results in Hall effect physics arises when the Lorentz force becomes sufficiently large that the electron's motion becomes circular.

2.2.2 Shubnikov-de Haas Oscillations

In a heterostructure, as explained earlier, the motion of electrons along the growth (z) direction is restricted by an approximately triangular potential well at the interface. Within this direction, the electrons occupy bound states referred to as sub-bands [45]. The intriguing physics in condensed matter systems often stems from the density of states (DOS), denoted as g. At low temperatures, in a 2DEG, the zero-field DOS, g_0, is constant and can be expressed as

$$g_0 = \frac{n}{E_F} = \frac{m^*}{\pi\hbar^2}, \tag{2.15}$$

where m^* is the effective mass of the carriers ($m^* = 0.067m_e$ in GaAs), n is the electron density, $\hbar$ is the reduced Planck's constant, and E_F is the Fermi energy. When a magnetic field is applied along the z direction, electrons experience a Lorentz force, causing them to move in circular orbits in the $x - y$ plane, with their energy states collapsing into quantized levels known as Landau levels (LLs), as depicted in Fig. 2.3b.

In the absence of disorder, the DOS would form a series of Dirac delta functions, spaced by the cyclotron energy $\hbar\omega_c$. This result stems from the complete solution of the 2D Schrödinger equation in a magnetic field, giving the DOS as

$$g(\epsilon) = g_0\hbar\omega_c \sum_{n=1}^{\infty} \delta(\epsilon - \epsilon_n), \tag{2.16}$$

where $\epsilon_n = \left(n + \frac{1}{2}\right)\hbar\omega_c$. The number of available states in each Landau level, *i.e.*, the landau level degeneracy n_B, is given by $n_B = \frac{eB}{h}$, where h is the Planck's constant and e is charge of the electron. As the magnetic field increases, the Landau level degeneracy (n_B) increases, requiring more electrons to fill each level [46].

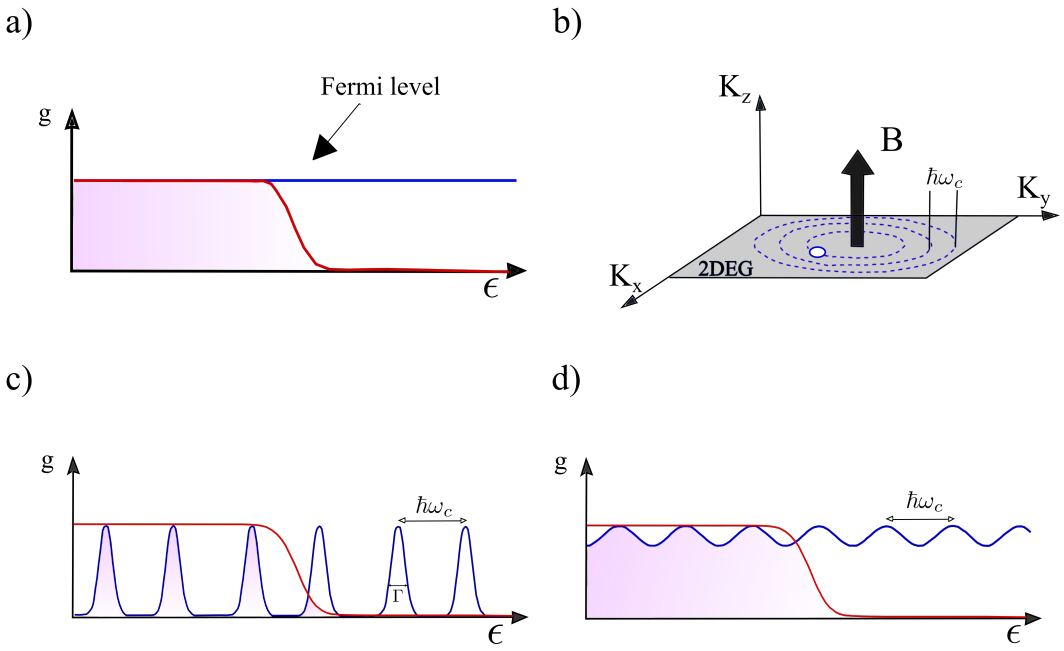

FIGURE 2.4 – The schematic shows the density of states (DOS) represented by the red line and the electron energy state. a) The DOS at B = 0. b) When a non-zero magnetic field is present, the electron energy states collapse onto concentric circular orbits in k-space, separated by a well-defined gap. c) DOS with well-separated Landau levels ($\Gamma \ll \hbar\omega_c$). d) Broadened Landau levels that overlap, resulting in a sinusoidal modulation of the DOS. The figures are adapted and modified from references [44, 45] with permission.

In reality, imperfections and impurities cause scattering leading to a broadening of these LLs. The broadening is given by $\Gamma = \frac{h}{\tau}$, where τ is the quantum lifetime. Under sufficiently low magnetic field conditions, when $\hbar\omega_c \ll \Gamma$, the LL disorder broadening becomes significant as the levels overlap and lead to sinusoidal oscillations of the DOS as given by a specific form,

$$g(\epsilon) = g_0 + \Delta g \sin\left(\frac{2\pi\epsilon}{\hbar\omega_c}\right), \tag{2.17}$$

where Δg represents the amplitude of the oscillations. Electronic properties oscillate due to variations in the DOS near the Fermi level. These oscillations, caused by changes in the magnetic field or Fermi level, are known as the de Haas-van Alphen effect (dHvA) in general and the Shubnikov-de Haas (SdH) effect for conductivity. In the coming chapters, I will discuss the electron density calculations for devices presented in this thesis using SdH oscillations.

2.3 Brief Review of Integer and Fractional Quantum Hall Effect

At higher magnetic fields, $\hbar\omega_c \gg \Gamma$, the LLs are well separated. In 1980, Klaus von Klitzing made a groundbreaking discovery of a quantum analogue of the Hall effect [47]. He studied transport in a clean MOSFET and observed that the Hall resistance changes in precise steps as the magnetic field varies. The Quantum Hall Effect (QHE) occurs when an integer number of LLs are exactly filled, corresponding to magnetic field values given by

$$B_\nu = \frac{nh}{e\nu}, \tag{2.18}$$

where in this equation, $\nu = \frac{n}{n_B}$ is the filling fraction (the ratio of the number of electrons and the available states per LL). When an integer number of LLs is filled, the Fermi energy lies between LLs where no states are available for charge carriers. As a result, the longitudinal conductivity (resistivity) drops to zero, $\sigma_{xx} = 0,\ \rho_{xx} = 0$.

At integer filling of the LLs, the transverse resistance is quantized, and as a result, plateaus are formed. These steps correspond to whole-number multiples of a constant known as the von Klitzing constant ($R_K = \frac{h}{e^2}$). In 1990, the National Institute of Standards and Technology (NIST) adopted the quantum of resistance R_K as the primary definition since it can be related to the fundamental units h and

e. In low-disorder samples, additional quantum Hall plateaus appear at fractional filling factors, accompanied by fractionally quantized Hall resistivity [48]. To explain this, the composite fermion (CF) model is used [49, 50], where each electron pairs with two flux quanta, forming CFs that experience a reduced effective magnetic field. The effective filling factor for CFs is given by $\nu^* = \frac{\nu}{1-2\nu}$, leading to fractional quantum Hall (FQH) series (1/3, 2/5, 3/7...) and is shown in Fig. 2.5. It is important to note that this description only gives an odd denominator value, representing the integer quantum Hall effect of CFs occurring only at the odd denominator of ν.

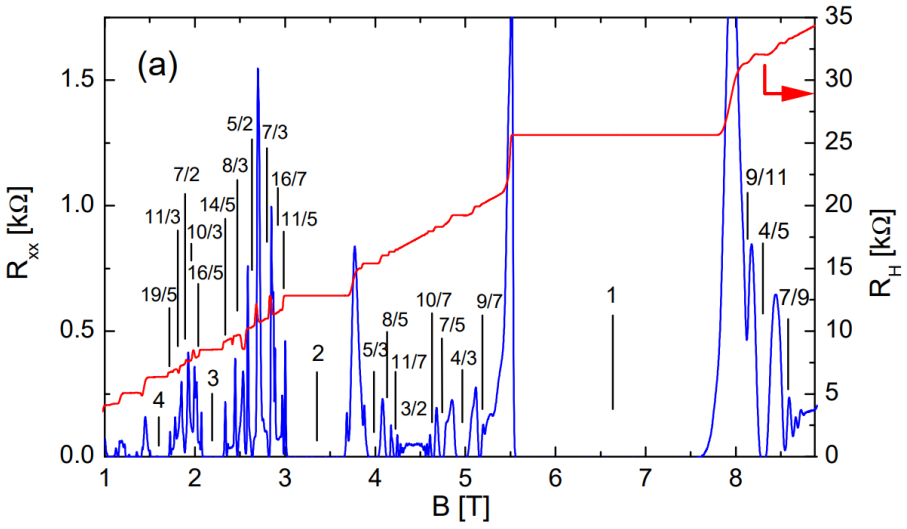

FIGURE 2.5 – Longitudinal and transverse magnetotransport conducted at Gervais lab on a van der Pauw device with an electron density 1.60×10^{11} cm^{-2} and mobility 16.6×10^6 cm^2(Vs)$^{-1}$. When the longitudinal resistance reaches a minimum, a corresponding plateau is observed in the Hall resistance, indicating both integer and fractional Hall states. The figure is used with permission from reference [44].

In 1987, an unexpected even-denominator FQH plateau was discovered at a filling factor of 5/2, prompting the development of several theoretical models. The Moore-Read (MR) Pfaffian wavefunction is the most prominent [51]. High magnetic field characterization of the devices used in this thesis will be provided in Chapter 3 to assess the high quality of the device and its ability to host such exotic quantum Hall states.

2.4 Measurement Geometries

2.4.1 Hall Bar and van der Pauw Geometry

Hall bar and van der Paw (VdP) geometries, the most commonly used device structures in quantum transport measurements, share an identical topology of a single outer edge as shown in Fig. 2.6a and b. The results of electronic transport

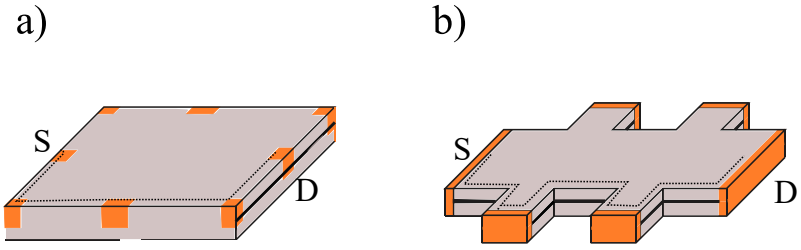

FIGURE 2.6 – Schematics of measurement geometries. Panels a) and b) depict a van der Pauw (VdP) and Hall bar geometry with marked source (S) and drain (D), respectively. The dotted line shows the edge current path.

measurements for both are predominantly influenced by edge state conduction. Although the quantum Hall effect is not the focus of our study, the previous section provides essential background for understanding this phenomenon. In VdP and Hall bar geometries, the dominance of edge states limits the ability to probe bulk behaviour and necessitates a different geometry. Consider filled LLs, as shown in Fig. 2.7,

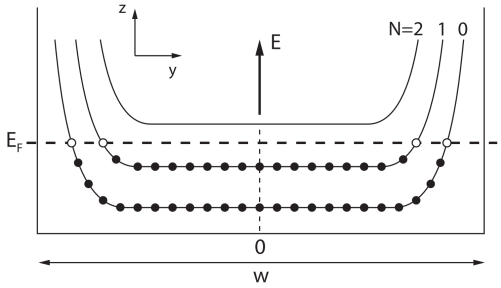

FIGURE 2.7 – Band bending at the edges of the sample in the IQHE. The LLs bend upwards at the edges of the sample, passing through the Fermi level, resulting in an edge current. Figure reproduced with permission from references [44, 45].

depicted as a function of the sample width w. At the edge, a confinement potential

will bend the energy bands upwards. Due to this bending, the E_F will cross the LLs, giving rise to a conduction channel known as the edge state that is used to study quantum Hall states [52]. Conversely, the bulk of the sample behaves like an insulator.

2.4.2 Corbino Geometry

The Corbino disk contact arrangement creates a distinct topology compared to Hall and VdP geometries. In a single-ring Corbino (Fig. 2.8a), two contacts are formed concentrically, thus preventing current from being carried by edge states. The Corbino effect was discovered by Orso Mario Corbino [55]. Unlike the Hall and VdP geometries where the resistance can vanish due to dissipationless edge modes, the conductance between contacts vanishes in the Corbino disk. This vanishing conductance is caused by directing the current through the bulk insulating region, thereby making the Corbino disk an ideal platform for studying the bulk properties of 2DEG.

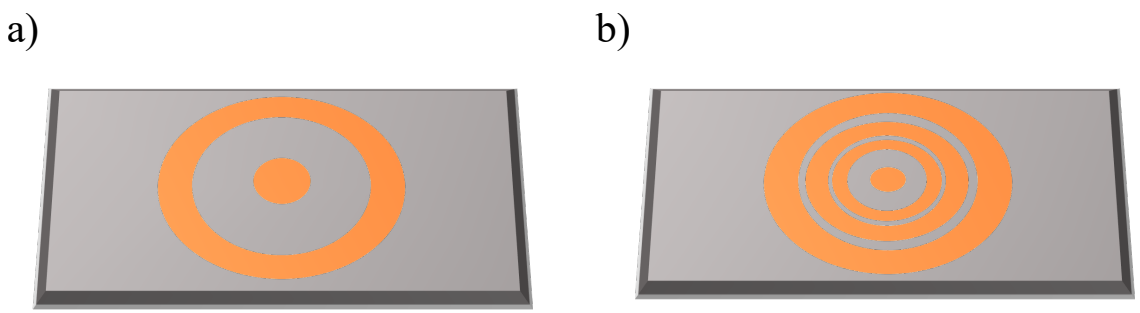

FIGURE 2.8 – Schematics of single (panel a) and multi-ring (panel b) Corbino. The orange colour depicts the contacts. The figures are reproduced with permission from references [53, 54].

The total resistance between outer and inner contact is given by

$$R = \frac{\log(r_2/r_1)}{2\pi\sigma_{xx}}, \tag{2.19}$$

where r_1 and r_2 are the inner and outer radii of the 2DEG ring. As we see in

this equation, the resistance in a Corbino device is proportional to $\frac{1}{\sigma_{xx}}$, rather than ρ_{xx}. Conventionally, conductance is measured in the Corbino geometry since the resistance diverges as $\sigma_{xx} \to 0$ in a quantum Hall minima. The equation for σ_{xx} is given by

$$2\pi\sigma_{xx} = G\ log(r_2/r_1), \tag{2.20}$$

where G is the conductance. This equation relates the microscopic transport property (σ_{xx}) to the macroscopically measurable quantity (G). The comparison of magnetotransport measurements in Hall bar and Corbino devices, as presented in [45], demonstrates that σ_{xx} in a Corbino device and ρ_{xx} in a Hall bar exhibit similar behaviour. However, a key distinction is the sharp decrease in conductivity observed in the Corbino device as the magnetic field is applied. This rapid decrease at a rate of $\frac{1}{B^2}$ is due to the changes in the carrier lifetime and DOS and also due to the lengthening of the current path in a Corbino geometry [1].

We selected Corbino geometries for our study of hydrodynamic transport due to their ability to probe the bulk. To investigate hydrodynamic transport at zero magnetic field in 2DEG, we first measured the resistance and its variation with increasing temperature in two previously fabricated single-ring Corbino devices (refer to Appendix A for details of the fabrication). While the zero-field transport characteristics show hints of hydrodynamic transport, with details on hydrodynamic transport provided in the next section, they unavoidably included effects from the contacts due to the two-point measurement configuration. To mitigate this, we fabricated a four-contact device (referred to as a multi-ring Corbino) as depicted in Fig. 2.8b so that a four-terminal measurement could be performed. In order to understand the results presented in this thesis, the following section will provide a brief introduction to the various electron transport regimes.

1. Lengthening of the current path in a Corbino disk under a magnetic field refers to the increased effective path that current travels due to the device's circular geometry. In the presence of a perpendicular magnetic field, the current carriers experience the Lorentz force, leading to curved trajectories and extending the radial current path between the inner and outer contacts, influencing the system's magnetoresistance.

2.5 Single Particle Electron Transport

2.5.1 Diffusive Transport

In most metals, the transport of electrons is limited to diffusive transport, *i.e.,* electrons scatter from the neighbouring impurities or phonons (Fig. 2.9a), resulting in the relaxation of momentum to the lattice. The Drude model describes a diffusive regime where electrons can be treated similarly to gas molecules in a classical picture [42]. In this model, the Drude resistivity (or conductivity) can be expressed in terms of the momentum-relaxing (MR) scattering time τ_{MR} or mobility μ. In the Drude model, the resistivity is given by

$$\rho = \frac{m}{ne^2\tau_{MR}} = \frac{1}{ne\mu}, \tag{2.21}$$

where n is the electron density, m is the electron mass and e is the electron charge. As previously mentioned, τ_{MR} has two contributing factors: one is the relaxation time associated with the impurity/ disorder scattering, and the other is associated with phonon scattering. At temperatures below 1 K, the effects of phonon scattering are reduced and hence negligible [29].

2.5.2 Ballistic Transport

For an ultra-clean electron system (high electron mobility), the impurity scattering will be minimized at low temperatures, resulting in a long momentum-relaxing mean free path (ℓ_{MR}). This will result in a ballistic transport where the electrons will move through a channel of width W without any scattering or very little scattering (quasi-ballistic) from the boundaries of the device (Fig. 2.9b). When this is the case, scattering conserves momentum, and the resistance is expected to decrease to zero. However, experiments conducted in a 1D ballistic conductor 30 years ago [56, 57]

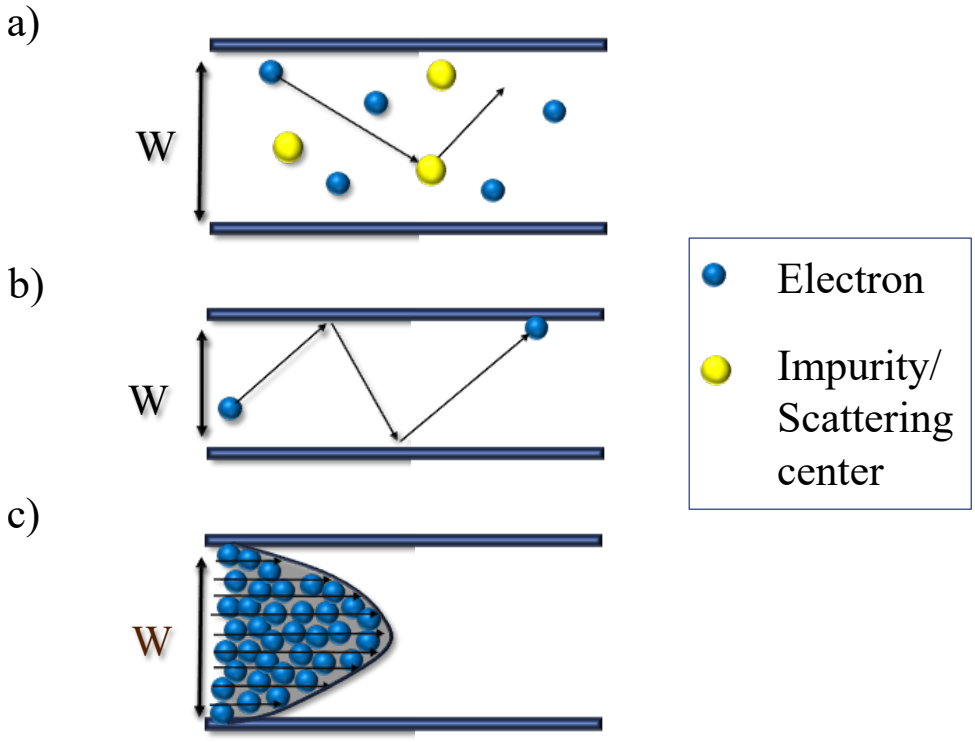

FIGURE 2.9 – Schematics illustrating different electronic transport regimes in a channel of width W. a) At higher temperatures, electrons scatter with impurities/-defects in the system or with phonons, resulting in diffusive transport, which can be described by the Drude model. b) The panel illustrates the quasi-ballistic transport regime, which occurs at very low temperatures in ultra-clean materials. In this regime, electrons travel with minimal scattering, with some scattering at the channel boundary that conserves momentum. In an ideal scenario, electrons can move without any scattering, which is referred to as ballistic transport. c) Hydrodynamic flow is achieved when electron-electron interaction is the dominant scattering mechanism in the channel, resulting in collective electron motion resembling the flow of a viscous fluid.

showed that this was not the case, and resistance was found to be given by

$$R_B = \frac{h}{2e^2 M}, \tag{2.22}$$

where h is the Planck's constant, and M is the number of conducting modes. For a box of size W, it is given in terms of Fermi wavelength (λ_F) by $R_B = \frac{h}{2e^2}\frac{\lambda_F}{2W}$. The resistance R_B was shown to arise from the contacts, which act as a large reservoir with an infinite number of electrons. One can, therefore, view this as a contact resistance as one tries to push electrons to the in-between narrow ballistic channel.

In 2001, Picciotto *et al.* [58] at Bell Labs conducted a four-point measurement to probe the intrinsic ballistic transport. The study was conducted on a one-dimensional ballistic wire patterned on a high-mobility GaAs/AlGaAs heterostructure. They measured a vanishing ballistic resistance using this four-point configuration and a metallic field-effect gate. In contrast to single-particle electron transport, the following section will highlight the implications of continuum transport behaviour, which forms the core focus of this thesis.

2.6 Hydrodynamic Transport

2.6.1 Landau's Description of Fermi Liquid Theory

L. D. Landau developed Fermi liquid theory [59] to describe interacting Fermi systems, such as liquid ^{3}He and electrons in metals at low temperatures. In Fermi liquid theory, the Pauli exclusion principle limits how particles (or electrons in metals) scatter off each other. At $T = 0$ K in metals, all the electrons occupy the surface of the filled Fermi sphere with energy E_F. Now, consider a single excited electron with energy $E_1 \gg E_F$. For this electron to scatter, it must interact with another electron of energy E_2. According to the exclusion principle, these electrons can only scatter into unoccupied states. Since at $T = 0$ K all the states below E_F are occupied, no states are available for scattering, meaning that an electron on the Fermi surface at absolute zero has an infinite lifetime.

As the temperature increases, the Fermi surface smears over a distance k_BT, where k_B is the Boltzmann constant, creating available states for scattering. As a result, electrons in this partially occupied shell of width k_BT can now scatter into available states, leading to a scattering rate proportional to $(k_BT)^2$ [42]. The probability of finding an empty state for two electrons within this k_BT region near

E_F is $\left(\frac{k_B T}{E_F}\right)^2$, leading to a scattering rate given by

$$\frac{1}{\tau_{MC}} \approx \left(\frac{k_B T}{E_F}\right)^2. \tag{2.23}$$

The momentum-conserving mean free path (ℓ_{MC}) is given by $\ell_{MC} = v_F \tau_{MC}$, where v_F is the Fermi velocity. The kinematic viscosity ν, which can be understood in analogy to classical gases, where it is proportional to $\sim v\ell$, with v representing the average velocity of gas molecules and ℓ being the mean free path. For electrons and other fermions, using low-order terms of the Boltzmann transport equation, Polini and Geim [9, 60] derived the relation $\nu = \frac{1}{4} v_F \ell_{MC}$. The temperature dependence of ℓ_{MC}, which scales as $\frac{1}{T^2}$, leads to a similar dependence for ν [61]. This suggests that as momentum-conserving (MC) scattering decreases, ν increases and this may seem counterintuitive [14]. This has been shown experimentally to be significant in liquid ^{3}He at very low temperatures. For example, in refrigerators cooling ^{3}He to milliKelvin temperatures, the system enters the Fermi liquid regime, where the viscosity of ^{3}He increases sharply as $\frac{1}{T^2}$. Eventually, the viscosity becomes so high that further cooling becomes inefficient and difficult [62,63]. The Fermi liquid theory is applicable in both two-dimensional (2D) and three-dimensional (3D) interacting systems. In 2D systems, the interactions are stronger than in 3D systems, but this does not imply a failure of the Fermi liquid theory [64].

2.6.2 Electron Hydrodynamics and Viscosity

In the study of electronic transport in 2DEG, the role of $e - e$ scattering can be significant, particularly when it becomes the dominant scattering mechanism. Unlike other scattering mechanisms, $e - e$ scattering does not dissipate the total electron momentum but rather forms a continuum, leading to a transport regime known as hydrodynamic transport regime (Fig. 2.9c). Traditionally, hydrodynamics was used to describe classical fluids. It provides a universal framework that describes the behaviour of fluids at time and lengthscales larger than those associated with

local equilibration. The hydrodynamic framework can be applied to diverse systems, including strongly interacting fluids and ideal gases. In the case of electrons in metals, when $e-e$ scattering dominates, it establishes a local equilibrium, and when this is the case, the individual characteristics of electrons are lost, giving rise to a collective behaviour akin to the physics of a classical fluid. To describe this mathematically, we employ the Navier-Stokes (NS) equations of fluid mechanics. The NS equation is typically used for classical fluids experiencing frequent inter-particle collisions [65]. In this context, the NS equations for an electron fluid include an effective kinematic viscosity, denoted as ν, arising from momentum transfer between different fluid parts, as explained in the above section. As we shall see later, this viscosity leads to drag effects within the electron fluid that are similar to those seen in classical fluids.

When examining the hydrodynamic regime in electronic systems, we consider the continuity equation and the NS equation given by

$$\nabla \cdot \vec{u} = 0, \tag{2.24}$$

$$\frac{\partial \vec{u}}{\partial t} + \left(\vec{u} \cdot \vec{\nabla}\right) \vec{u} = \nu \vec{\nabla}^2 \vec{u} + \vec{f}, \tag{2.25}$$

where $\vec{u}$ is the electron drift velocity, $\nu = \frac{v_F \ell_{MC}}{4}$ is the electron viscosity [3] with v_F the Fermi velocity, and $\vec{f}$ is the body force per unit mass. The pressure gradient term, typically present in the NS equation, is absent in this context due to its relatively negligible contribution compared to the dominant electric field, see [66, 67]. The two primary body forces to consider are the force due to the external electric field $\vec{E}$ and the force arising from internal scattering mechanisms. Thus, the total body force per unit mass can be expressed by

$$\vec{f} = \vec{f}_{\text{EM}} + \vec{f}_{\text{scat}} = \frac{e}{m^*} \nabla \phi + \frac{\vec{u}}{\tau}, \tag{2.26}$$

where e is the electron charge, m^* is the effective mass ($0.067 m_e$ for GaAs/Al-

GaAs), τ is the effective mean-free scattering time, given by $\tau^{-1} = \tau_{\mathrm{MC}}^{-1} - \tau_{\mathrm{MR}}^{-1}$, and ϕ represents the electric potential generated by the electron flow due to an applied current. The continuity equation (Eq. 2.24) plays a crucial role in maintaining the incompressibility of the electron fluid, reflecting the strong Coulombic repulsion between electrons. The NS equation (Eq. 2.25) includes terms representing the viscous forces, momentum-relaxation due to disorder or phonon scattering, forces due to momentum-conserving scattering, and the external electric field.

In these equations, the current density $\vec{J}$ can be linked to the velocity $\vec{u}$ of the electron fluid and the external electric field $\vec{E}$ driving the current. Depending on which term dominates in the NS equation, the system can either revert to a diffusive transport regime or remain in the hydrodynamic regime [60]. In the viscous flow regime, where $\vec{\nabla} \times \vec{J} \neq \vec{0}$, the current distribution can exhibit complex patterns and vorticity [61, 68], necessitating knowledge of the electric field throughout the entire sample to determine the current accurately. In our work, such current vortices play no role since the current is purely radial. The viscous effect will arise solely from the body force, as we will discuss in Chapter 4.

2.7 Gurzhi Effect

In 1963, R.N. Gurzhi proposed that when an ultra-clean Fermi liquid is confined to a channel of width W, its resistance will vary non-monotonically and reach a minimum at a certain temperature [16]. At low temperatures if $\ell_{MC}, \ell_{MR} \gg W$, he predicted that the system would first be in a ballistic regime, with the resistance coming from electrons colliding at the channel boundary, hence independent of temperature. As the temperature increases, the MC scattering eventually dominates over other scattering processes when $\ell_{MC} \ll W \ll \ell_{MR}$ and will begin entering a hydrodynamic regime. We saw in the above section that the ν decreases with T, resulting in a decreasing resistance. As the temperature is further increased, the MR scattering dominates the system ($\ell_{MC}, W \gg \ell_{MR}$), resulting in regaining the

usual monotonic increase of resistance (see the retrace of Gurzhi's prediction in Fig. 2.10). Even though this effect was predicted in 1960, the experimental realization occurred much later, and more details about the current progress are provided in the next section.

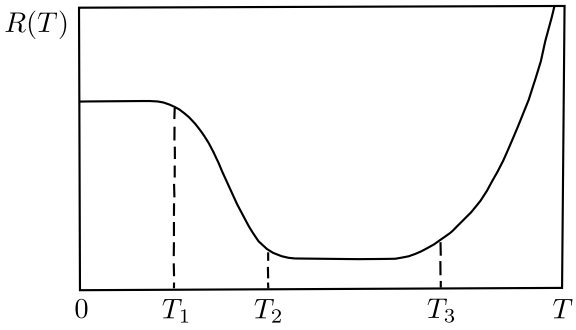

FIGURE 2.10 – Gurzhi effect. The figure shows different transport regimes as originally presented by R. N. Gurzhi [16]. The zero to T_1 temperature region represents ballistic transport, and the T_1 to T_2 region corresponds to hydrodynamic transport. The decrease in resistance observed is known as the Gurzhi effect. The system shows a diffusive transport at a higher temperature above T_3. This is a retrace of the original work of Gurzhi [16].

2.8 An Overview of Hydrodynamic Transport in Various 2DEG Systems and Hall Viscosity

Following Gurzhi's prediction of hydrodynamic transport, early efforts to observe these effects in clean potassium (K) samples were inconclusive due to the ℓ_{MC} being approximately 100 times larger than the device scale [69]. Later, in the 1990s, significant experimental evidence for hydrodynamic transport emerged with studies conducted on GaAs 2DEG wires [4]. In this study they applied current to enhance $e-e$ interactions, revealing a non-monotonic differential resistance as a function of electron current attributed to the Gurzhi effect. However, Gurzhi later suggested that this non-monotonic behaviour might also arise from a hydrodynamic-like effect due to the ballistic regime's MC scattering [70]. Observing hydrodynamic electron flow in solids has remained challenging due to the requirement for exceptionally clean materials. The advent of modern semiconductor technology has significantly advan-

ced this field through the creation of ultra-high mobility heterostructures [25–36]. Despite these advancements, the field experienced a period of stagnation until a resurgence of interest in 2016, driven by groundbreaking experimental observations in two-dimensional systems, notably graphene [61, 68, 71] and PdCoO2 [72].

In Section 2.6.2, we looked at the impact of viscous flow, highlighting the occurrence of vorticity. In a vicinity geometry, this can result in a negative electrical response [68]. This response stems when momentum diffuses transversely, generating shear flows that create vorticity and backflow. The backflow, in turn, produces a reverse electric field, leading to a negative nonlocal resistance, which remarkably persists despite significant ohmic currents [61]. It is important to note that negative nonlocal resistance due to current backflow can also occur in the ballistic regime [10, 73–75]. Therefore, interpreting low-temperature results requires caution. Imaging advancements allowed us to directly visualize electron flow, providing further support for hydrodynamic electron transport [76–78].

Theoretical [61,68,79–85] and experimental studies [5,6,11,72,73,77,86–97] have explored the viscous flow of electrons. Many theorists favour Corbino geometry due to its simplified geometry and symmetry. The Corbino geometry is advantageous due to its lack of lateral edges, simplifying boundary conditions to those at the contacts. In this setup, the current density is given by

$$J(r) = \frac{I}{2\pi r}\hat{r}, \tag{2.27}$$

where I is the total current. In the limit of infinite conductivity ($\sigma \to \infty$), the electric field $E(\vec{r})$ calculated from this current density is zero. This suggests that current flows without an electric field, raising the question of whether a Corbino can be considered a perceptual motion machine [98]. The authors of reference [98] further studied this concept of freely flowing current in a Corbino with an idealized disorder-free contact. In this case, the bulk dissipation due to viscosity has to be compensated by the work done by the current source, resulting in a sharp elec-

tric potential in-homogeneity close to the bulk-contact interface [99]. Studies have progressed towards analyzing hydrodynamic effects in the Corbino geometry. Experimental [94] and theoretical [100] studies have investigated whether $e-e$ interactions in a Corbino geometry can overcome the Landauer-Sharvin resistance, which arises even in a perfect lattice due to the finite number of propagating electron modes. The results indicate that Landauer-Sharvin resistance can be spread to the bulk in this particular geometry, and hydrodynamic transport can eliminate its effects. Hydrodynamic transport in the Corbino geometry has recently garnered more attention due to its potential in measuring electron viscosity [66] and due to the possibility of directly probing Hall viscosity, an intrinsic property of the system [83]. These studies suggest that the Corbino geometry is ideal for studying such complex phenomena. In chapters 3 and 4, I will present transport measurements conducted in a Corbino geometry, demonstrating signatures of ballistic and hydrodynamic transport.

3

Anomalous Electronic Transport in High-Mobility Corbino Rings

3.1 Preface

This chapter presents local transport measurements on two multi-terminal Corbino devices fabricated on ultra-high mobility 2DEGs. Detailed fabrication procedures are provided in Appendix A. The quality of the devices was assessed through magnetotransport measurements. Previous studies in the Gervais Lab have investigated reentrant quantum Hall states and charge density waves in the second and third Landau levels of sample CBM301 [101]. Magnetotransport measurements for sample CBM302, presented in Fig. 3.1, reveal well-defined quantum Hall states, indicating higher quality of the sample.

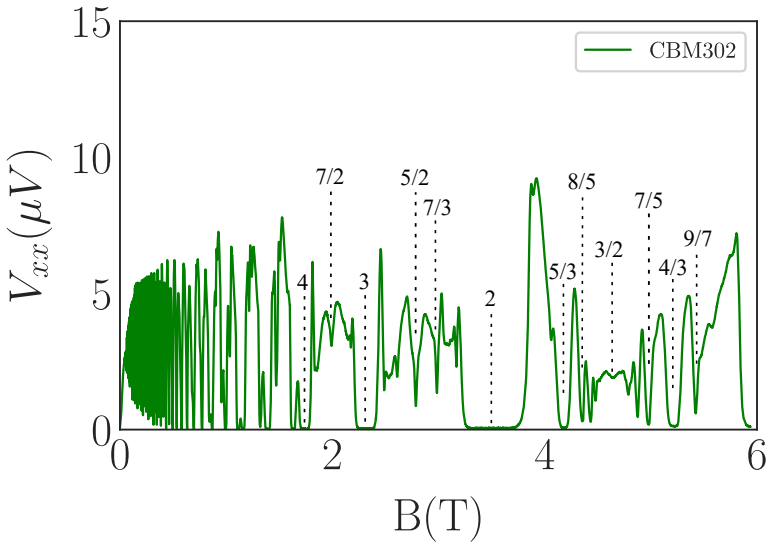

FIGURE 3.1 – Figure shows four-point magnetotransport measurement result of CBM302 conducted at 12 mK. The data show well-defined integer and fractional QHS, indicating the high quality of the sample.

Enhanced $e-e$ interactions are crucial for achieving hydrodynamic transport. Some studies achieve this by heating the sample using a current passed through the device. The 2DEG formed using delta-doping methods offers increased stability and robustness for such measurements. In this study, instead of applying a current to heat the sample, we increased the temperature of the stage to which the sample was thermalized in the dilution refrigerator. The results discussed in this chapter are relevant to various aspects of condensed matter physics. It should be noted that the full manuscript below is identical to the version published in *Nature communications* under the title *"Anomalous Electronic Transport in High-Mobility Corbino Rings"* [17]. The figures and notations align with the published manuscript and remain independent from the rest of this thesis. Supplementary materials (SM) are provided in Appendix B. Throughout this chapter, we will refer to the momentum-conserving mean free path as ℓ_{ee} instead of ℓ_{MC} and the momentum relaxing mean free path as ℓ_e instead of ℓ_{MR}.

3.2 Abstract

We report low-temperature electronic transport measurements performed in two multi-terminal Corbino samples formed in GaAs/Al-GaAs two-dimensional electron gases (2DEG) with both ultra-high electron mobility ($\gtrsim 20 \times 10^6\ cm^2/Vs$) and with distinct electron density of 1.7 and $3.6 \times 10^{11}\ cm^{-2}$. In both Corbino samples, a non-monotonic behavior is observed in the temperature dependence of the resistance below 1 K. Surprisingly, a sharp decrease in resistance is observed with increasing temperature in the sample with lower electron density, whereas an opposite behavior is observed in the sample with higher density. To investigate further, transport measurements were performed in large van der Pauw samples having identical heterostructures, and as expected they exhibit resistivity that is monotonic with temperature. Finally, we discuss the results in terms of various lengthscales leading to ballistic and hydrodynamic electronic transport, as well as a possible Gurzhi effect.

3.3 Introduction

Over the last two decades, great progress has been achieved in increasing the electron mobility in two-dimensional electron gases formed in MBE-grown materials such as GaA/AlGaAs and alternatively in exfoliated graphene. Spectacularly, the electron mobility in GaAs/AlGaAs 2DEGs has recently been reported to reach $57 \times 10^6\ cm^2(Vs)^{-1}$ [1] and, in the absence of phonons at low temperatures, this results in large impurity-dominated mean free path that can exceed 350 μm. These high-mobility 2DEGs are notoriously well described by Fermi liquid theory at low temperatures, but what is perhaps less obvious is that counter-intuitive phenomena can arise as a result of an interplay between hydrodynamic transport and confinement. As an example, Gurzhi noted in 1963 [2,3] that if a Fermi liquid is confined in a narrow constriction of characteristic size d, within some restrictive conditions the resistance of the metal could decrease with increasing temperature. More recently,

studying the scattering lengths in 2D semiconductors with moderately high electron mobility, Ahn and Das Sarma [4] proposed that Gurzhi's prediction could occur even in bulk GaAs 2DEGs with sufficiently short electron-electron scattering lengths and low disorder.

Motivated by these works, we have fabricated two identical multi-terminal Corbino rings in GaAs/AlGaAs 2DEGs with electron mobility exceeding 20×10^6 $cm^2(Vs)^{-1}$, and with two different electron density leading to distinctive electron-electron and electron-impurity scattering lengths. Four-point conductance (resistance) measurements were performed in these Corbino with a transport channel defined by a 40 μm annular ring probing only the bulk of the sample, *i.e.* with no edge. These measurements are compared with similar measurements performed in millimetre scale van der Pauw (VdP) samples that have the same heterostructure. We note the intrinsic resistivity (conductivity) in the VdP and Corbino samples differs from the measured resistance (conductance) solely by a geometric factor and therefore both will be used interchangeably in the text below. Astonishingly, the temperature dependence of both multi-terminal Corbino shows an anomalous temperature dependence whereby in one case a sharp decrease in resistance is observed at temperatures below 1 K with increasing temperature, and an opposite behavior is observed in the other Corbino sample. In the van der Pauw (VdP) samples with identical heterostructure to the multi-terminal Corbino, as expected a monotonic behavior of resistivity with temperature was observed.

3.4 Results

3.4.1 Corbino and van der Pauw Geometry

Typical measurements performed in large 2DEG samples usually utilizes either samples prepared in van der Pauw or Hall bar geometry. In the VdP geometry, the electrical contacts are located in each corner and midpoint along the perimeter of a

square wafer typically of size 3×3 mm. Four-point measurements are then performed by applying a fixed current (voltage) and measuring voltage (current) using a combination of four contacts. Even though non-patterning helps to preserve the pristine state of the ultra-high quality 2DEG, transport measurements performed in either VdP or Hall bar unavoidably contain both the bulk and surface (or more precisely the edge) effects. In the case where only the bulk contribution to the resistivity (or conductivity) is wanted, one can have recourse to the Corbino geometry where the sample contacts are prepared in a circular/ring geometry, with the active region of the 2DEG sample defined by an annulus. In this case, the current is applied concentrically from the outer to inner radii and the electronic transport measurements solely probe the bulk of the sample. Most studies performed so far in the Corbino geometry have focused on samples with an inner contact and a single outer ring, and these are inherently two-point contact measurements where, unfortunately, the contact resistance with the 2DEG is not eliminated. However, multi-terminal Corbino samples possessing one inner contact and three outer rings can be fabricated for four-point measurements, see Fig.1a. While the Corbino geometry does not have any edge nor radial dimension, however it does have a channel length which is defined as the distance between the inner diameter of the third ring (V_+ probe) and the outer diameter of the second ring (V_- probe). In our case, this channel length is $L_{Corbino} = 40\ \mu m$ for both Corbino samples.

3.4.2 Electron Density and r_s Parameter

The dimensionless electron-electron interaction parameter $r_s = (\pi n a_B^2)^{-\frac{1}{2}}$, where n is the electron density of either set of samples, and $a_B = 103\ \mathring{A}$ is the calculated effective Bohr magneton radius, are 0.92 and 1.32 for the 301 and 302 wafers, respectively, and they are shown in Fig.1b. Given its significantly higher r_s value and ultra-high electron mobility, the 2DEG formed in 302 samples (when compared to 301) are expected to inherently have enhanced electron-electron interaction, and conversely significantly distinct electron-electron scattering lengths versus tempera-

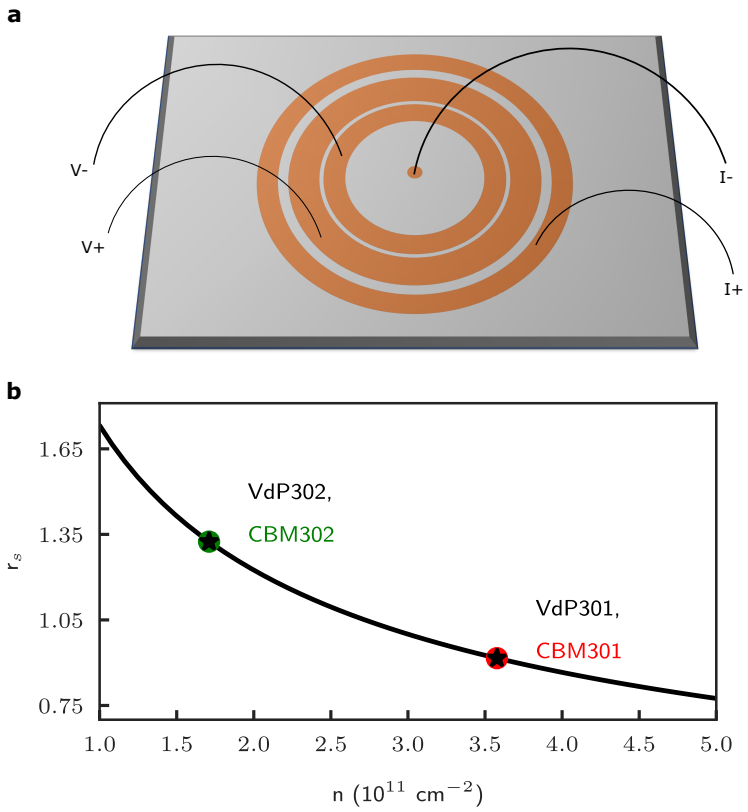

Figure 1 – Schematics of the multi-terminal Corbino and electron-electron interaction parameter. **a** Four-terminal Corbino design with the gold rings depicting the contact geometry for sample CBM301 and CBM302. The contact ring sizes is identical for both samples. **b** Electron-electron interaction parameter r_s *versus* electron density (see main text). The r_s parameter values for CBM301 (and VdP301) denoted as red dot (star) and CBM302 (and VdP302) denoted as green dot (star) are 0.92 and 1.32, respectively.

ture.

3.4.3 Four-point Corbino Conductance Measurements

Electronic transport measurements were carried on with the multi-terminal Corbino samples. In this geometry, it is usual to measure the conductance and for this reason we first show the measured conductance *versus* temperatures in both samples. We performed these measurements with two distinct measurement circuits, labeled

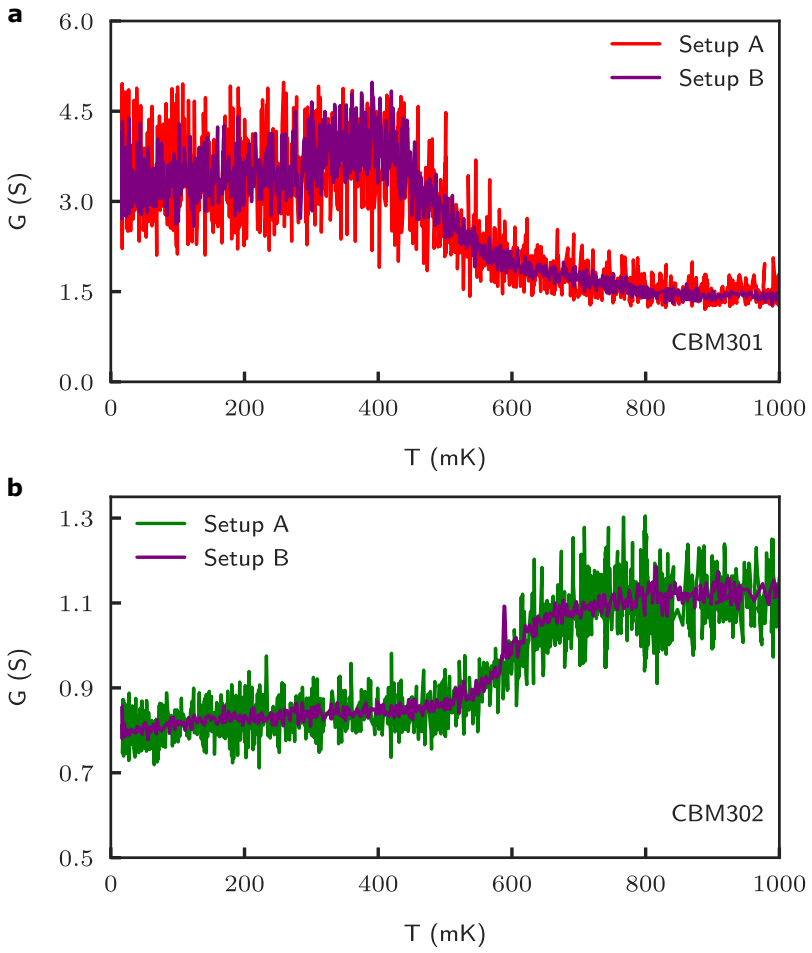

Figure 2 – Temperature dependence of the Corbino conductance. The four-point conductance G measured with two distinct measurement setups labeled A and B (see main text and SM), is shown *versus* temperature for CBM301 (**a**) and CBM302 (**b**). An increase in conductance (decrease in resistance) onsetting near 500 mK is observed in CBM302 (panel **b**) with increasing temperature, whereas an opposite behavior at ∼400 mK is observed for CBM301 (panel **a**). Note that in the next figures the resistance $R = G^{-1}$ rather than the conductance will be shown.

setup A (20 nA excitation current) and setup B (83 nA excitation current), see SM. These results are shown in Fig.2a for CBM301 and Fig.2b for CBM302, with both circuits in excellent agreement with one another. The temperature dependence of conductance measured in CBM301 shows a decrease in conductance at temperatures above ∼400 mK, which at first sight may not be surprising given there has been reports of increasing electron mobility well below 1 K in 2DEGs of moderately high mobility [5]. Surprisingly, a completely opposite trend is observed for CBM302

where an anomalous increase in conductance (decrease in resistance) with increasing temperature is observed at temperatures above $\sim$500 mK. The resulting fractional change in conductance ($\Delta G/G$) is $\sim$ 40% between $\sim$500 and 700 mK, and this is different from the anomalous transport behavior observed in CBM301 in spite of both samples having an identical geometry and similar high electron mobility.

3.4.4 Probe Symmetry and Reciprocity Theorem

To further validate our observation, we have performed conventional and unconventional transport measurements in both Corbino samples, see Fig.3. Note that in this figure, and in the remainder of the text we opted to report and discuss the resistance $R = G^{-1}$ *versus* temperature rather than the conductance. In the unconventional configuration, the current (I_+, I_-) and voltage (V_+, V_-) probes are interchanged and this results in Corbino geometry for the current probes, somewhat counterintuitively, to be connected to intermediate rings, and the voltage probes to the most outer and inner contacts, see Fig.3a. The reciprocity theorem of electromagnetism which traces its roots to Maxwell's equations (and has been connected to Onsager's relations by Casimir [6]) states that both configurations should yield the same measurement. This holds true for passive circuits that are composed of linear media and for which time-reversal symmetry is not broken. Our reciprocity measurements are shown in Fig.3b and c, with the data shown in magenta taken in the unconventional configuration. Except for the higher noise floor, the measurements clearly satisfy the reciprocity theorem, adding strength to the observation of anomalous transport in the multi-terminal Corbino samples.

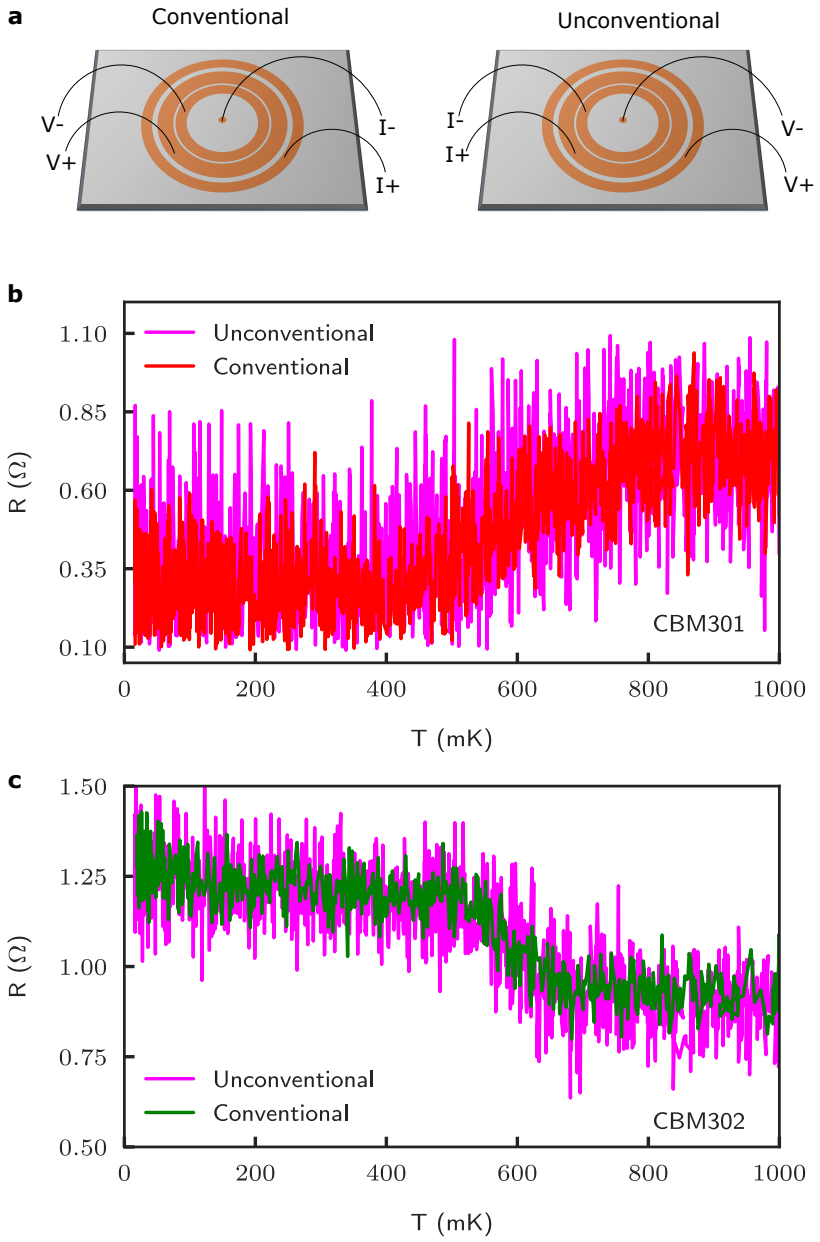

Figure 3 – Conventional and unconventional resistance measurement. **a** Schematics of the current-voltage probe terminal used for conventional (left) and unconventional (right) measurements. In the unconventional case, the current (I_+, I_-) and voltage (V_+, V_-) leads are interchanged, with the current leads connected to the inner Corbino rings. The resistance measured *versus* temperature for CBM301 (panel **b**) and CBM302 (panel **c**) is shown for both cases, with the data in magenta denoting the unconventional configuration. The reciprocity relations are clearly validated in both Corbino samples.

3.4.5 Comparison of Corbino and van der Pauw Measurements

van der Pauw measurements were performed to determine the bulk resistivity of each parent heterostructure. Fig.4a and b shows the resistance measured in both Corbino and VdP samples up to 10 K temperature on a semi-log scale. The resistance of VdP301 shows a very slight decrease up to 2 K which is then followed by the expected monotonic increase due to scattering with phonons. This behavior

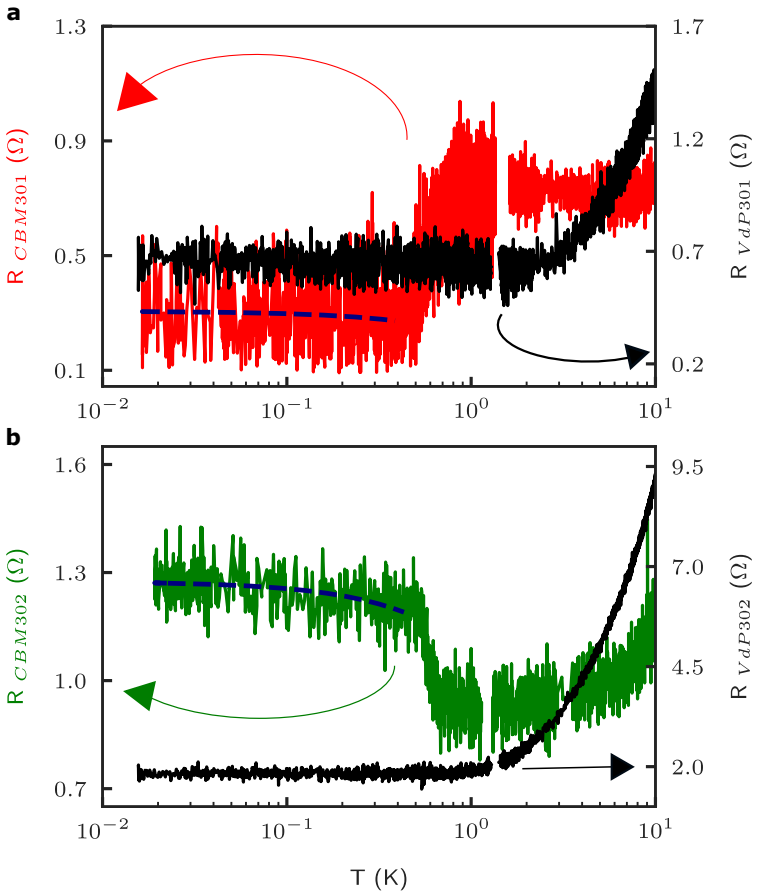

Figure 4 – Temperature dependence of Corbino and van der Pauw resistance (VdP). The temperature dependence of the measured Corbino resistance is compared with the resistance measured in VdP cut from wafers with the exact same heterostructure. Panel **a** shows resistance measured for CBM301 (red) and VdP301 (black). Panel **b** shows the resistance measured for CBM302 (green), and VdP302 (black). A guide-to-the-eye blue dash line shows the moving average of the resistance at low temperature for CBM301 and CBM302.

is drastically distinct from CBM301 which exhibits a sudden increase in resistance at $\sim$400 mK, followed by a saturation over a wide range of temperatures, up to $\sim$10 K. In the case of VdP302, the increase in resistance due to phonons onsets near 1 K, and as expected is followed by a monotonic increase with temperature, see Fig.4b. This greatly contrasts with the sudden decrease in resistance observed in CBM302 near $\sim$500 mK, followed by a saturation up to a temperature of $\sim$3 K where a monotonic increase with temperature is observed. We also note that in all cases the resistance is nearly constant at temperatures below $\sim$0.5 K, as expected in very high-mobility GaAs/AlGaAs 2DEGs, hence ruling out the anomalous behaviour in electronic transport observed being caused by a percolation process (metal-insulator transition). Recent work also found that under some conditions NiGeAu could be superconducting with a transition temperature around $\sim$700 mK and a critical field of $\sim$0.15 T [7,8]. In order to investigate if a supercurrent and/or a proximity effect could have played a role in our transport measurements, two-terminal and four-terminal differential resistance measurements under a DC current bias were performed at base temperature of the dilution refrigerator ($T \sim 20$ mK) and the $I-V$ obtained were found to be linear (ohmic). In addition, we have performed magneto-transport measurements in a perpendicular field near the expected critical field 0.15 T (also at base temperature) and found no evidence of superconductivity in either samples, see SM. Finally, additional electronic transport data up to 100 K in the Corbino and up to 10 K in the VdP samples are provided in the SM that illustrates the distinctive behaviour between the VdP and CBM samples at temperatures below a few Kelvins.

3.5 Discussion

3.5.1 Transport Lengthscales

As discussed in Ref. [4], the relevant lengthscales that are impacting the bulk resistivity of a high-mobility 2DEG are: (A) The momentum-conserving mean free

path due to electron-electron interaction, l_{ee}; (B) the momentum-relaxing mean free path due to electron scattering with both impurities and phonons, l_e; and (C) the width of the annular region forming the transport channel which is $L_{Corbino} = 40\ \mu m$ in our case. When phonons contribute negligibly to electron scattering, which has been shown to be the case below 1 K temperature [9], the momentum-relaxing mean free path l_e can be calculated from the mobility and electron density, $l_e = 5.22 \times \mu\sqrt{n}$. Owing to the very high-mobility of the 2DEG used here, this lengthscale is exceedingly larger than the channel transport length, yielding ∼271 μm in CBM301 and ∼138 μm in CBM302.

Within Fermi liquid theory, Ahn and Das Sarma [4] calculated from first principles the momentum-conserving mean free path l_{ee} for 2DEGs with similar density and with an electron mobility of $1 \times 10^6\ cm^2/(V\ s)$. In particular, they found that for a 2DEG with a density $1.5 \times 10^{11}\ cm^{-2}$ (similar to CBM302) the momentum-conserving mean free path l_{ee} falls below 40 μm at temperatures above $\sim 550\ mK$. At a higher electron density of $2.5 \times 10^{11}\ cm^{-2}$ (close to CBM301), this occurs at a temperature of ∼850 mK and so the condition $l_{ee} < L_{Corbino} \ll l_e$ can occur within a finite temperature interval for both CBM301 and CBM302 with a negligible phonon contribution to resistivity, *i.e.* until l_e is reduced due to phonon scattering and becomes comparable to either l_{ee} or $L_{Corbino}$.

3.5.2 Knudsen Parameter, Ballistic Transport and Hydrodynamics

In fluids, when a liquid or a gas flow through an aperture, distinctive flow regime can be classified by a dimensionless parameter known as the Knudsen number $K_n = \lambda/D$. Here, λ is the mean free path of the fluid's constituent and D is the diameter of the aperture or fluid channel. As a function of K_n, a classical fluid can transit from (effusive) single-particle transport following kinetic theory of statistical mechanics at high Knudsen number ($K_n \gg 1$), to a continuous hydrodynamic flow

governed by the Navier-Stokes at low Knudsen number ($K_n \ll 1$), see Ref. [10] for a simple experimental demonstration in the case of a gas flowing through a small aperture.

In electronic systems such as two-dimensional electron gases, both transport regimes are in principle possible although the realization of hydrodynamic flow has proven to be challenging to observe experimentally. In their study of transport-relevant lengthscales in high-mobility 2DEGs, Ahn and Das Sarma [4] have defined a dimensionless Knudsen parameter, $\zeta \equiv l_{ee}/l_e$, which also marks the crossover from ballistic (or effusive) flow when $\zeta \gg 1$, to the hydrodynamic regime in a continuum when $\zeta \ll 1$. Interestingly, this ζ parameter falls below 0.5 at temperatures above 500 mK for both CBM301 and CBM302, hinting strongly to the occurrence of hydrodynamic transport in a regime where phonons play very little, or no role at all. We note that the sharp drop in resistance at $\sim$500 mK observed in CBM302 occurs when $l_{ee} < L_{Corbino}$ and $\zeta \ll 1$, suggestive of a hydrodynamic flow caused by increased electron-electron interaction. To our knowledge, this sharp drop (increase) observed in CBM302 (CBM301) in resistivity with increasing temperature below 1 K has never been observed before in any high-mobility 2DEGs. Moreover, this is surprising given the transport channel length in the Corbino being 40 μm long, and for which a priori one would assume to be well within the bulk regime of 2D electronic flow.

3.5.3 Gurzhi Effect?

The prediction by Gurzhi that a Fermi liquid metal can have a decreasing resistance with increasing temperature due to hydrodynamic flow has been notoriously difficult to realize in 3D metals, with the end result that very little progress has been made on the topic for decades. Only over the last few years there has been experimental report of hydrodynamic behaviour in 3D materials [11,12]. In 2D semiconductors, materials have long been made with astonishingly high-electron mobility and hence extremely long mean free path. In spite of this, reports of hydrodynamic flow have

been scarce, with the first claim made roughly thirty years ago (and only one for many years) in GaAs quantum wires [13]. More recent works have focused on bilayers [14], strongly-correlated 2D hole systems [15], non-local measurements [16,17] including an extensive study of the conductivity in GaAs/AlGaAs channel with smooth sidewalls and perfect slip boundary condition [18], graphene [19–22], graphene Corbino rings [23] as well as theoretical interest of hydrodynamic flow in Corbino geometries [24–27]. But to the best of our knowledge, there has been no report to date of a direct observation of Gurzhi's prediction of a super ballistic-to-hydrodynamic electron flow when phonons play very little, or no role at all.

The Gurzhi effect occurs when the electron flow is neither diffused by impurity scattering nor by single-particle transport events but is rather the result of the formation of a continuum and collective transport properties described by hydrodynamics. In principle, this effect can be observed in the resistivity of a clean Fermi liquid metal up to a temperature where the increasing electron-phonon interaction becomes important and leads to a non-negligible scattering sources. Rather stunningly, the resistance observed below $\sim 1\ K$ in CBM302 shows a great similarity with the resistance curve predicted and plotted by Gurzhi in his original work [2]. This possibility is further supported by the ζ value calculated which would indicate the electron flow to be in the hydrodynamic regime. This being said, in the case of CBM301 whose higher electron density leads to a smaller r_s parameter and hence with decreased electron interaction when compared to CBM302, the sudden increase in resistance around 400 mK with temperature cannot be explained solely by arguments based on hydrodynamic flow, nor by any obvious electron-phonon scattering mechanisms.

A recent study conducted on spatial mapping of local electron density fluctuation in a high-mobility GaAs/AlGaAs 2DEG by way of scanning photoluminescence [28] reported electron density variations up to 100 μm with a spot size of 40 μm. These fluctuations are likely to generate local electron mobility fluctuations, and we hypothesize that it could perhaps play a role in a Corbino measurement

scheme because there is no edge and the concentric sample can be viewed as a very large number of conductors wired in parallel. This being said, whether a higher conductance path due to a local spatial fluctuation in the electron density (or mobility) would occur, and lead to the anomalous electronic transport observed in both CBM301 and CBM302 remains an open question. This will be the subject of future works.

In this work, we have performed four-terminal electronic transport measurements in two very-high mobility Corbino 2DEG rings with distinct electron density and identical annular channel length of 40 μm. In both cases, anomalous transport was observed in the temperature dependence of the resistance at temperatures below 1 K where phonons are expected to play a negligible or no role at all. The discovery of a sharp decrease in resistance with increasing temperature in the lower density sample is stunning, and even more so since the estimated Knudsen parameter hints at a Gurzhi effect and a crossover from super-ballistic to hydrodynamic flow. Nevertheless, this sharp decrease in resistance contrasts with the trend observed at a similar temperature in the higher electron density sample, and for which we have no clear explanation as for its origin. At temperatures above 10 K, we have shown that in both cases the expected monotonic temperature dependence of the resistance is recovered and is similar in trend to that measured in larger millimetre size VdP samples. While the exact mechanism leading to the anomalous electronic transport observed here remains an open question, this work demonstrates that a 40 μm channel length is not bulk in high mobility 2DEGs since both the momentum-conserving and momentum-relaxing mean free path values are either larger, or equal to the channel length in the 20 mK to $\sim$1 K temperature range. Looking forward, confirmation of hydrodynamic flow in GaAs/AlGaAs could allow us to study the remarkable properties of the anti-symmetric part of a viscosity tensor, known as the Hall viscosity [29, 30], a dissipationless viscosity existing even at zero temperature that has no classical equivalent whatsoever.

3.6 Methods

3.6.1 Experimental Design and Procedure

The measurements were performed on GaAs/AlGaAs symmetrically-doped heterostructures with a quantum well width of 30 nm (CBM301, VdP301) and 40 nm (CBM302, VdP302. A sketch of the heterostructure that include the main growth parameters such as the setback distances for the dopants and the capping layer thickness is provided in the supplementary material (SM) for both samples. The electron density of CBM301 and VdP301 is 3.6×10^{11} cm^{-2}, and for CBM302 and VdP302 is 1.7×10^{11} cm^{-2}, as determined by magneto-transport measurements of Shubnikov de-Haas (SdH) oscillations at low magnetic fields, see SM. Their mobilities are 27.8×10^6 $cm^2(Vs)^{-1}$ and 20.3×10^6 $cm^2(Vs)^{-1}$, respectively. The contacts for the Corbino samples were patterned using UV lithography followed by e-beam deposition of Ge/Au/Ni/Au layers of 26/54/14/100 nm thickness and at a $1 - 2$ A s^{-1} rate. Subsequently, the contacts were annealed in H2N2 atmosphere using a two step annealing procedure: a 20 s first step at 370 $°C$ followed by a longer 80 s step at 440 $°C$ [31, 32]. Both Corbino samples have three 2DEG rings with inner/outer radii (150/750) μm, (960/1000) μm, and (1300/1400) μm, respectively, see Fig.2.1a. One van der Pauw sample was cleaved from the exact same wafer used to fabricate CBM302, and from a twin wafer with an identical heterostructure grown on the same day for CBM301. They are 3×3 mm square wafers with eight diffused indium contacts around the perimeter. All samples were cooled to a base temperature of approximately 20 mK in a dilution refrigerator, and were illuminated by a red LED from room temperature down to approximately 6 K to increase both the mobility and density of the 2DEG. Specific details pertaining to the circuit used to perform the transport measurements are provided in the SM.

3.7 References

[1] Chung, Y. J., Gupta, A., Baldwin, K. W., West, K. W., Shayegan, M. and Pfeiffer, L. N. Understanding limits to mobility in ultrahigh-mobility GaAs two-dimensional electron systems: 100 million cm^2/Vs and beyond, Phys. Rev. B **106**, 075134 (2022).

[2] Gurzhi, R. N., Minimum of resistance in impurity-free conductors, Sov. Phys. JETP **17**, 521 (1963).

[3] Gurzhi, R. N., Hydrodynamic effects in solids at low temperature, Sov. Phys. Usp. **11**, 255 (1968).

[4] Ahn, Seongjin and Das Sarma, Sankar, Hydrodynamics, viscous electron fluid, and Wiedeman-Franz law in two-dimensional semiconductors, Phys. Rev. B **106**, L081303 (2022).

[5] Umansky, V., de-Picciotto, R. and Heiblum, M., Extremely high-mobility two dimensional electron gas : Evaluation of scattering mechanisms, Appl. Phys. Lett. **71**, 683 (1997).

[6] Casimir, H. B. G., reciprocity theorems and irreversible processes, IEEE **51**, 1570 (1963).

[7] Beauchamp, C. B., Dimitriadis, S., Nicholls, J. T., Levitin, L. V., Casey, A. J., See, P., Creeth, G., Waldie, J., Farrer, I., Beere, H. E. and Ritchie, D. A., Superconductivity in AuNiGe Ohmic contacts to a GaAs-based high mobility two-dimensional electron gas, Appl. Phys. Lett. **117**, 162104 (2020).

[8] Levitin, L. V., Theisen, T., Dimitriadis, S., Lucas, M., Corcoles, A. D., Nyéki, J., Casey, A. J., Creeth, G., Farrer, I., Ritchie, D. A., Nicholls, J. T. and Saunders, J., Cooling low-dimensional electron systems into the microkelvin regime, Nat. Commun. **13**, 1-8 (2022).

[9] Hwang, E. H. and Das Sarma, S., Limit to two-dimensional mobility in modulation-doped GaAs quantum structures : How to achieve a mobility of 100

million, Phys. Rev. B **77**, 235437 (2008).

[10] Savard, M., Tremblay-Darveau, C. and Gervais,G., Flow conductance of a single nanohole, Phys. Rev. Lett. **103**, 104502 (2009).

[11] Gooth, J., Menges, F., Kumar, N., Shekhar, C., Sun, Y., Drechsler, U., Zierold, R., Felser, C. and Gotsmann, B.,Thermal and electrical signatures of a hydrodynamic electron fluid in tungsten diphosphide, Nat. Commun. **9**, 4093 (2018).

[12] W. Moll, P. J., Kushwaha, P., Nandi, N., Schmidt, B., and Mackenzie, A. P., Evidence for hydrodynamic electron flow in PdCoO2, Science **351**, 1061 (2016).

[13] de Jong, M. J. M. and Molenkamp, L. W., Hydrodynamic electron flow in high-mobility wires, Phys. Rev. B **51**, 13389 (1995).

[14] Gusev, G. M., Jaroshevich, A. S., Levin, A. D., Kvon, Z. D. and Bakarov, A. K., Viscous magnetotransport and Gurzhi effect in bilayer electron system, Phys. Rev. B **103**, 075303 (2021).

[15] Kumar, A. S., Liu, C., Liu, S., Pfeiffer, L. N., West, K. W., Levchenko, A., and Gao, X. P., Interaction effects and viscous magneto-transport in a strongly correlated 2D hole system, arXiv:2105.06502v1.

[16] Gusev, G. M., Levin, A. D., Levinson, E. V. and Bakarov, A. K., Viscous electron flow in mesoscopic two-dimensional electron gas, AIP Adv. **8**, 025318 (2018).

[17] Gupta, A., Heremans, J. J., Kataria, G., Chandra, M., Fallahi, S., Gardner, G. C. and Manfra, M. J., Hydrodynamic and Ballistic Transport over Large Length Scales in GaAs/AlGaAs, Phys. Rev. Lett. **126**, 076803 (2021).

[18] Keser, A. C., Wang, D. Q., Klochan,O., Ho, D. Y. H., Tkachenko, O. A., Tkachenko, V. A., Culcer, D., Adam, S., Farrer, I., Ritchie, D. A., Sushkov, O. P., and Hamilton, A. R., Geometric control of universal hydrodynamic flow in a two-dimensional electron fluid, Phys. Rev. X **11**, 031030 (2021).

[19] Krishna Kumar, R.,Bandurin, D. A., Pellegrino, F. M. D., Cao, Y., Principi, A., Guo, H., Auton, G. H., Ben Shalom, M., Ponomarenko, L. A., Falkovich, G., Wa-

tanabe, K., Taniguchi, T., Grigorieva, I. V., Levitov, L. S., Polini, M.and Geim, A. K., Superballistic flow of viscous electron fluid through graphene constrictions, Nat. Phys. **13**, 1182-1185 (2017).

[20] Bandurin, D. A., Shytov, A. V., Levitov, L. S., Kumar, R. K., Berdyugin, A. I., Ben Shalom, M., Grigorieva, I. V., Geim, A. K. and Falkovich, G., Fluidity onset in graphene, Nat. Commun. **9**, 4533 (2018).

[21] Ku, M. J., Zhou, T. X., Li, Q., Shin, Y. J., Shi, J. K., Burch, C., Anderson, L. E., Pierce, A. T., Xie, Y., Hamo, A., Vool, U., Zhang, H., Casola, F., Taniguchi, T., Watanabe, K., Fogler, M. M., Kim, P., Yacoby, A., and Walsworth, R. L., Imaging viscous flow of the Dirac fluid in graphene, Nat. Phys. **583**, 537-541 (2020).

[22] Jenkins, A., Baumann, S., Zhou, H., Meynell, S. A., Daipeng, Y., Watanabe, K., Taniguchi, T., Lucas, A., Young, A. F., and Bleszynski Jayich, A. C., Imaging the breakdown of Ohmic transport in graphene, Phys. Rev. Lett. **129**, 087701 (2022).

[23] Kumar, C., Birkbeck, J., Sulpizio, J. A., Perello, D., Taniguchi, T., Watanabe, K., Reuven, O., Scaffidi, T., Stern, A., Geim, A. K., and Ilani, S., Imaging hydrodynamic electrons flowing without Landauer–Sharvin resistance, Nature **609**, 276-281 (2021).

[24] Shavit, M., Shytov, A. and Falkovich, G., Freely flowing currents and electric field expulsion in viscous electronics, Phys. Rev. Lett. **123**, 026801 (2019).

[25] Li, Songci , Levchenko, A. and Andreev, A. V., Hydrodynamic thermoelectric transport in Corbino geometry, Phys. Rev. B **105**, 125302 (2022).

[26] Levchenko, A., Li, Songci and Andreev, A. V., Hydrodynamic magnetoresistance in graphene Corbino devices, Phys. Rev. B **106**, L201306 (2022).

[27] Narozhny, Boris N., Hydrodynamic approach to two-dimensional electron systems, Riv. Nuovo Cim. **45**, 661–736 (2022).

[28] Chung, Yoon Jang, Baldwin, K. W., West, K. W., Haug, N., van de Wetering, J., Shayegan, M. and Pfeiffer, L. N., Spatial mapping of local density variations

in two-dimensional electron systems using scanning photoluminescence, Nano Lett. **19**, 1530-6984 (2019).

[29] Avron, J. E., Seiler, R. and Zograf, P. G., Viscosity of quantum Hall fluids, Phys. Rev. Lett. **75**, 697-700 (1995).

[30] Holder, T., Queiroz, R. and Stern, A., Unified description of the classical Hall viscosity, Phys. Rev. Lett. **123**, 106801 (2019).

[31] Schmidt, B. A., Bennaceur, K., Bilodeau,S., Gervais, G., Pfeiffer, L. N., and West, K. W.,Second Landau level fractional quantum Hall effects in the Corbino geometry, Solid State Communications **217**, 1 (2015).

[32] Bennaceur, K. and Lupien, C. and Reulet, B. and Gervais, G. and Pfeiffer, L. N. and West, K. W., Competing charge density waves probed by nonlinear transport and noise in the second and third Landau levels, Phys. Rev. Lett.**120**, 136801(2018).

4

Two-dimensional hydrodynamic viscous electron flow in annular Corbino rings

4.1 Preface

The previous chapter detailed our findings from local transport measurements conducted on two ultra-high mobility devices, where we identified signatures of the Gurzhi effect in one of the samples, CBM302. As introduced in Chapter 2, nonlocal measurements conducted in vicinity geometries yield a negative potential [61,68] due to the backflow of current in the hydrodynamic regime. Further studies revealed that ballistic electron transport can also produce a negative nonlocal potential. However,

the temperature dependence of these nonlocal potentials differs between the ballistic regime and the hydrodynamic regime [10].

In this Chapter, we expand our investigation from local to nonlocal transport. Unlike traditional vicinity geometries, where viscosity can induce a backflow of current, the nonlocal signal obtained from Corbino devices results from a different manifestation of viscous flow. In Corbino geometry, the current flows radially at zero magnetic field. In the viscous regime, viscous electron drag can cause the current to extend beyond the contact. The results presented here provide further support for our hypothesis of hydrodynamic transport in CBM302 in contrast to its absence in CBM301. These findings are compared with numerical simulations based on the Navier-Stokes equation performed by another member of the Gervais Lab.

The manuscript included in this chapter, titled *"Two-Dimensional Hydrodynamic Viscous Electron Flow in Annular Corbino Rings"*, is identical to the version submitted to Physical Review Letters and is currently under review. It is also available on arXiv [18]. The figure labels and reference numbering follow the posted manuscript on the *arXiv* and are independent of the rest of the thesis. Supplementary material, including discussions on hydrodynamic reciprocity and probe symmetry, is provided in Appendix C.

4.2 Abstract

The concept of fluidic viscosity is ubiquitous in condensed matter systems hosting a continuum where macroscopic properties can emerge. While an important property of liquids and some solids, only recently the viscosity of electron was shown to play a role in electronic transport experiments. In this letter, we present nonlocal electronic transport measurements in concentric annular rings formed in high-mobility 2DEGs, and the resulting data shows that viscous hydrodynamic flow can occur far away from the source-drain current region. Our conclusion of viscous electronic transport is further corroborated by simulations of the Navier-Stokes equa-

tions that are found to be in agreement with our measurements below $T = 1\ K$. Finally, this work emphasizes the key role played by viscosity via electron-electron $(e - e)$ interaction even when the electronic transport is restricted radially, and for which *a priori* should have played no major role.

4.3 Introduction

Consider a gas moving through a small constriction: depending on the density of the gas, flow out of the chamber can vary significantly due to the varying mean-free path of its constituent particles. If the mean-free path greatly exceeds the hole size, individual gas particles will diffuse independently with their own trajectories, akin to single-particle effusive transport. Conversely, if the mean free path is much smaller than the hole size, the particles will interact more frequently, ultimately leading to a collective flow guided by the broader dynamics of the ensemble and forming a continuum. When this is the case, the flow properties of neutral fluids are typically governed by the Navier-Stokes equations of hydrodynamics, which holds true for the flow of water and other fluids that are ubiquitous in our everyday life.

In the case of electrons in metals governed by Fermi liquid theory, somewhat oppositely single particle theoretical descriptions are most often used, neglecting electron viscosity arising from a possible continuum. In narrow graphene constrictions, however, collective effects were shown experimentally to be important under the form of current backflow, forming whirlpools of electrons [1]. Recently, Ahn and Das Sarma [2] further proposed that hydrodynamic effects should be observable in the bulk of moderately high electron mobility GaAs/AlGaAs two-dimensional electron gases (2DEGs), provided their scattering parameters place them into a collective regime. In this letter, we present local and nonlocal electronic transport measurements in annular regions formed in GaAs/AlGaAs 2DEGs that have no edges and are therefore entirely bulk. Numerical simulation based on the Navier-Stokes equations for a charged fluid that includes the electron viscosity proposed by Polini and

co-workers [3] is found to be in good agreement with experimental results, hence confirming the significance of electron viscosity and viscous drag far away from the source-drain current region.

4.4 Lengthscales and Hydrodynamic Electron Transport

In the regime of clean conductors, such as high-mobility 2DEGs, momentum scattering is dominated by electron-electron ($e-e$) interactions, where the mean-free path due to these interactions (ℓ_{MC}) is much smaller than both the conducting channel width (W) as in a Hall bar geometry and the momentum relaxing mean-free path (ℓ_{MR}) from either impurity or phonon scattering. In the case where $\ell_{MC} \ll W \ll \ell_{MR}$, a collective behaviour of electrons can emerge, that resembles a fluid-like continuum rather than discrete single particle effusive motion. This type of electronic transport is commonly referred to as hydrodynamic transport. This transport regime in metals was first theorized by R. N Gurzhi [4, 5] in 1963, and it offers a more complete perspective on electronic transport wherein the resistance to flow is governed by the fluidic viscosity of the electron stream and the geometric characteristics of the conducting channel. This has recently led to a renewed interest in the study of hydrodynamics in electronic systems, and blossomed into a series of theoretical [1–3, 6–14] and experimental [15–26] advances.

4.5 Corbino Samples Parameters and Experimental Protocol

Typical measurements performed in large 2DEG samples utilize the four-terminal setup either in van der Pauw (VdP) or Hall bar geometries, and the latter is shown in Fig.1A for both local and nonlocal measurement configurations. The Corbino geometry shown in Fig.1B was chosen to ensure that only the bulk of the 2DEG

was probed. To avoid any contributions from the Ohmic contacts, four-terminal Corbino devices were patterned on two symmetrically doped GaAs/AlGaAs heterostructures, one with a 40 nm (CBM302) and the other with a 30 nm (CBM301) quantum well widths, see Supplementary Material (SM). The devices have electron densities of $n_e = 1.7 \times 10^{11}\ cm^{-2}$ and $n_e = 3.6 \times 10^{11}\ cm^{-2}$, and electron mobilities of $20.3 \times 10^6\ cm^2(Vs)^{-1}$ and $27.8 \times 10^6\ cm^2(Vs)^{-1}$ below 20 mK, respectively. Both Corbino devices consist of three 2DEG active rings with inner/outer radii of (150/750) μm, (960/1000) μm, and (1300/1400) μm respectively. These annular regions are defined by Ge/Au/Ni/Au layers of 26/54/14/100 nm thickness that diffuses into the wafer during an annealing process. As a result, Ohmic contacts with resistances on the order of $\sim 3\ \Omega$ are formed.

From their electron densities the $e-e$ interaction parameter $r_s = (\pi n_e a_B^2)^{-\frac{1}{2}}$, where a_B is the effective Bohr radius, were calculated to be 1.32 for CBM302 and 0.92 for CBM301, and from their electron mobilities ℓ_{MR} values were calculated to be 138 μm for CBM302 and 271 μm for CBM301. The device with a lower electron density, CBM302, has a higher r_s parameter, indicating an enhanced $e-e$ interaction compared to CBM301. The multi-terminal Corbino devices were cooled down to the base temperature $T \simeq 6\ mK$ of a dilution refrigerator, illuminated by a red LED from room temperature to approximately $T \simeq 7\ K$ to optimize the electron mobility. All nonlocal measurements presented in this work were performed with a fixed current of 100 nA applied to the two innermost rings, and the voltage difference was measured across the outermost rings.

4.6 Results

4.6.1 Local and Nonlocal Measurements

To ensure consistency, we performed both local and nonlocal measurements in both multi-terminal Corbino devices during the same cooldown, and the results are

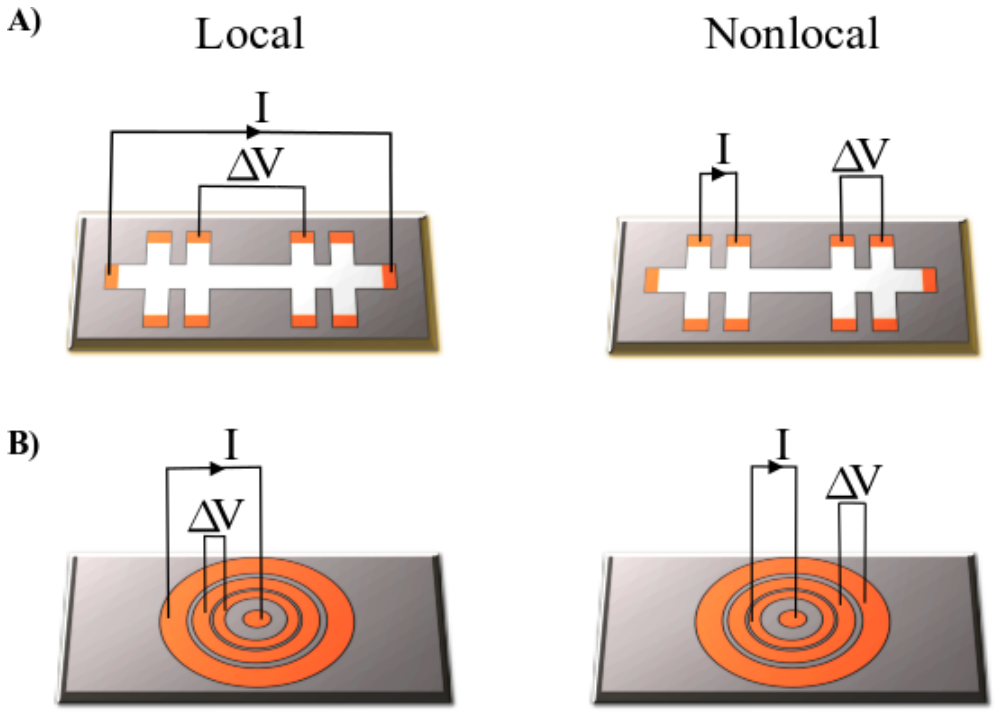

Figure 1 – Schematics of Hall bar and multi-terminal Corbino geometry. Measurement lead configurations for local and nonlocal measurements are shown in (**A**) for the Hall bar and (**B**) the Corbino geometry.

shown in Fig.2B and C. For the nonlocal measurements, a current I was applied to the two inner rings and the voltage difference ΔV_{NL} was measured across the two outer rings (the Onsager 1 (O1) configuration), and vice-versa for the Onsager 2 (O2) configuration, shown in Fig.2A. The temperature dependence of nonlocal resistance $R_{NL} \equiv \Delta V_{NL}/I$ is shown in Fig.2B by a green line for CBM302 and by a red line for CBM301 in Fig.2C, from base temperature (6 mK) to 1 K. In CBM302, a nearly constant negative nonlocal signal was measured up to $T \simeq 450$ mK, at which point a sharp increase of the negative signal occurs concomitantly with the sharp decrease in local resistance. Between temperatures $T = 450$ mK and $T = 1$ K, our measurements in CBM302 demonstrate a $\sim$160% increase in negative nonlocal signal, and a $\sim$33% decrease in local signal. As discussed below, these two observations are inconsistent with ballistic effusive electronic transport [27, 28], and rather point towards the formation of a continuum and electronic flow governed by hydrodynamics when the Knudsen number $\zeta \equiv l_{MC}/l_{MR} \lesssim 1$, as is the case here.

Consistent with our previous report [29], CBM301 shows an opposite behaviour to CBM302, and within experimental resolution the nonlocal resistance is absent except for a small positive hump occurring at $T \simeq 400\ mK$.

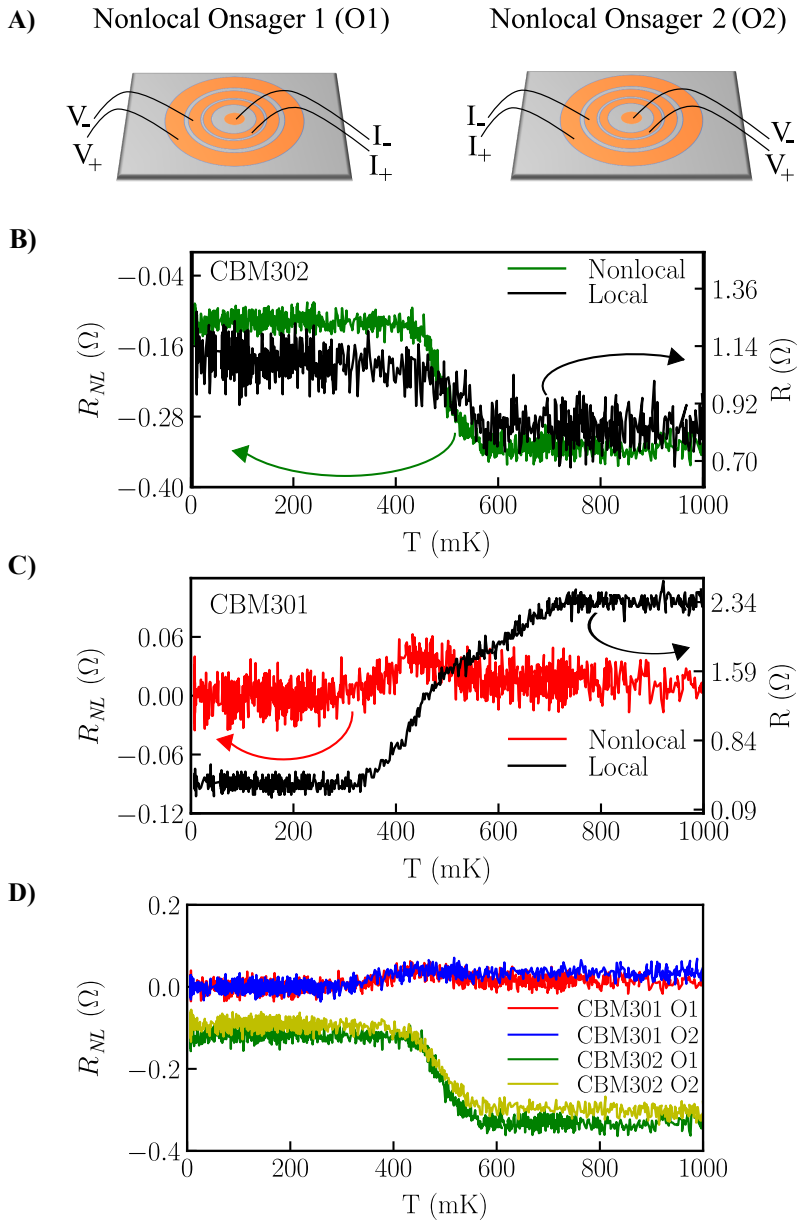

Figure 2 – Local and nonlocal transport measurements in multi-terminal Corbino 2DEGs. (**A**) Schematic representation of two distinct four-point nonlocal measurement configurations. (**B**) Nonlocal resistance measured in O1 configuration is compared with local measurements for CBM302 and (**C**) for CBM301. (**D**) Nonlocal measurements in CBM301 and CBM302 for both O1 and O2 configurations. Onsager reciprocity is validated within experimental resolution.

4.6.2 Nonlocal Reciprocity Measurements

To test the reciprocity relations, we measured the nonlocal response for both O1 and O2 configuration, see Fig.2A. Despite the smaller current-driving area and larger measurement area in the O2 configuration compared to O1, we observe no notable differences in nonlocal resistance and their temperature dependence is shown in Fig.2D. Clearly, the Onsager reciprocity relations are satisfied over the temperature range probed in our experiment, *i.e.* from $T = 6\ mK$ to $T = 1\ K$, as expected in hydrodynamic transport [30]. This also shows that the nonlocal signal is not caused by an accumulation of charges, as reciprocity measurements should have been different if the electron density remains constant between the inner and outer annular rings that have significantly different areas. In the SM, we show that the reciprocity relations are analytically satisfied for our system based on the hydrodynamic model presented in the following section. Finally, we performed probe symmetry measurements between adjacent contacts, also shown in the SM, which are all proved to be satisfied.

4.7 Discussion

4.7.1 Electron Collision and Kinetic Theory

In a continuum, the role played by individual particle states diminishes and the flow becomes governed by the transport of a macroscopic fluid ensemble of particles. When this is the case, the details of their macroscopic behaviour arise from the description of individual particle states through solving Boltzmann's Transport Equation (BTE) of kinetic theory and determining macroscopic quantities. For electron flow however, interparticle interactions become important, requiring higher-order terms for an accurate description. Macroscopically, these interactions are described as body forces acting on the collective behaviour of the system. In our case, the interaction mechanisms arise by scattering, and we consider two main forms: momentum

conserving $e-e$ scattering and momentum relaxing electron-impurity scattering, with relaxation times τ_{MC} and τ_{MR} respectively. We also omit the contribution to momentum relaxing due to electron-phonon scattering in our modelling since it has been shown to play a negligible role below a temperature of 1 K [31]. Moreover, it is known that well below 1 K, electron-impurity scattering does not depend on temperature, whereas electron-electron has an inverse square power relationship [2,32]. Despite the common misconception that momentum-conserving interactions do not affect bulk resistivity, in a Corbino device without edges our observations of a non-monotonic temperature dependent transport and the realization of Gurzhi effect must relate to momentum conserving scattering. As such, when deriving the collective behaviour from BTE, we must consider the effects of a collision integral that is non-zero under velocity space integration.

In the presence of an electric field $\vec{E}$, the linearized transport equation is [33]

$$\frac{\partial f_{\vec{v}}}{\partial t}+\vec{v}\cdot\frac{\partial f_{\vec{v}}}{\partial \vec{r}}+\frac{q_e}{m^*}\vec{E}\cdot\frac{\partial f^0_{\vec{v}}}{\partial \vec{v}}=\left(\frac{\partial f_{\vec{v}}}{\partial t}\right)_{coll}, \tag{4.1}$$

where $(\vec{v},\vec{r},t)$ is particle velocity and position at time t, $f_{\vec{v}}(\vec{v},\vec{r},t)$ is the electron distribution function, $f^0_{\vec{v}}(\vec{v},\vec{r},t)$ is the equilibrium distribution in the absence of an electric field, q_e is electron charge $-e$ and m^* is effective mass ($0.067m_e$ for GaAs/AlGaAs). Using the relaxation time approximation, momentum relaxing scattering relaxes the system to a field-less equilibrium, whereas momentum conserving scattering relaxes the system to an equilibrium where electrons drift at velocity $\vec{u}$ with distribution function $f^0_{\vec{u}}$. The collision integral then becomes

$$\left(\frac{\partial f_{\vec{v}}}{\partial t}\right)_{coll}=-\frac{f_{\vec{v}}-f^0_{\vec{v}}}{\tau_{MR}}-\frac{f_{\vec{v}}-f^0_{\vec{u}}}{\tau_{MC}}. \tag{4.2}$$

For small drift velocity, expanding $f^0_{\vec{u}}=f^0_{\vec{v}}\left(\epsilon-m^*\vec{v}\cdot\vec{u}\right)$ around static equilibrium yields

$$f^0_{\vec{u}}\approx f^0_{\vec{v}}-2\vec{u}\cdot\frac{\partial f^0_{\vec{v}}}{\partial \vec{v}}, \tag{4.3}$$

and substituting this result into Eq.4.2 gives

$$\left(\frac{\partial f_{\vec{v}}}{\partial t}\right)_{coll} = -\frac{f_{\vec{v}} - f^0_{\vec{v}}}{\tau_T} - \frac{2}{\tau_{MC}}\vec{u}\cdot\frac{\partial f^0_{\vec{v}}}{\partial \vec{v}}, \tag{4.4}$$

where $\tau_T^{-1} = \tau_{MC}^{-1} + \tau_{MR}^{-1}$ is the total mean-free time of all scattering events by Matthiessen's rule. This result is consistent with previous work in lower dimensions [7, 15, 25] and finally Boltzmann's equation now reads

$$\frac{\partial f_{\vec{v}}}{\partial t} + \vec{v}\cdot\frac{\partial f_{\vec{v}}}{\partial \vec{r}} + \left(\frac{q_e}{m^*}\vec{E} + \frac{2\vec{u}}{\tau_{MC}}\right)\cdot\frac{\partial f^0_{\vec{v}}}{\partial \vec{v}} = -\frac{f_{\vec{v}} - f^0_{\vec{v}}}{\tau_T}. \tag{4.5}$$

By taking the first velocity moment of Eq.4.5, we arrive at the Navier-Stokes equation where the third and fourth term give body force with the following scattering corrections:

$$\begin{aligned} \vec{f} &= \frac{q_e}{m^*}\vec{E} + \vec{u}\left(\frac{2}{\tau_{MC}} - \frac{1}{\tau_T}\right) \\ &= -\frac{q_e}{m^*}\vec{\nabla}\phi + \frac{\vec{u}}{\tau}, \end{aligned} \tag{4.6}$$

where $\tau^{-1} = \tau_{MC}^{-1} - \tau_{MR}^{-1}$ and $\vec{E} = -\vec{\nabla}\phi$. This macroscopic description of the body force originating from the single-particle picture will be shown below to be of paramount importance for the nonlocal electronic transport observed in the hydrodynamic regime.

4.7.2 Hydrodynamics and Electron Viscosity

The Navier-Stokes equation of hydrodynamics for incompressible flow can be written as

$$\vec{\nabla}\cdot\vec{u} = 0, \tag{4.7}$$

$$\frac{\partial \vec{u}}{\partial t} + \left(\vec{u}\cdot\vec{\nabla}\right)\vec{u} = \nu\vec{\nabla}^2\vec{u} + \vec{f}. \tag{4.8}$$

In our case, $\vec{u}$ describes the electron drift velocity, $\nu = \frac{v_f \ell_{MC}}{4}$ is the electron viscosity [3] with v_f the Fermi velocity, and $\vec{f}$ is the body force per unit mass given by Eq.(4.6). For a steady state flow ($\frac{\partial \vec{u}}{\partial t} = 0$), we can re-write Eq.(4.8) as

$$\left(\vec{u} \cdot \vec{\nabla}\right) \vec{u} = \nu \vec{\nabla}^2 \vec{u} - \frac{q_e}{m^*} \vec{\nabla} \phi + \frac{\vec{u}}{\tau}. \tag{4.9}$$

At zero magnetic field, $\vec{u} = (u_r, 0, 0)$ in polar coordinates for the Corbino geometry [34]. As shown in the SM, analytic solutions to Eq.4.7 and Eq.4.9 give the general forms of u_r and ϕ as

$$u_r \propto \frac{1}{r}, \quad \phi \propto \tau^{-1} \log(r), \tag{4.10}$$

and as a result when the steady-state solution of u_r is substituted into Eq.(4.8), the viscosity term $\nu \vec{\nabla}^2 \vec{u}$ disappears.

Although this may seem unusual as it would suggest that viscosity plays no role at first glance, viscosity is responsible for resisting radial shear deformations, where fluid layers move at different speeds along the direction of motion. This shear deformation occurs due to radial velocity gradients, such as those seen in the discontinuous motion at contact boundaries in Ohmic transport, and causes the flow to extend beyond the discontinuity. It is only at this point that the viscosity term truly does drop out. As flow beyond the boundary is a direct result of this viscosity term, one would expect an explicit dependence of ν in the electric potential profile ϕ. In our model, this manifests as the dependence of ℓ_{MC} in τ, which is directly related to ν and depends greatly on temperature below 1 K. A distinct feature of radial hydrodynamic transport, viscous electron flow can now extend beyond the source-drain region and be experimentally probed.

4.7.3 Navier-Stokes Simulation and Comparison with Experiment

To confirm our findings, we modelled the electronic system using the Navier-Stokes equations (4.7) and (4.8). We performed simulations of these equations for nonlocal configurations in CBM301 and CBM302 from base temperature to $T = 1\ K$. In this configuration, simulations are extended from the active simulation region (the current path) to the outer rings through extrapolation, by fitting drift velocity $\vec{u}$ and electric potential ϕ to general functions resembling Eq.(4.10). This extrapolation technique is verified by simulating the entire region, and is shown in section 5.3 of SM. To obtain the voltage difference, we subtracted electric potential from edge-to-edge of each contact, using the configuration shown in Fig.2A O1. As the ohmic contacts are made by diffusion, the metal-rich phases penetrate the heterostructure and one may wonder if it obstructs the 2DEG. In an extensive study of diffusion by way of transmission electron microscopy (TEM) and energy dispersive X-ray (EDX) spectroscopy, it was concluded [35] that the annealing produces a highly doped region within the 2DEG, making the Schottky barrier very thin. As a result, 2DEGs with heterostructures similar to those presented in our work can retain their electronic transport characteristics. While this obstruction likely induces disorder to some unknown degree and could modify the profile of ϕ within the contact region, by taking the edge-to-edge potential difference, the overall effect of the obstruction drops out.

The temperature dependence of simulated values of the nonlocal potential are shown in Fig.3D together with the experimental values of potential difference measured. While the simulation does not capture the negative nonlocal potential observed below $\sim$ 300 mK temperature in the super ballistic transport regime, it nevertheless semi-quantitatively explains the strong (weak) nonlocal voltages observed in CBM302 (CBM301) between 450 mK and 1 K. Furthermore, the obtained simulation value of $-7.4 \pm 0.1\ nV$ for CBM301 at $T = 1\ K$ confirms the near-zero nonlocal

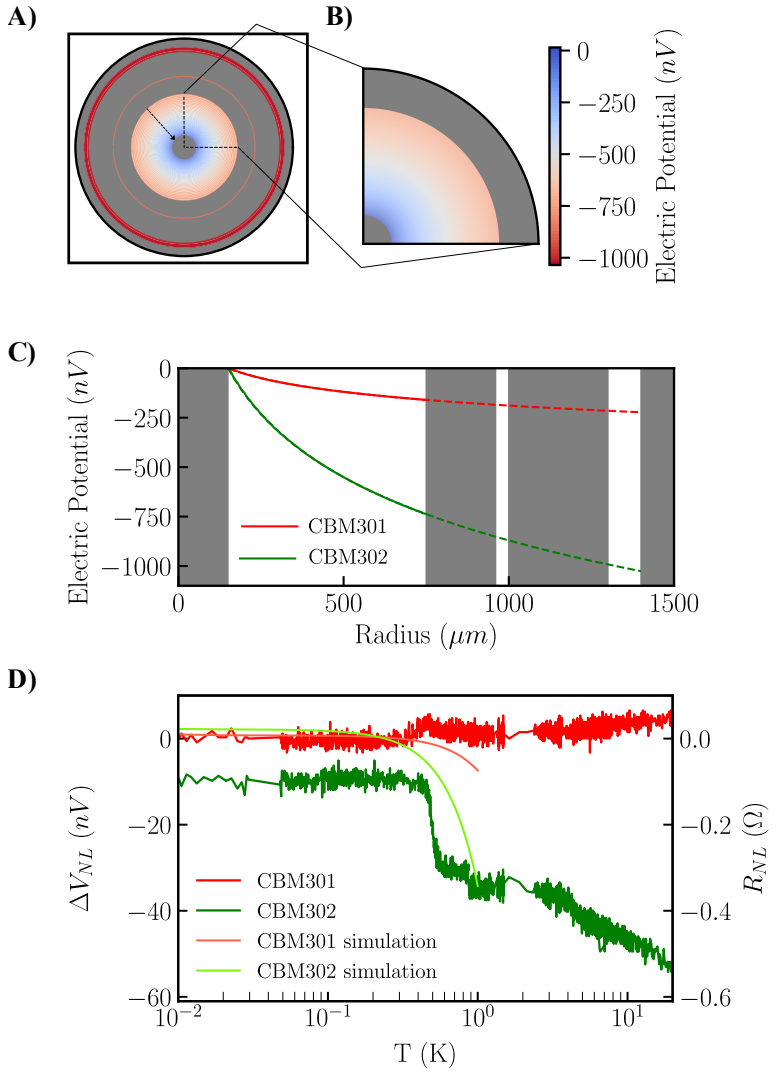

Figure 3 – Nonlocal simulation results. Simulation results are shown with the center contact as the grounding reference point. (**A**) The results of nonlocal simulation for CBM302 with shaded regions representing Ohmic contacts. (**B**) A zoom in of the active simulation region. (**C**) Results for both CBM301 and CBM302 along the central axis, with the dotted lines indicated the region of extrapolation. Ohmic contacts are shaded grey. (**D**) Comparison with simulated and experimental results for both devices is shown.

resistance in our experimental data is not a result of dominant hydrodynamic transport. Finally, for temperatures well above 1 K, we verified that including phonon contributions to resistances by adding experimentally determined electron-phonon scattering rates to our model [36] restored the expected behavior, *i.e.* a monotonic increase in resistance towards a positive value.

4.8 Conclusion

We have observed non-zero local and nonlocal voltages found to be akin to a Gurzhi effect, albeit in the bulk in a 2DEG Corbino device with high $e-e$ interaction that meets the length scale criteria for hydrodynamic transport, *i.e. at Knudsen number* $\zeta \lesssim 1$. The nonlocal signal was found to be nearly absent in a lower $e-e$ interaction device that failed to meet the same length scale criteria in a similar temperature range of investigations. Due to the bulk nature of electronic transport in the Corbino geometry and considering the Navier-Stokes equations, we conclude that the body force of carriers plays an integral role in dictating the flow of electrons, and necessarily contains the electron viscosity. This is turn allows viscous drag flow to extend beyond the contact boundary, as is observed in the experiment. Looking forward, our confirmation of hydrodynamic transport in GaAs/AlGaAs Corbino rings may allow the probing of Hall viscosity, an intriguing dissipationless bulk property arising from the odd symmetry of the viscosity tensor in two dimensions [8].

4.9 References

[1] D. A. Bandurin, I. Torre, R. Krishna Kumar, M. Ben Shalom, A. Tomadin, A. Principi, G. H. Auton, E. Khestanova, K. S. Novoselov, I. V. Grigorieva, L. A. Ponomarenko, A. K. Geim, and M. Polini, Science **351**, 1055 (2016).

[2] Seongjin Ahn and Sankar Das Sarma, Phys. Rev. B **106**, L081303 (2022).

[3] I. Torre, A. Tomadin, A. K. Geim, and M. Polini, Phys. Rev. B **92**, 165433 (2015).

[4] R. N. Gurzhi, Sov. Phys. JETP **17**, 521 (1963).

[5] R. N. Gurzhi, Sov. Phys. Usp. **11**, 255 (1968).

[6] F. M. D Pellegrino, T. Torre, A. K. Geim, and M. Polini, Phys. Rev. B **94**, 155414 (2016).

[7] T. Scaffidi, N. Nandi, B. Schmidt, A. P. Mackenzie, and J. E. Moore, Phys. Rev. Lett. **118**, 226601 (2017).

[8] T. Holder, R. Queiroz, and A. Stern, Phys. Rev. Lett. **123**, 106801 (2019).

[9] J. Crossno, J. K. Shi, K. Wang, X. Liu, A. Harzheim, A. Lucas, S. Sachdev, P. Kim, T. Taniguchi, K. Watanabe, T. A. Ohki, and K. C. Fong, Science **351**, 1058 (2016).

[10] D. A. Bandurin, A. V. Shytov, L. S. Levitov, R. Krishna Kumar, A. I. Berdyugin, M. Ben Shalom, I. V. Grigorieva, A. K. Geim, and G. Falkovich, Nat. Commun **9**, 4533 (2018).

[11] L. Levitov, and G. Falkovich, Nat. Phys. **12**, 672 (2016).

[12] R. Krishna Kumar, D. A. Bandurin, F. M. D. Pellegrino, Y. Cao, A. Principi, H. Guo, G. H. Auton, M. Ben Shalom, L. A. Ponomarenko, G. Falkovich, K. Watanabe, T. Taniguchi, I. V. Grigorieva, L. S. Levitov, M. Polini, and A. K. Geim, Nat. Phys. **13**, 1182 (2017).

[13] A. I. Berdyugin, S. G. Xu, F. M. D. Pellegrino, R. Krishna Kumar, A. Principi, I. Torre, M. Ben Shalom, T. Taniguchi, K. Watanabe, I. V. Grigorieva, M. Polini, A. K. Geim, and D. A. Bandurin, Science **364**, 162 (2019).

[14] Alex Levchenko, Songci Li, and A. V. Andreev, Phys. Rev. B **106**, L201306 (2022).

[15] L. W. Molenkamp, and M. J. M. de Jong Phys. Rev. B **49**, 5038 (1994).

[16] M. J. M. de Jong, and L. W. Molenkamp, Phys. Rev. B **51**, 13389 (1995).

[17] P. J. W. Moll, P. Kushwaha, N. Nandi, B. Schmidt, and A. P. Mackenzie, Science **351**, 1061 (2016).

[18] J. Gooth, F. Menges, N. Kumar, C. Shekhar, Y. Sun, U. Drechsler, R. Zierold, C. Felser, and B. Gotsmann, Nat. Commun **9**, 4093 (2018).

[19] G. M. Gusev, A. D. Levin, E. V. Levinson, and A. K. Bakarov, AIP Adv. **8**, 025318 (2018).

[20] A. D. Levin, G. M. Gusev, E. V. Levinson, Z. D. Kvon, and A. K. Bakarov, Phys. Rev. B **97**, 245308 (2018).

[21] G. M. Gusev, A. S. Jaroshevich, A. D. Levin, Z. D. Kvon, and A. K. Bakarov, Phys. Rev. B **103**, 075303 (2021).

[22] A. C. Keser, D. Q. Wang, O. Klochan, D. Y. H. Ho, O. A. Tkachenko, V. A. Tkachenko, D. Culcer, S. Adam, I. Farrer, D. A. Ritchie, O. P. Sushkov, and A. R. Hamilton, Phys. Rev. X **11**, 031030 (2021).

[23] L. Ella, A. Rozen, J. Birkbeck, M. Ben Shalom, D. Perello, J. Zultak, T. Taniguchi, K. Watanabe, A. K. Geim, S. Ilani, and J. A. Sulpizio, Nat. Nanotechnol. **14**, 480 (2019).

[24] J. A. Sulpizio, L. Ella, A. Rozen, J. Birkbeck, D. J. Perello, D. Dutta, M. Ben Shalom, T. Taniguchi, K. Watanabe, T. Holder, R. Queiroz, A. Principi, A. Stern, T. Scaffidi, A. K. Geim, and S. Ilani, Nature **576**, 75 (2019).

[25] C. Kumar, J. Birkbeck, J. A. Sulpizio, D. Perello, T. Taniguchi, K. Watanabe, O. Reuven, T. Scaffidi, A. Stern, A. K. Geim, and S. Ilani, Nature **609**, 276 (2022).

[26] A. Aharon-Steinberg, T. Völkl, A. Kaplan, A. K. Pariari, I. Roy, T. Holder, Y. Wolf, A. Y. Meltzer, Y. Myasoedov, M. E. Huber, B. Yan, G. Falkovich, L. S. Levitov, M. Hücker, and E. Zeldov, Nature **607**, 74 (2022).

[27] A. Shytov, J. F. Kong, G. Falkovich, and L. Levitov, Phys. Rev. Lett. **121**, 176805 (2018).

[28] A. Gupta, J. J. Heremans, G. Kataria, M. Chandra, S. Fallahi, G. C. Gardner, and M. J. Manfra, Phys. Rev. Lett. **126**, 076803 (2021).

[29] S. Vijayakrishnan, F. Poitevin, O. Yu, Z. Berkson-Korenberg, M. Petrescu, M. P. Lilly, T. Szkopek, K. Agarwal, K. W. West, L. N. Pfeiffer, and G. Gervais, Nat Commun **14**, 3906 (2023)

[30] W. E. Olmstead, Acta Mechanica **21**, 289 (1975).

[31] T. Kawamura, and Sankar Das Sarma, Phys. Rev. B **45**, 3612 (1992).

[32] Gabriele F. Giuliani, and John J. Quinn, Phys. Rev. B **26**, 4421 (1982).

[33] J. M. Ziman , *Electrons and Phonons* (Oxford University press, Clarendon, 1960).

[34] D. A. Kleinman, and A. L. Schawlow, J. Appl. Phys. **31**, 2176 (1960).

[35] E. J. Koop, M. J. Iqbal, F. Limbach, M. Boute, B. J. van Wees, D. Reuter, A. D. Wieck, B. J. Kooi, and C. H. van der Wal, Semicond. Sci. Technol. **28**, 025006 (2013).

[36] A. Mittal, R. G. Wheeler, M. W. Keller, D. E. Prober and R. N. Sacks, Surface Science **361**, 537 (1996) ; A. Mittal, Electron-phonon scattering rates in GaAs/AlGaAs 2DEGs below 0.5 K (Doctoral dissertation, Yale University 1996).

5

Discussion

5.1 Electron Transport Regime and Lengthscales

The results presented in the previous chapter thoroughly investigated hydrodynamic transport in ultra-high mobility 2DEGs. While the exceptional mobility of the material leads to a large momentum-relaxing mean free path ℓ_{MR} value below 1 K, it is essential to recognize that this alone does not guarantee the onset of hydrodynamic transport. Our study, detailed in Chapters 3 and 4, underscores the importance of device geometry, material quality, and a carefully selected temperature range where $e-e$ scattering dominates in observing hydrodynamic transport. We conducted measurements on two Corbino samples and two VdP samples. In the VdP samples, the bulk of the sample exhibited the expected monotonic increase in resistance with temperature, contrasting with the anomalous behaviour observed

in the Corbino samples Fig. 4 of Chapter 3. At temperatures below 2 K, VdP301 exhibited a constant resistance, while VdP302 maintained a constant resistance below 1 K. Above these temperature thresholds, an increase in resistance represents a transition to phonon-dominated diffusive transport. In contrast, the Corbino devices demonstrated non-monotonic behaviour, with CBM302 showing features indicative of the Gurzhi effect, suggesting collective electron flow.

5.1.1 Importance of Lengthscales

To understand the anomalous behaviour in Corbino devices, we analyzed the relevant lengthscales as a function of temperature. We compared them with the measured local resistance over the same temperature range, as shown in Fig. 5.1. We calculated the momentum-conserving mean free path, ℓ_{MC}, using the Fermi velocity v_F and the momentum-conserving scattering lifetime τ_{MC}, as

$$\ell_{MC} = v_F \tau_{MC}, \tag{5.1}$$

where τ_{MC} is obtained using the Giuliani and Quinn equation, which gives the scattering rate for momentum-conserving events [102] in a 2DEG. The equation for the scattering lifetime is given by

$$\frac{1}{\tau_{MC}} \approx \frac{(k_B T)^2}{2\pi\hbar E_F} \left[\log\left(\frac{E_F}{k_B T}\right) + \log\left(\frac{2q_{TF}}{k_F}\right) + 1 \right], \tag{5.2}$$

where E_F, k_F, q_{TF}, and k_B represent the Fermi energy, Fermi wave vector, Thomas-Fermi wave vector, and Boltzmann constant, respectively. The momentum-relaxing mean free path ℓ_{MR} was determined using the electron mobility (μ), with $\ell_{MR} = 5.22 \times \mu\sqrt{n}$, where n is the two-dimensional electron density. Since our study focuses on transport below 1 K, we neglected the role played by phonons and hence its effect on ℓ_{MR}, as their effect on ℓ_{MR} has been shown to be negligible in this temperature range [29].

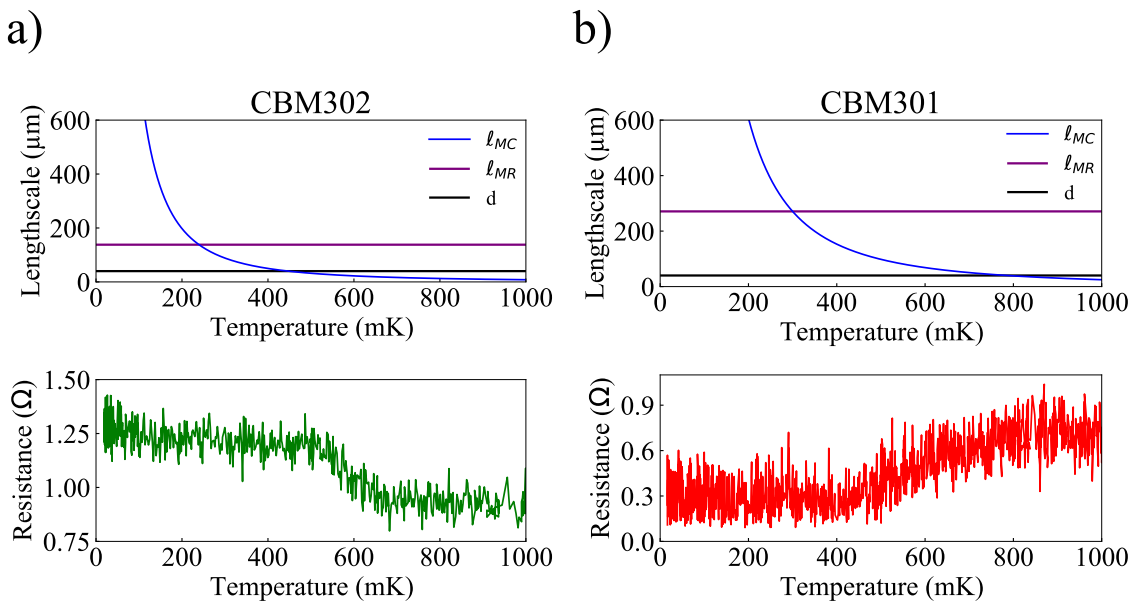

FIGURE 5.1 – Figure shows the temperature dependence of scattering lengthscales, channel width and resistance measured for the CBM302 (a) and CBM301 (b) samples. The top panels display the momentum-conserving mean free path ℓ_{MC}, momentum-relaxing mean free path ℓ_{MR}, and Corbino channel width d as functions of temperature. In the CBM302 sample (a), resistance remains constant below 500 mK, indicating ballistic transport, and decreases above 500 mK as ℓ_{MC} becomes the smallest length scale. In contrast, the CBM301 sample (b) exhibits ballistic transport from 20 mK to 400 mK, with resistance increasing as ℓ_{MC} shortens and approaches the channel width d around 800 mK.

The resistance of CBM302 is observed to remain constant below 500 mK, suggesting a ballistic transport, since the channel width, $d = 40$ μm, is much less than the ℓ_{MR} and ℓ_{MC} in that regime, see Fig. 5.1a. As the temperature increases beyond 500 mK, the resistance was observed to decrease, reaching a minimum when the condition $\ell_{MC} \ll W \ll \ell_{MR}$ was met. Between 500 mK and 1 K, where ℓ_{MC} becomes the smallest length scale, $e-e$ interactions dominate and allows for a continuum to form. In CBM301, ballistic transport was observed between 20 mK and 400 mK, where the Corbino channel width d was smaller than both ℓ_{MR} and ℓ_{MC} (see Fig. 5.1b). Consequently, the resistance remained constant in this temperature range. However, as the temperature was increased beyond 400 mK, ℓ_{MC} decreased rapidly, and becomes significantly shorter than ℓ_{MR}, eventually approaching the channel width d around 800 mK. In this temperature range (400 mK to

800 mK), the resistance of CBM301 increased and was then followed by a saturation over a broad temperature range above 1 K (see Fig. B.8).

5.1.2 Electron Flow in Nonlocal Configuration

The local transport measurements discussed in terms of lengthscales laid the foundation for understanding different electron transport regimes that occur in our ultra-high mobility samples and indicate the Gurzhi effect in CBM302. In Chapter 4, Fig. 2 presents a comparison of both local and nonlocal measurements conducted on CBM301 and CBM302. In the nonlocal configuration, the voltage difference ΔV_{NL} was measured 40 μm away from the current path. Previous studies conducted by other research groups reported negative nonlocal resistance [61], which was shown to be a signature of hydrodynamic transport in Hall bar and vicinity devices. In these cases, the negative nonlocal resistance was attributed to the formation of current whirlpools [61]. However, the nonlocal response observed in our experiments is not likely resulting from current backflow. By comparing our data with a simulation of the Navier-Stokes (NS) equation in a purely radial geometry, we arrived at the conclusion that the nonlocal response in our devices arises from the viscous flow of electrons and its associated drag effects. Previous studies have shown that in hydrodynamic momentum-mode transport, there is momentum flow towards the current source [100]. Viscosity prevents any radial shear deformations, where layers of fluid move at different velocities along the flow direction. These shear deformations result from radial velocity gradients, such as those observed in the discontinuous motion at contact boundaries in Ohmic transport, leading to flow spreading beyond the discontinuity [18].

Compared to experimental data, the numerical simulations based on the NS equation further elucidate the differences in transport between CBM301 and CBM302 (see Fig. 3 in Chapter 4). For CBM301, both simulations and measurements show agreement below 400 mK, with a zero nonlocal signal indicating the absence of hydrodynamic transport in this regime. However, above 400 mK, simulations based

purely on hydrodynamic models begin to diverge from experimental data. This discrepancy, alongside a small but noticeable increase in the nonlocal signal in CBM301, suggests that the increase in local resistance might not be a manifestation of hydrodynamic transport. Importantly, this increase in nonlocal signal coincides with a simultaneous rise in local resistance, as shown in Chapter 4, Fig. 2 and this warrants further studies. Based solely on the NS equation, our simulations did not fully capture the nonzero nonlocal potential observed below 450 mK in CBM302, as they did not account for ballistic transport. Above 450 mK, we observed an increase in the negative nonlocal signal, which notably coincides with the temperature at where a decrease in local resistance occurs in CBM302. Nonetheless, the qualitative agreement between the numerical simulations and experimental nonlocal measurements in the temperature range of 450 mK to 1 K strengthens our conclusion that CBM302 exhibits hydrodynamic transport.

5.1.3 Investigation of the Increase in Resistance in CBM301

Although we could not definitively explain the increase in resistance observed in CBM301 above 400 mK for both local and nonlocal measurements, we were able to rule out several potential causes, and these are discussed below.

Superconductivity: One of the referees of our manuscript published in Nature Communications raised the question of whether there could be a possible effect due to superconductivity in the contacts. Previous reports from other research groups suggest that contacts formed with specific Ge/Au/Ni/Au layers compositions can exhibit a superconducting effect [103,104], although achieving this requires a precise tuning of the layer thickness and composition. However, as detailed in Appendix B, our magnetotransport measurements did not show any anomaly near the expected critical field of 0.15 T. Additionally, differential resistance ($\frac{dV}{dI}$) measurements under a DC bias confirmed ohmic behaviour (see Fig. 5.2) at $T \approx 6$ mK, further suggesting that superconductivity is not responsible for the observed increase in resistance.

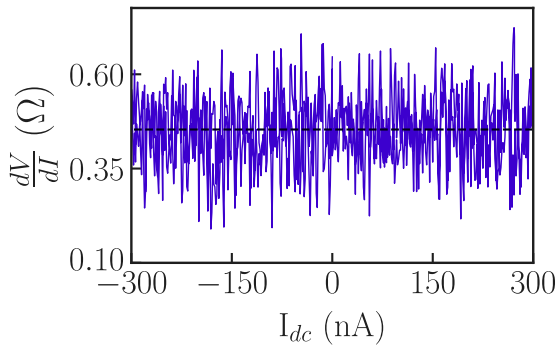

FIGURE 5.2 – The figure shows differential resistance ($\frac{dV}{dI}$) measurement for the CBM301 sample with a 300 nA DC bias. The data exhibit a linear response with no noticeable deviation from Ohmic behaviour. This result confirms that the increased resistance observed above 400mK is not due to superconductivity.

Residual Trapped Magnetic Field: Magnetotransport measurements were conducted carefully near zero magnetic fields to eliminate the influence of any residual trapped magnetic fields in the superconducting magnet as ultra-high mobility 2DEG Corbino samples are highly sensitive, even to small magnetic fields of a few gausses. To account for any effects caused by trapped magnetic flux, we applied a

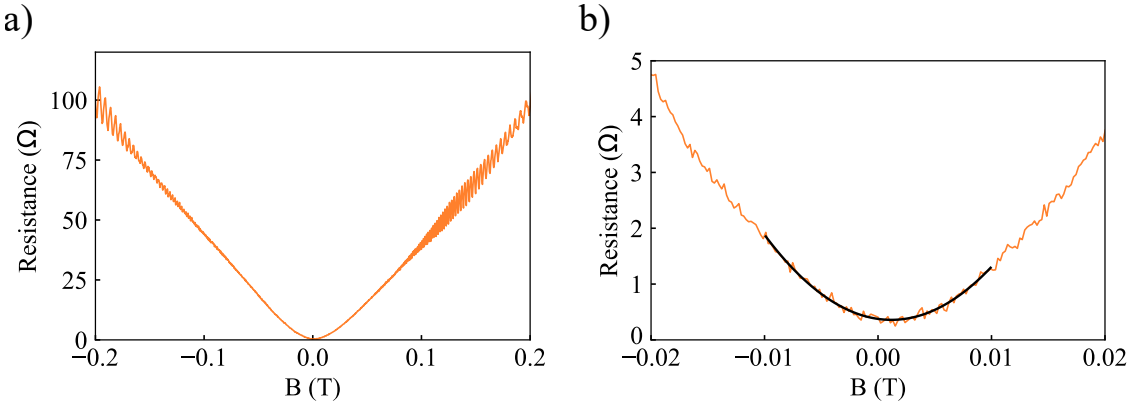

FIGURE 5.3 – Panel (a) shows resistance as a function of magnetic field for CBM301 near $B = 0$ T, showcasing the ultra-high mobility 2DEG Corbino sample's extreme sensitivity to even small magnetic fields. (b) A zoomed-in plot of the resistance (red line) with a least-squares fit (black line) using the equation $R = a \times (B - B_0)^2 + c$, where the parameters a and c can be used to extract mobility and contact resistance as explained in reference [45], and B_0 captures any offset of the true zero magnetic field. The fit confirms that B_0, with a value of 0.00117 ± 0.00081 T, is small but non-zero, indicating the presence of a small residual magnetic field, $\lesssim 12$ gauss.

parabolic fit to the data measured near zero fields, following the procedure outlined in reference [45], and determined the exact zero-field values (see Fig. 5.3). All subsequent measurements were performed after applying this zero-field correction.

Thermal Disequilibrium: To further investigate whether the observed increase could have resulted from electrons being out of thermal equilibrium with the mixing chamber temperature, we measured the resistance at specific discrete temperatures. The results of these discrete measurements aligned with the continuous data presented in this thesis (see Fig. 5.4), leading us to conclude that thermal disequilibrium did not contribute to the resistance increase observed in CBM301.

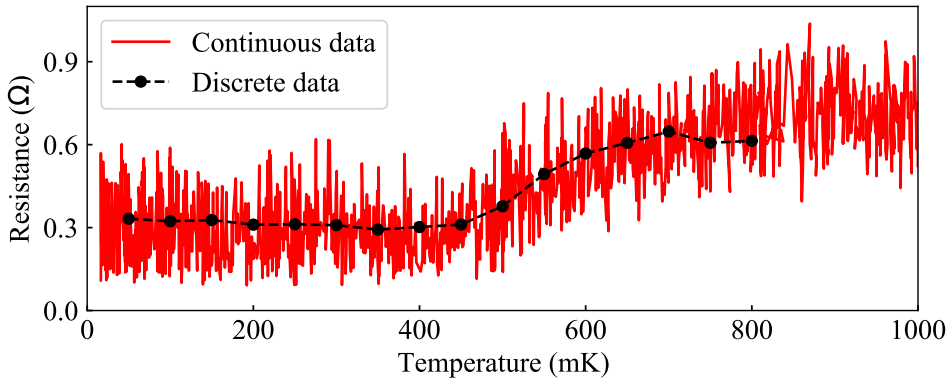

FIGURE 5.4 – Discrete and continuous resistance measured as a function of temperature for CBM301. The discrete data represent averaged values of time traces taken at specific temperatures. The discrete data points align well with the continuous measurements, confirming that the observed increase in resistance is not due to thermal disequilibrium between the electrons and the mixing chamber.

Probe Symmetry: We conducted probe symmetry measurements to determine whether the increase in resistance could be due to contact deformation or due to charge accumulation in the contact. To check this, we conducted electron transport measurements in different probe configurations. Since the probe symmetry was respected in all cases, as shown in Appendix C, we conclude that charge accumulation is not the cause for the observed resistance increase in CBM301.

Given our laboratory's expertise in low-temperature and high magnetic fields, we are naturally inclined to investigate the electronic transport properties, but in order to understand this further, one could also think of conducting imaging experiments in these devices. To summarize, despite our efforts to understand it, the origin of the resistance increase above 400 mK in CBM301 remains an unresolved mystery, suggesting that other physical factors are at play and warrant further investigation.

5.2 Electron Transport at Higher Temperatures

Thus far, our focus has been on transport measurements below 1 K, where phonon effects are negligible [29]. However, local electron transport measurements were also extended up to 100 K, and the corresponding results are presented in Fig.B.8. At these higher temperatures, both CBM301 and CBM302 exhibit the expected monotonic increase in resistance. In the case of CBM301, the resistance remained relatively constant over a broad temperature range up to 10 K. This is likely due to an interplay between diffusive and hydrodynamic transport, which is followed by an increase in resistance due to phonon-dominated electron transport at higher temperatures above 10 K (see Fig.B.8). In contrast, CBM302 displays electron transport characteristics closely aligned with Gurzhi's predictions and indicates a transition from ballistic to hydrodynamic transport followed by diffusive transport as phonon scattering eventually becomes increasingly dominant at higher temperatures.

For nonlocal transport, where the observed effect is purely due to the viscous drag of electrons, the higher-temperature resistance measurements is shown in Fig. 5.5. This data suggests an enhanced viscous effect in CBM302 extending from 500 mK to 90 K. At these elevated temperatures, phonon scattering becomes dominant and significantly influences mobility. Our findings suggest that hydrodynamic transport can occur over a wide temperature range due to increased $e-e$ interactions. At densities below $2 \times 10^{11}\mathrm{cm}^{-2}$, it has been shown theoretically [105] that as temperature increases, the screening of electrons diminishes, which leads to

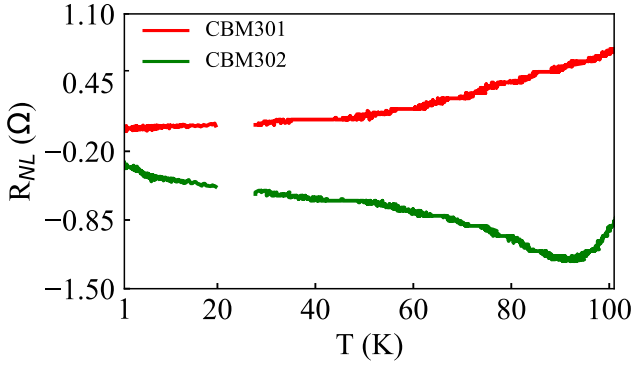

FIGURE 5.5 – The figure shows the nonlocal resistance across a broad temperature range for CBM301 and CBM302 from 1 K to 100 K. For CBM302 (green), the negative nonlocal resistance shows a notable increase from 500 mK (see Fig. 3 for resistance below 1 K) to 90 K, suggesting enhanced viscous flow. In contrast, the nonlocal resistance of CBM301 (red) remains relatively constant with a rise above 50 K.

stronger $e-e$ interactions. This reduction in screening allows hydrodynamic electron transport to persist even in the presence of phonon scattering. However, the absence of hydrodynamic transport in the higher electron density sample CBM301 could be attributed to other factors.

5.3 Towards Hall Viscosity

The findings from Chapters 3 and 4 demonstrate that hydrodynamic electron transport in ultra-high mobility 2DEGs. Looking forward, a particularly promising new avenue of research is the exploration of Hall viscosity, a fundamental property that emerges when time-reversal symmetry is broken in two-dimensional systems. The time-reversal symmetry breaking can be achieved in 2DEGs by applying a magnetic field. In the following two subsections, we provide a mathematical description of the Hall viscosity and details on how it could be probed in the Corbino geometry.

5.3.1 Mathematical Description of Odd Viscosity

The study of viscosity involves understanding the stress tensor, which can be broken down into symmetric and anti-symmetric parts and is expressed as

$$\frac{\partial u_i}{\partial x_j} = \frac{1}{2}\left(\frac{\partial u_i}{\partial x_j} + \frac{\partial u_j}{\partial x_i}\right) + \frac{1}{2}\left(\frac{\partial u_i}{\partial x_j} - \frac{\partial u_j}{\partial x_i}\right), \tag{5.3}$$

where u_i and u_j are the components of the velocity vector in different spatial directions. The first term is the symmetric strain rate tensor, and the second is the anti-symmetric vorticity tensor. The symmetric part is related to deformation, whereas the anti-symmetric part is related to rotation. In a homogeneous Newtonian fluid [1], the relationship between viscous stress σ_{ij} and strain rate $\frac{\partial u_k}{\partial x_l}$ is linear, described by a fourth-order viscosity tensor η_{ijkl} given by

$$\sigma_{ij} = \eta_{ijkl}\frac{\partial u_k}{\partial x_l}. \tag{5.4}$$

For most fluids, including air and water, the viscosity tensor η_{ijkl} is symmetric [106] *i.e.,*

$$\eta_{ijkl} = \eta_{jikl} = \eta_{ijlk}. \tag{5.5}$$

However, two-dimensional systems offer an important distinction. In this case, the viscosity tensor can be decomposed into symmetric $\eta^{(s)}$ and anti-symmetric $\eta^{(a)}$ parts,

$$\eta_{ijkl} = \eta^{(s)}_{ijkl} + \eta^{(a)}_{ijkl}, \tag{5.6}$$

where the symmetric part $\eta^{(s)}_{ijkl}$ corresponds to even viscosity and the anti-symmetric part $\eta^{(a)}_{ijkl}$ is odd viscosity. Odd viscosity has been shown to arise only when time-reversal symmetry is broken [106]. In a 2DEG, this can be achieved when a magnetic field B is applied perpendicular to it so that the Lorentz force compels the electrons

1. A Newtonian fluid follows Newton's law of viscosity, where shear stress is directly proportional to the velocity gradient, and the viscosity remains constant regardless of the applied force. Examples include water, petrol, and milk.

to move in a circular path. Reversing time hence changes the direction of the Lorentz force's velocity component, causing the electrons to move in the opposite direction, thereby breaking time-reversal symmetry. Hence, the flow can be mathematically represented as a modified version of Eq. 2.25 in a magnetic field applied in the z-direction given by

$$\frac{\partial \vec{u}}{\partial t} = \nu_{xx}\nabla^2\vec{u} - \frac{\vec{u}}{\tau_{MR}} + \frac{e\vec{E} + \vec{u} \times B}{m} + \nu_{xy}\nabla^2 \times \hat{z}, \tag{5.7}$$

where $\vec{u}$ is the electron drift velocity, ν_{xx} here denotes the kinematic viscosity, $\vec{E}$ is the electric field, τ_{MR} is the momentum relaxing scattering time and ν_{xy} is the Hall viscosity. Here, the term $\nu_{xy}\nabla^2 \times \hat{z}$ accounts for the viscous force acting perpendicular to the flow direction, incorporating the effects of Hall viscosity. To understand it, we can envision a solid disc rotating in a fluid, and the viscosity will act as a torque opposing the motion, whereas the Hall viscosity will act as a pressure applied to the disc. Therefore, the kinematic viscosity can be probed by examining ρ_{xx}, while the Hall viscosity can be investigated through ρ_{xy}. Observation of classical Hall viscosity has been reported in graphene [82,89]. However, the experimental observation of Hall viscosity at higher magnetic fields is still lacking [107].

5.3.2 Probing Hall Viscosity in the Corbino Geometry

The Corbino geometry has been extensively used to study viscous electron transport [66, 83, 108–111] and is favoured by many theorists because of its symmetric geometry, which minimizes correction terms related to the geometry. It has been proposed by A. Stern *et al.* that the Hall viscosity can be measured directly by probing the Hall current j_ϕ *i.e.,* current in the azimuthal direction, as long as the sample remains in the hydrodynamic regime [83]. As noted by them, an essential requirement for probing Hall viscosity in a Corbino geometry is the application of a non-quantizing magnetic field B. This ensures that the Fermi surface remains intact, allowing for the application of a straightforward definition of Hall viscosity, as

outlined in the reference [83]. In the presence of a perpendicular magnetic field, the current densities in a Corbino geometry consist of both radial (j_r) and azimuthal (j_ϕ) components, with the azimuthal current j_ϕ varying as a function of the radial position r due to the circular symmetry (see Fig. 5.6).

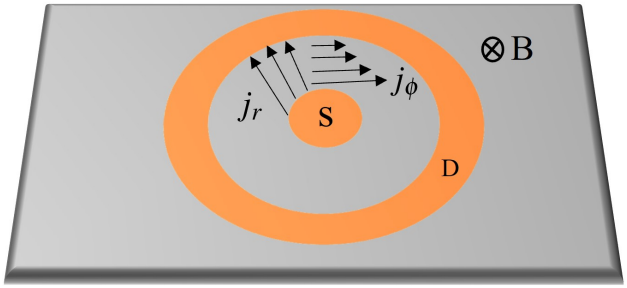

FIGURE 5.6 – The figure shows a schematic representation of the current components in a Corbino disk under a magnetic field B. It illustrates the radial j_r and azimuthal j_ϕ components of the current densities.

In this case, two additional length scales become relevant alongside the mean free paths ℓ_{MC} and ℓ_{MR}. The first is the cyclotron radius r_c, which is defined as

$$r_c = \frac{\hbar k_F}{eB}, \tag{5.8}$$

where $\hbar$ is the reduced Planck's constant, k_F is the Fermi wavevector, e is the electron charge, and B is the magnetic field strength. The second is the Gurzhi length ℓ_c given by

$$\ell_c = r_c \sqrt{\frac{\ell \ell_{MR}}{4\ell^2 + r_c^2}}, \tag{5.9}$$

where ℓ is the effective length defined as $\ell = \left(\ell_{MR}^{-1} + \ell_{MC}^{-1}\right)^{-1}$. When the Gurzhi length significantly exceeds the radial size of the Corbino ring ($l_c \gg L$), the system is considered to be in the hydrodynamic regime. In this limit, A. Stern and coworkers [83] introduced a parameter known as viscous angle θ_{vis} and showed that it is related to the Hall angle by

$$\tan\theta_H = \frac{j_\varphi}{j_r} = \frac{\nu_{xy}}{\nu_{xx}} = \tan\theta_{\text{vis}}. \tag{5.10}$$

Therefore, the confirmation of the hydrodynamic electron transport demonstrated in this thesis lays the groundwork for future investigations of the classical Hall viscosity. Extending measurements to non-quantizing magnetic fields will enable further exploration of this phenomenon, potentially leading to new insights into the hydrodynamics of two-dimensional systems. For simplicity, we have used a single-ring Corbino in this section, however, the four-terminal geometry developed in the Gervais Lab will allow us to probe the 2DEG without any contact contribution and hence it enables us to probe the Hall viscosity in different Onsager configurations. In the future this will allow us to determine whether hydrodynamic reciprocity is satisfied when the time-reversal symmetry is broken.

6

Conclusion

6.1 Evidence for Hydrodynamic Transport in Ultra-High Mobility 2DEGs

Over the past five decades, advancements in the mobility of these heterostructures [25–36] have been an inevitable factor in studying various quantum phenomena. The ultra-high electron mobility of the material, characterized by a large momentum-relaxing mean free path (ℓ_{MR}), provides an extended range of temperatures and device scales for exploring non-diffusive transport regimes such as ballistic and hydrodynamic. Chapters 3 and 4 presented local and nonlocal electronic transport measurements performed on four terminal Corbino samples fabricated on ultra-high mobility heterostructures with distinct electron densities. In Chapter 3, we compared the local transport results in Corbino samples with measurements

conducted on large millimetre-sized VdP samples. The VdP samples showed monotonic behaviour, with a clear transition to a phonon-dominated diffusive transport at temperatures above 1 K for VdP302 and 2 K for VdP301. In contrast, the local electron transport measurements in Corbino devices displayed non-monotonic behaviour. The lower electron density sample, CBM302, showed a temperature dependence for the resistance that resembles Gurzhi's prediction. It showed ballistic transport at lower temperatures and transition to hydrodynamic flow in the vicinity of 500 mK followed by phonon-dominated diffusive transport at temperatures above 3 K. In the higher electron density sample (CBM301), however, no clear signature of hydrodynamic transport was observed. Instead, an unexpected increase in resistance occurred around 400 mK. Despite exploring several potential avenues of explanation, the cause of this resistance increase remains uncertain and warrants further investigation. Finally, nonlocal measurements further confirmed viscous electron flow in CBM302, and numerical simulations of the Navier-Stokes equation performed by Zachary Berkson-Korenberg, a member of the Gervais Lab, support our conclusion of hydrodynamic electron transport in CBM302.

The findings presented in this thesis have important implications for low temperature condensed matter physics, particularly in the study of electron transport in ultra-high mobility systems. The results presented in this thesis are highly reproducible, having been consistently observed across multiple cooldowns and in two different refrigerators with different wiring. Our observation of hydrodynamic electron flow in GaAs/AlGaAs Corbino devices provides critical insights into non-diffusive transport regimes, reshaping the understanding of viscous transport in electron fluids. While the origin of the unexpected resistance increase in the higher electron density sample remains unresolved, this phenomenon opens up intriguing questions about electron interactions at low temperatures. Further exploration is essential to unravel this mystery. In the following section, we propose future research directions that can significantly advance our understanding of electron hydrodynamics, sparking anticipation and excitement for the next steps in this field of research.

6.2 Future Work

This thesis provides strong evidence for hydrodynamic transport in ultra-high mobility 2DEGs. The results presented in Chapters 3 and 4 suggest several promising directions and some of them are listed below.

1. As discussed in Chapter 5, extending this study with a non-quantizing magnetic field will enable experimental measurements of Hall viscosity. The symmetric design of the Corbino geometry provides a unique opportunity to probe Hall viscosity as a function of the Hall angle. Extending this study to higher magnetic fields will enable the exploration of viscous effects in quantum Hall states, which as of today remains experimentally unexplored [107].
2. The Gervais Lab currently has access to heterostructures with electron mobility as high as $\sim 50 \times 10^6$ cm^2(Vs)$^{-1}$ grown by Dr. Loren Pfeiffer at Princeton University. This high electron mobility, combined with implementing a gate to tune device density, will offer more definitive insights into the physics of electron viscous flow in the Corbino geometry.
3. The anomalous behaviour observed in CBM301 could not be definitively resolved despite ruling out several possibilities. Notably, measurements conducted in a single-ring Corbino device with a larger channel width of 750 μm, fabricated on the same ultra-high mobility wafer as CBM301 (see Appendix A), also indicated an increase in resistance around 400 mK. To gain further insights into this phenomenon, implementing imaging techniques that would not interfere with the flow itself could prove beneficial in understanding the anomalous behaviour observed in CBM301. One can either detect spatial variations in electric potential or measure the local magnetic field generated by the movement of charges to visualise electron flow [99].

6.3 Final Words

The discovery of hydrodynamic electron transport in ultra-high mobility 2DEG Corbino rings presented in this thesis, is a pivotal advancement in our understanding of electron transport. This discovery brings the rich theoretical framework of electron hydrodynamic transport to light. In recent years, interest in hydrodynamic electron flow has surged, and in this thesis, we report electron transport characteristics that was predicted by Gurzhi roughly sixty years ago. The key finding of our research is the significant impact of $e-e$ interactions on viscosity, even in a radially constrained geometry. While certain phenomena, such as the resistance increase in CBM301 remain unresolved, they spark curiosity and they set the stage for future investigations. These results also advance the study of viscous electron transport and highlight the broader significance of hydrodynamic transport in electronic devices, hence reshaping the landscape of condensed matter physics.

A

Fabrication details of Corbino devices and Transport in Single Ring Corbino

A.1 Corbino Geometry

The Corbino devices presented in this thesis were formed on GaAs/AlGaAs heterostructures grown by molecular beam epitaxy (MBE). We fabricated two single-ring and two multi-ring Corbino samples. While the main text of the thesis focuses on the results from the multi-ring samples, the initial measurements were conducted on single-ring Corbino samples. The single-ring samples have an inner contact radius of $r_1 = 0.25$ mm, an outer contact inner radius of $r_2 = 1.0$ mm, and an outer

contact outer radius of $r_3 = 1.5$ mm. Detailed fabrication procedures are provided in the following section. The fabrication of samples CB01, CB05, and CBM301 were carried out by Simon Bilodeau and Keyan Bennaceur, respectively. The wafers used for fabricating CBM301, CBM302, and CB05 were from Princeton, while the wafer for CB01 was obtained from Sandia National Laboratories. A table detailing the wafer specifications is provided below.

Name	Wafer Name	Geometry	Carrier Density (cm^{-2})	Mobility ($cm^2/V.s$)
CB01	VA142	Single ring	4.6×10^{11}	1×10^{6}
CB05	3.11.10.2	Single ring	3.6×10^{11}	2.7×10^{7}
CBM301	3.11.10.2	Multi-ring	3.6×10^{11}	2.7×10^{7}
CBM302	2.22.10.2	Multi-ring	1.69×10^{11}	2.04×10^{7}

TABLE A.1 – List of Corbino samples used for this project.

A.1.1 Fabrication Methods of Corbino

After cleaving and cleaning, the fabrication procedure begins with the application of resist using spin coating. We have used LOR5A and S1813 as resists. The wafer is first coated with one drop of LOR5A at a temperature of 180 °C for 1 minute and 30 seconds on a spin coat at 3500 rpm (V = 25.5). Subsequently, a drop of S1813 is applied, and the sample is annealed at 115 °C for 1 minute. We use a maskless UV lithography (SF100) technique with an exposure time of 4 minutes. After exposure, the resist is removed from the exposed areas using Microposit MF 319 Developer. The next step involves e-beam deposition, where layers of Ge/Au/-Ni/Au are deposited in 26/54/14/100 nm thicknesses, respectively, at a rate of 1-2 Å/s. Finally, annealing is carried out in an Ar atmosphere by ramping the temperature to 370 °C at a rate of 10 °C/sec, holding at 370 °C for 20 seconds, then further ramping to 440 °C at the same rate and maintaining this temperature for 80 seconds before cooling down.

A.2 Transport Measurements in CB01 and CB05

The two contacts formed in the CB01 and CB05 allow us to perform two-point measurements. At zero field, the resistance of the sample is much lower than that of the wiring and contact resistance. To prevent any inaccuracy associated with this, we attached two wires to each contact, which allowed us to perform a pseudo four-point measurement. The magnetotransport measurements conducted on CB05 and CB01 are shown in A.1.

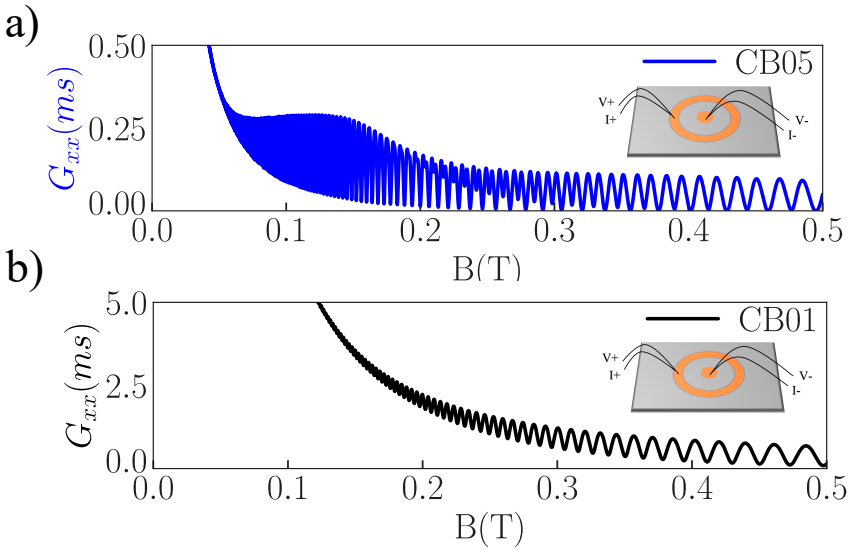

FIGURE A.1 – The figure shows the magnetotransport measurement conducted on CB05 (panel a) and CB01 (panel b) using pseudo four-point configuration. The well-defined SdH oscillations of CB05, even at a smaller field compared to CB01, indicate the higher quality of the sample.

Figure A.2 presents the transport measurements for these devices. Both samples show a non-monotonic behaviour. The interaction parameter values are 0.92 for CB05 and 0.81 for CB01. In CB05, the resistance decreases immediately as we increase the temperature from the base value of 20 mK, reaches a minimum, and then rises again, approaching its initial value. For the higher-density sample, CB01, the resistance decreases slightly and then starts to increase around 350 mK. Although we successfully eliminated the lead resistance, contact resistance and its effects per-

sisted in the measurements, which led us to fabricate four-terminal devices.

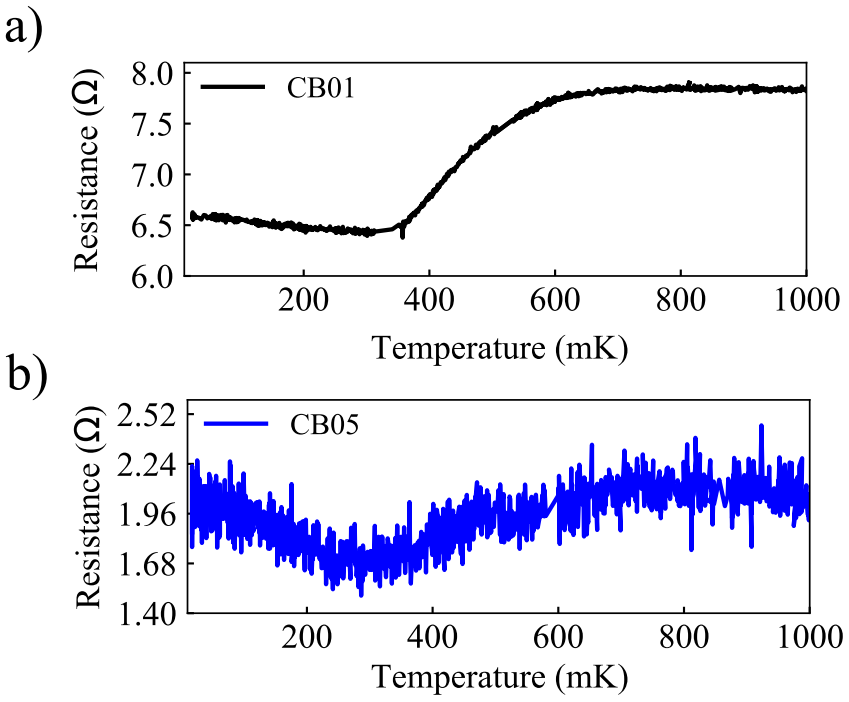

FIGURE A.2 – Transport measurements conducted at zero magnetic field (B = 0 T) on (a) CB01 and (b) CB05. Both devices exhibited a non-monotonic behaviour below 1 K. CB05 showed a decrease in resistance, reaching a minimum at $\sim$ 300 mK before increasing again. While CB01 shows a similar trend, with the resistance starting to increase around 370 mK.

B

Supplementary Material : Anomalous Electronic Transport in High-Mobility Corbino Rings

B.1 Heterostructure

A sketch of the wafer heterostructure used to fabricate CBM301, VdP301 and CBM302, VdP302 is shown in Fig.B.1. The main components forming the heterostructure grown on an undoped GaAs subtrate are : a buffer/spacer, the setback defining the position of the dopants, the quantum well width, and the spacer/capping layer. The main differences between the 301 and 302 heterostructures are : the electron density ($3.6 \times 10^{11}\ cm^{-2}$ for CBM301 and $1.7 \times 10^{11}\ cm^{-2-}$for CBM302) ;

the quantum well width (30 nm for CBM301 and 40 nm for CBM302) ; the setback distance for the dopants (∼80 nm for CBM301 and ∼160 nm for CBM302).

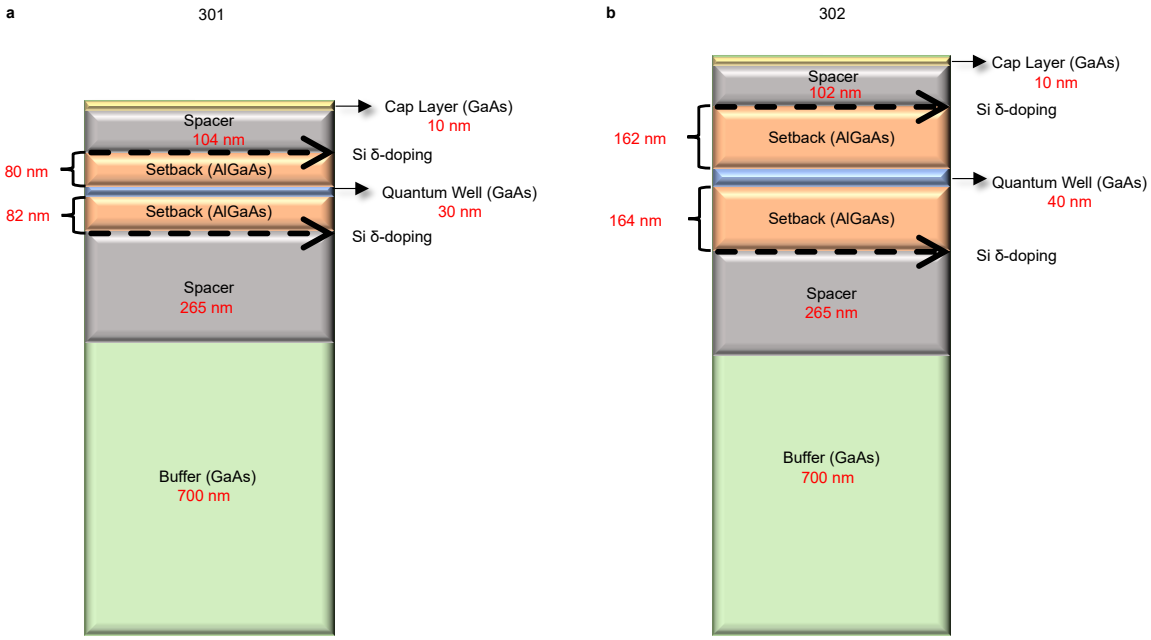

FIGURE B.1 – Heterostructure of (a) 301 (CBM301, VdP301) and (b) 302 (CBM302, VdP302). The main heterostructure components and their thickness are shown.

B.2 Electronic Transport Measurement Circuit

In the main text of the manuscript, Fig.2 shows the conductance of Corbino devices measured with two different electrical setups, and these are discussed below.

B.2.1 Experimental Setup A

The experimental setup A shown in Fig.B.2 consists of a SR830 lock-in amplifier and a resistor with a high resistance. An output voltage of 200 mV is passed through a 10 $M\Omega$ resistor connected in series with the Corbino device. This configuration allows us to apply a constant current of 20 nA to the outermost contact of the Corbino while keeping the inner contact grounded. The four-point resistance is calculated from the voltage drop measured across the inner two rings of the Corbino

samples.

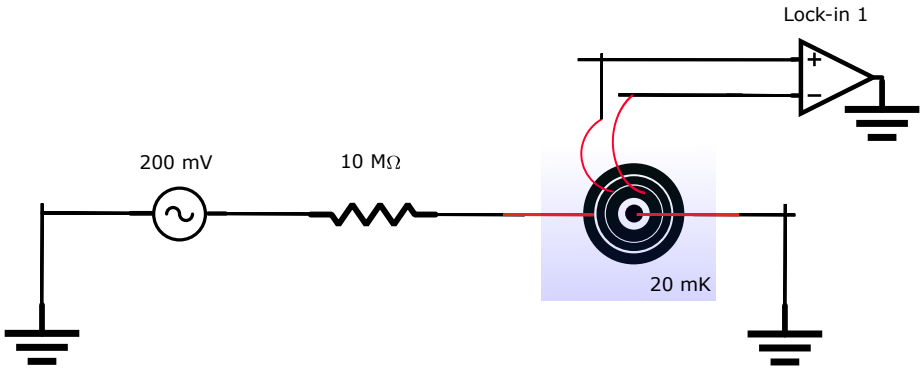

FIGURE B.2 – Setup A circuit used to determine the four point resistance of the Corbino sample with a fixed current of 20 nA.

B.2.2 Experimental Setup B

In the Corbino geometry, the sample has a large magneto-resistance in magnetic fields above $\sim$1 T, and as a result this makes the previous experimental circuit measurement not ideal. Experimental setup B was used to measure the conductance while sweeping the magnetic field in order to extract the electron density from the Shubnikov de-Haas (SdH) oscillations. In this configuration, an output voltage of 100 mV was applied to a voltage divider consisting of 100 $k\Omega$ $\parallel$ 100 Ω, connected in series with the Corbino. The current through the sample is calculated from the measured voltage drop across a 1 $k\Omega$ resistor connected in series with the Corbino. For both experimental setups A and B, a voltage pre-amp with the gain of 100 was used at the output end.

B.3 Magneto-transport Measurement

In Fig.B.4 the magneto-conductance measured at low perpendicular magnetic fields with the experimental setup B and is shown. The onset of Shubnikov-de Haas oscillations (SdH) is observed at very low magnetic fields as expected from the very high electron mobility of the 2DEGs. Due to a large magneto-conductance at low magnetic field in a Corbino sample, distinct panels show the conductance

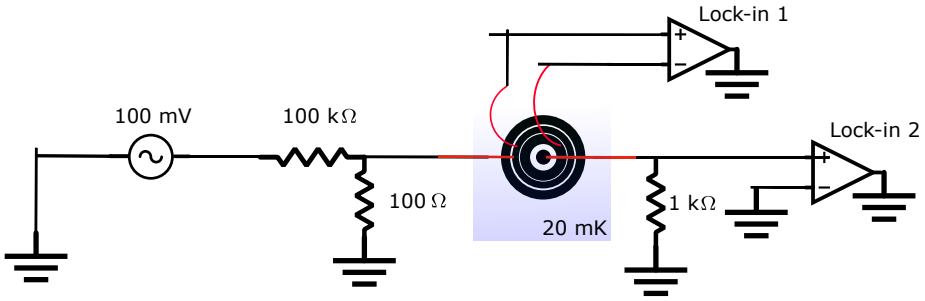

FIGURE B.3 – The circuit used to measure the conductance at B$\neq$ 0. This circuit was used in Fig.2 of the main manuscript to compare and verify the result obtained with setup A.

over different magnetic field ranges. No evidence was found for a superconducting transition, *i.e* a superconducting critical field, in either samples.

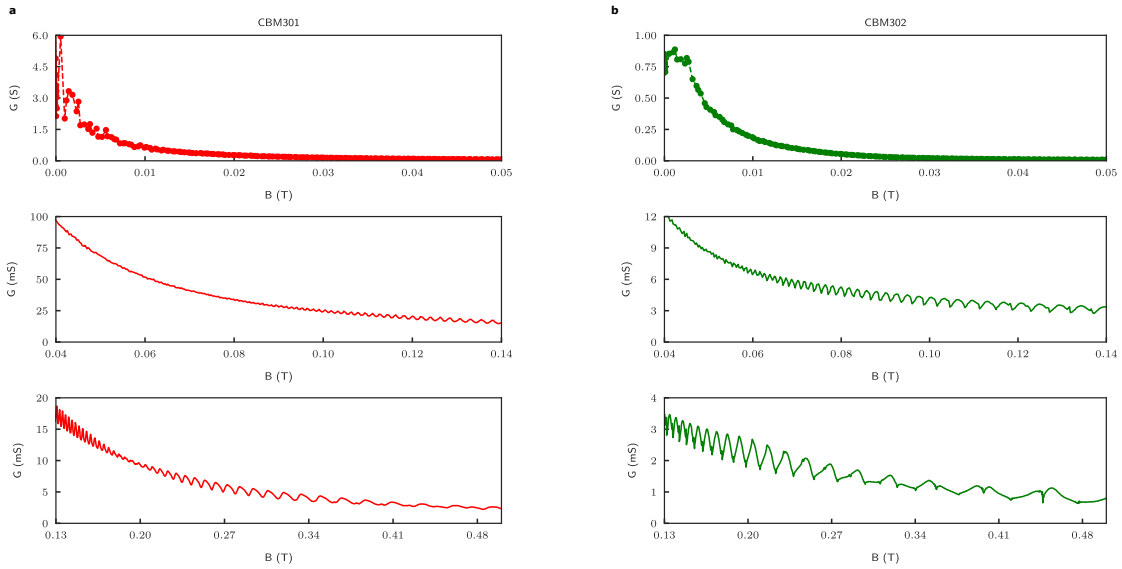

FIGURE B.4 – Magneto-conductance measured in (a) CBM301 and (b) CBM302 at 20 mK.

B.4 Electron Density Extraction

The SdH oscillations (after reducing the background) of conductivity (or conductance) *versus* inverse magnetic field are given by,

$$\Delta\sigma_{xx} \propto A \cos\left(2\pi\left(\frac{B_f}{B} - \delta\right)\right), \tag{B.1}$$

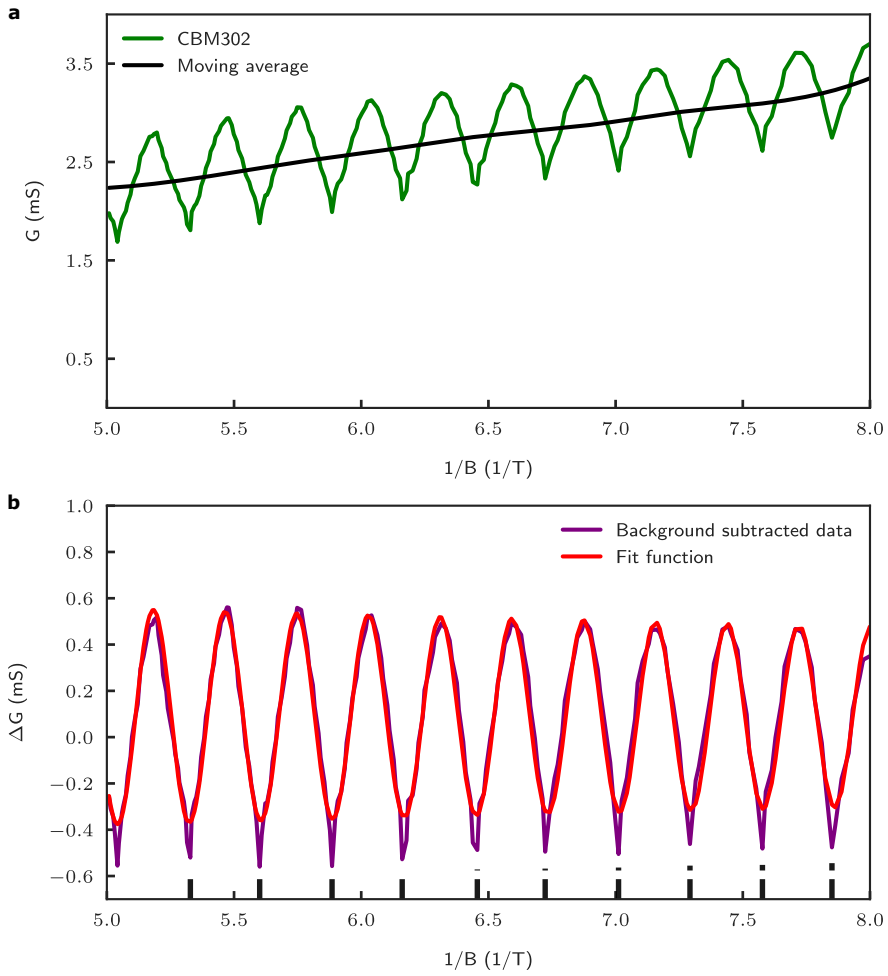

FIGURE B.5 – Panel (a) shows the SdH oscillation of CBM302 at 20 mK and the calculated moving average. The background reduced data and fit performed are shown in panel (b).

where the $\delta = 1/2$ and B_f is the SdH frequency. Here, we use the conductivity and conductance terms interchangeably since both parameters are related via a simple geometric factor. Fig.C.5 shows the background reduced SdH data and the fit performed for CBM302 at 20 mK. In it, we used the moving average of the raw data which was then subtracted to obtain the background reduced SdH oscillations. The fitting function used Eq B.1 to obtain the SdH frequency which was then used to calculate the electron density n,

$$n = \frac{2eB_f}{h}, \tag{B.2}$$

where e and h are the electron charge and Planck's constant.

B.4.1 Temperature Dependence of Electron Density

The electron density extracted using the aforementioned procedure at different temperatures ranging from 20 mK to 750 mK for CBM301 and CBM302 are shown in Fig.B.6. The calculated electron density remains constant within 0.5% in the temperature interval where the anomalous behaviour in electronic transport was observed.

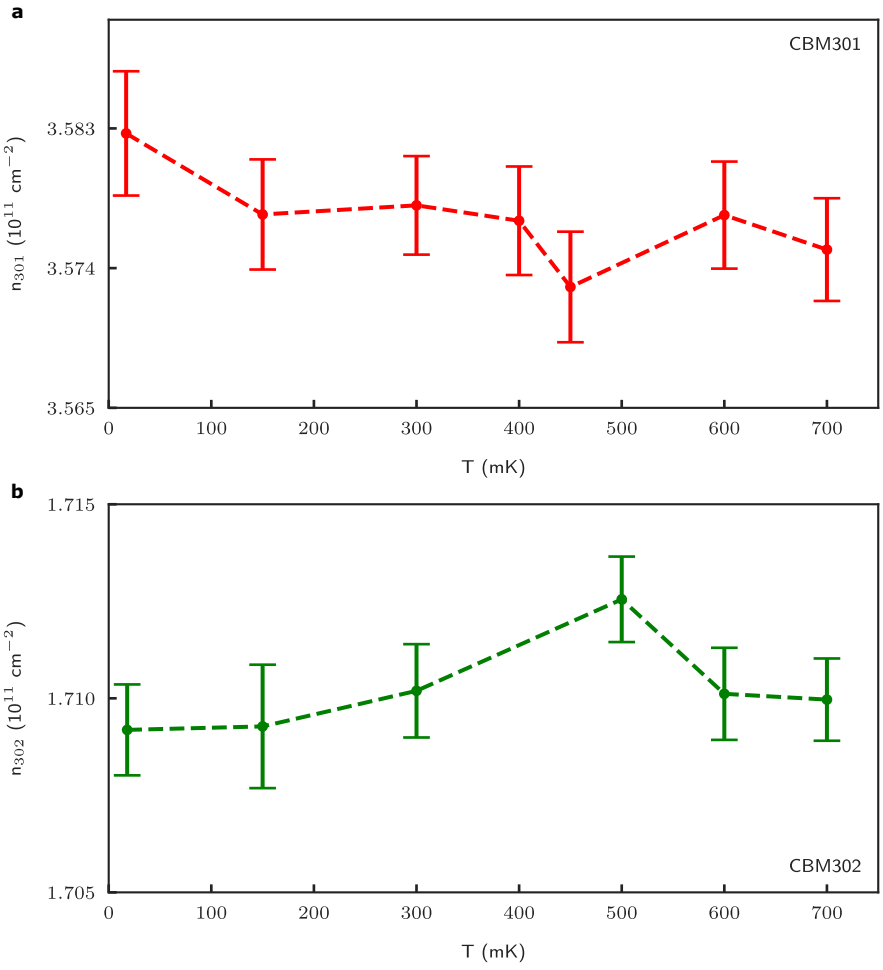

FIGURE B.6 – Temperature dependence of electron density for (a) CBM301 and (b) CBM302.

B.5 Data Consistency and Reproducibility

The anomalous behavior in resistance observed in CBM301 and CBM302 has been reproduced during several cooldowns. Fig.B.7 shows the data obtained for two different cooldowns in the same dilution refrigerator system using experimental setup A for both Corbino samples. In addition to the data shown in Fig.B.7, the results have been reproduced several times using both experimental setups in different cooldowns, and also in two different dilution refrigerators with distinctive electronics.

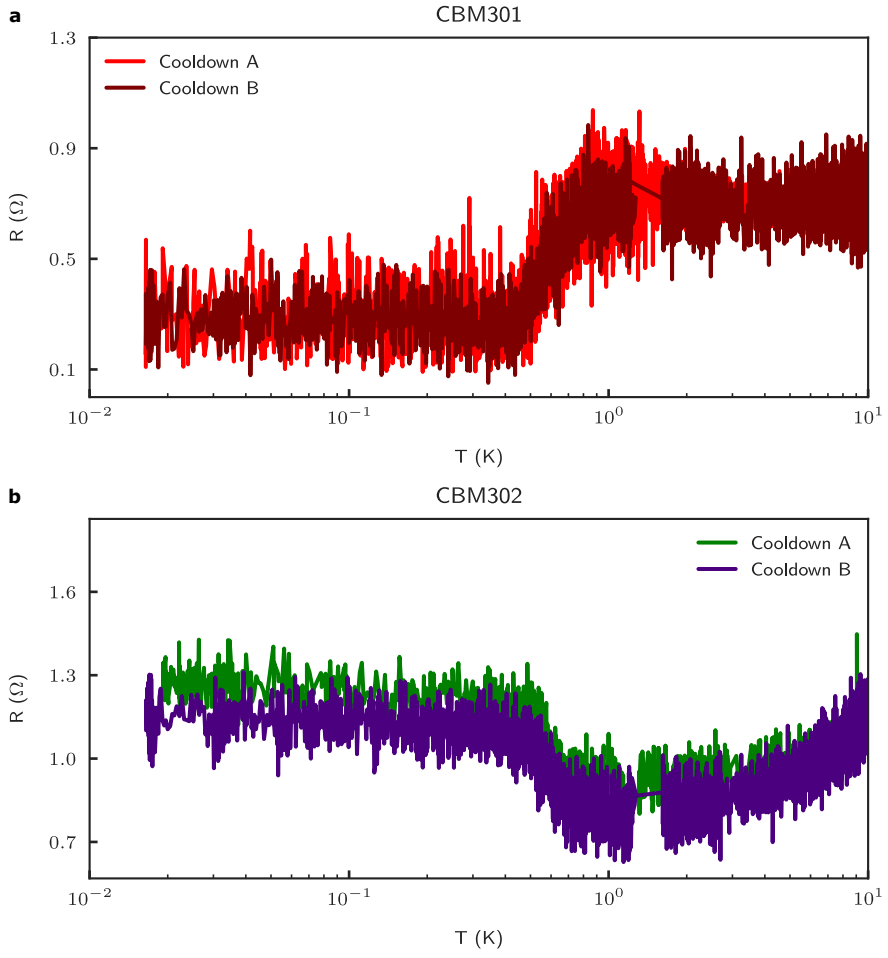

FIGURE B.7 – Temperature dependence of resistance for (a) CBM301 (b) and CBM302 measured during two different cooldown.

B.6 Transport Measurements at Higher Temperature

Electronic transport measurements were also performed at higher temperatures than shown in the main text, and they are shown in Fig.B.8. As expected, the monotonic increase in resistance with increasing temperature for VdP301 and VdP302 is observed. Note the increase in resistance observed at ∼400 mK for CBM301 is followed by a nearly-constant resistance value over a wide range of temperature up to ∼10 K, and subsequently a monotonic increase in resistance is observed at higher temperatures.

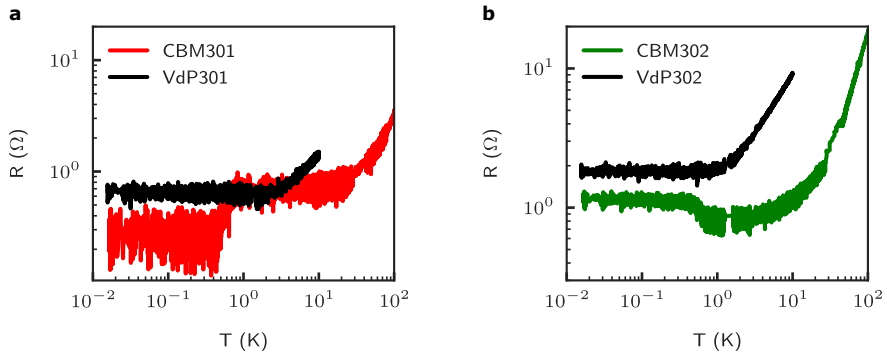

FIGURE B.8 – Temperature dependence of resistance up to 100 K for (a) CBM301, VdP301 and (b) CBM302, VdP302.

C

Supplementary Material : Nonlocal measurements and hydrodynamic reciprocity in high mobility electron flow

C.1 Heterostructure

The heterostructures used in this work to fabricate the devices were grown on undoped GaAs substrates and they are shown in Fig.C.1. Both heterostructures have a 700 nm thick buffer layer followed by a spacer layer deposited on top of the substrate (substrate is not shown). The distance between the dopant and the edge of the quantum well is denoted as the setback distance. Finally, the heterostructure is protected by a cap layer made of a material similar to the substrate.

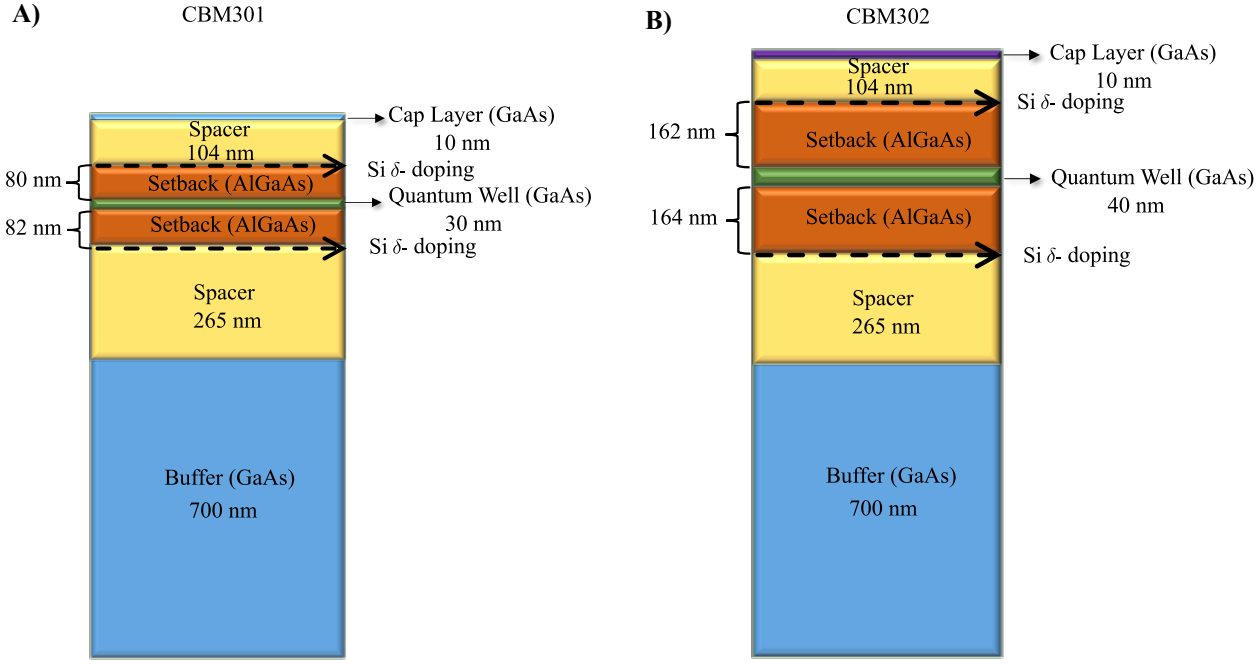

FIGURE C.1 – Heterostructure of wafers for sample (A) CBM301 and (B) CBM302. The figure indicates the materials used and the layer thickness.

C.2 Measurement Circuits

C.2.1 Local Measurement Circuit

The circuit in local transport measurements, depicted in Fig.C.2, consists of an SR830 lock-in amplifier, a 10 $M\Omega$ resistor and a SR560 pre-amplifier. It is a basic resistance measurement setup, where a fixed current is applied and the voltage difference is measured across the device. In this setup, an AC voltage of 200 mV from the SR830 is applied across the 10 $M\Omega$ resistor connected in series with the Corbino sample. This configuration allows for a constant current of 20 nA to be applied to the outermost contact of the multi-terminal Corbino, while the innermost contact is kept grounded. The voltage difference across the intermediate contacts is measured and amplified using the SR560 pre-amplifier with a gain of 100.

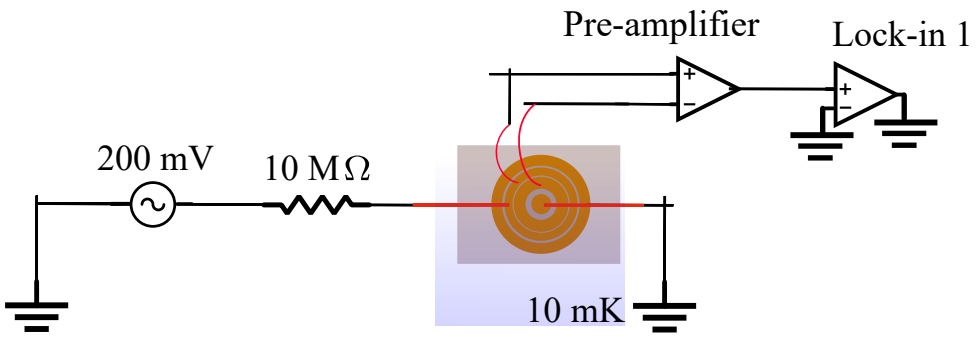

FIGURE C.2 – Local transport measurement circuit used to determine the four-point resistance of the Corbino sample with a fixed current of 20 nA.

C.2.2 Nonlocal Measurement Circuit

The nonlocal measurement circuit is identical to the local measurement circuit described above and uses the same elements. Here, an AC signal of 1 V is transmitted through the 10 $M\Omega$ resistor resulting in a 100 nA current as shown in Fig.C.3. This electric current flows across the inner two contacts by keeping the innermost contact grounded, and vice versa for Onsager measurements. The voltage difference

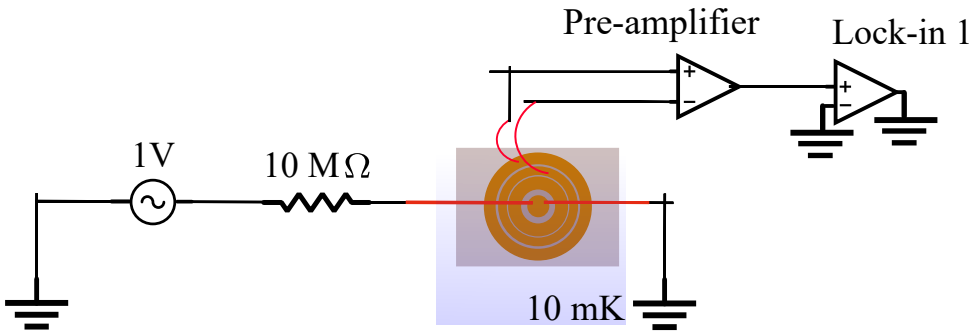

FIGURE C.3 – Nonlocal transport measurement circuit with a fixed current of 100 nA.

is measured across the two outer rings. To verify if any superconducting and/or proximity effects of the contacts contributed to our transport measurements, we conducted a DC-biased measurement with a 300 nA bias current. The obtained I-Vs were linear, demonstrating Ohmic electronic transport.

C.2.3 Lock-in Frequency

All transport measurements presented in the main text were conducted with lock-in signal frequencies of 73.51 Hz for CBM302 and 67.89 Hz for CBM301. To verify there was no frequency-dependent effects, we also performed the same measurements with lower lock-in signal frequencies of 13.957 Hz for CBM302 and 17.253 Hz for CBM301. The signal and its temperature dependence remains the same, albeit with smaller signal amplitudes, that we attribute to different cooldown conditions.

C.3 Probe Symmetry

To further confirm the results presented in Fig.2 of the main text, we also conducted nonlocal transport measurements using different probe configurations. The data obtained for both CBM301 and CBM302 at base temperature and zero magnetic fields ($B = 0\ T$) are shown in Fig.C.4. The results show that all probe symmetries

are respected in both devices.

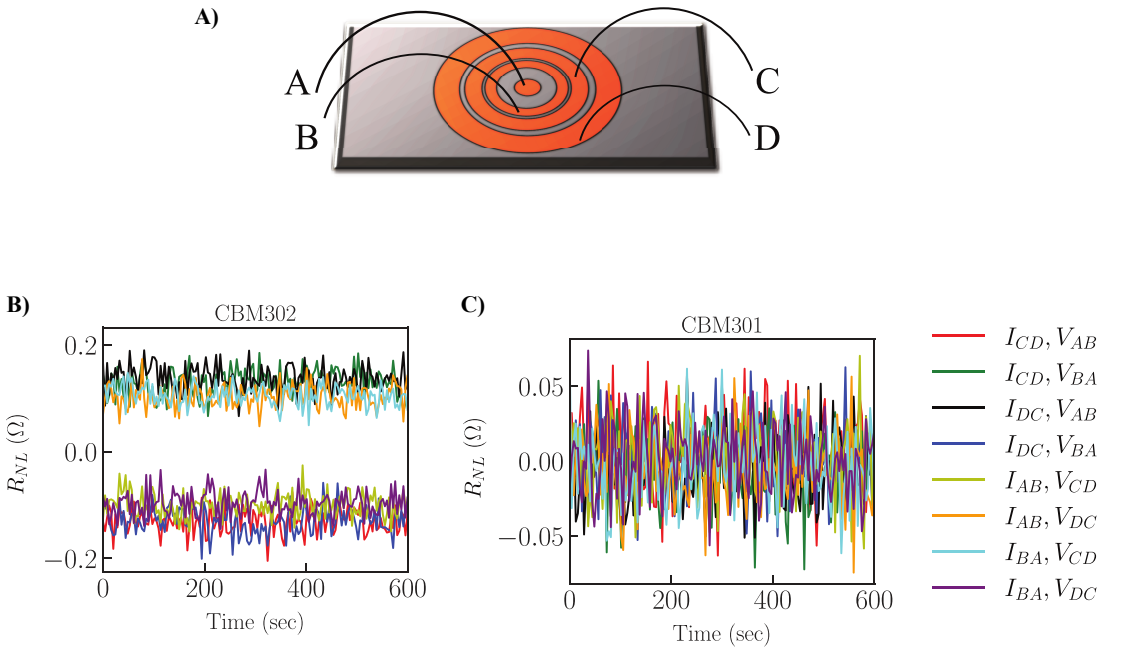

FIGURE C.4 – Panel (**A**) A cartoon of the Corbino device with each contact labeled as A, B, C and D. (**B**) and (**C**) show the nonlocal resistance measurements under various probe configurations in CBM302 and CBM301 respectively. The legend indicates contact configurations, where I is the applied current and V is the measured voltage difference.

C.4 Navier-Stokes in Hydrodynamics

C.4.1 Length Scales

As mentioned in the main text, the length scale conditions for hydrodynamic transport are $\ell_{MC} \ll W \ll \ell_{MR}$, where W is channel width, ℓ_{MC} is momentum conserving scattering mean-free path (in our case the $e-e$ scattering), and l_{MR} is momentum relaxing scattering mean-free path. At low temperatures ($T < 1\ K$) where phonon contribution is negligible, we consider only momentum relaxing scat-

tering due to electron-impurity,

$$\ell_{MR} = 5.22\mu\sqrt{n_e}, \tag{C.1}$$

where μ is carrier mobility and n_e is electron density. In our previously reported study [1], we verified experimentally that the electron density remains constant below 1 K, and therefore we consider ℓ_{MR} to be constant for both devices with scattering time $\tau_{MR} = \frac{v_f}{\ell_{MR}}$, where v_f is the Fermi velocity.

The quantum lifetime for electron-electron interaction was calculated using a well known theoretical expression from Guillani and Quinn [2]:

$$\frac{1}{\tau_{MC}} \approx \frac{(k_B T)^2}{2\pi\hbar E_f}\left[\log\left(\frac{E_f}{k_B T}\right) + \log\left(\frac{2q_{tf}}{k_f}\right) + 1\right], \tag{C.2}$$

where E_f k_f, q_{tf} and k_B are the Fermi energy, Fermi wave vector, Thomas-Fermi wave vector and Boltzmann constant, respectively.

In our simplified model, we consider a total scattering length making use of Matthiessen's rule, which is the mean-free path of any scattering event, given by

$$\ell_T^{-1} = \ell_{MC}^{-1} + \ell_{MR}^{-1}. \tag{C.3}$$

Hence the total lifetime τ_T can be written as

$$\tau_T^{-1} = \frac{v_f}{\ell_T} = v_f\left(\ell_{MC}^{-1} + \ell_{MR}^{-1}\right) = \left(\frac{v_f}{\ell_{MC}} + \frac{v_f}{\ell_{MR}}\right) = \tau_{MC}^{-1} + \tau_{MR}^{-1}. \tag{C.4}$$

C.4.2 Governing Equations

The Navier-Stokes equations for an incompressible viscous fluid with negligible pressure gradient are given by [3]:

$$\nabla \cdot \vec{u} = 0, \tag{C.5}$$

$$\frac{\partial \vec{u}}{\partial t} + \left(\vec{u} \cdot \vec{\nabla}\right) \vec{u} = \nu \vec{\nabla}^2 \vec{u} + \vec{f}. \tag{C.6}$$

$\vec{u}$ is electron velocity, ν is kinematic viscosity of the system given by $\nu = \frac{\hbar}{4m^*}\sqrt{2\pi n_e}\,\ell_{MC}$, and $\vec{f}$ is body force per unit mass. There are two main body forces that we consider: the electromagnetic (external) and momentum changes due to scattering (internal). As shown in the main text, the total body force per unit mass if given by

$$\vec{f} = \vec{f}_{EM} + \vec{f}_{scat} = -\frac{q_e}{m^*}\vec{\nabla}\phi + \frac{\vec{u}}{\tau}, \tag{C.7}$$

where q_e is electron charge $-e$, m^* is effective mass ($0.067m_e$ for GaAs/AlGaAs), τ is the effective mean-free scattering time $\tau^{-1} = \tau_{MC}^{-1} - \tau_{MR}^{-1}$, and ϕ represent the electric potential created by electron flow directed by an applied current.

C.4.3 Two-dimensional Geometries

In a multiring Corbino device, the 2DEG is formed by an annulus, hence the natural description of this system is in polar coordinates (r, θ), with the center contact as the origin. In the absence of a magnetic field, the symmetries of our system do not permit flow in the θ direction, as our current carries electrons along the r-axis [4]. As such, $\vec{u} = (u_r, 0, 0)$ and $\phi(r, \theta) = \phi(r)$, and as a result equations

C.5 and C.6 simplify to:

$$\frac{1}{r}\frac{\partial\left(ru_r\right)}{\partial r} = 0, \tag{C.8}$$

$$\frac{\partial u_r}{\partial t} + u_r\frac{\partial u_r}{\partial r} = \nu\left(\frac{1}{r}\frac{\partial}{\partial r}\left(r\frac{\partial u_r}{\partial r}\right) - \frac{u_r}{r^2}\right) - \frac{q_e}{m^*}\frac{\partial\phi}{\partial r} + \frac{u_r}{\tau}, \tag{C.9}$$

which in the steady state ($\frac{\partial u_r}{\partial t} \to 0$) has solutions:

$$u_r(r) = \frac{K}{r} \tag{C.10}$$

$$\begin{aligned}\phi(r) &= \frac{K^2}{2}\frac{m^*}{q_e}\left(\frac{1}{r^2} - \frac{1}{r_{gnd}^2}\right) + \frac{K}{\tau}\frac{m^*}{q_e}\log\left(\frac{r}{r_{gnd}}\right) \\ &= \frac{K}{\tau}\frac{m^*}{q_e}\log\left(\frac{r}{r_{gnd}}\right) + \mathcal{O}(K^2),\end{aligned} \tag{C.11}$$

where r_{gnd} is the reference position of the grounded contact edge. Noting that 2D current density is given by

$$J_r(r) = \frac{I}{2\pi r} = n_e q_e u_r = n_e q_e \frac{K}{r}, \tag{C.12}$$

we find that

$$|K| = \left|\frac{I}{2\pi n_e q_e}\right| \ll 1, \tag{C.13}$$

where the sign of I indicates the direction of current.

C.4.4 Hydrodynamic Reciprocity

In the realm of viscous hydrodynamic transport it is known that the reciprocity relation is satisfied [5] and the reciprocity identity for two different particle states, with a velocity $\vec{u}^{(1)}$ at position $r^{(1)}$ and $\vec{u}^{(2)}$ at position $r^{(2)}$ is

$$\vec{f}^{(1)} \cdot \vec{u}^{(2)} = \vec{f}^{(2)} \cdot \vec{u}^{(1)}, \tag{C.14}$$

where $\vec{f}^{(1)}$ and $\vec{f}^{(2)}$ are the corresponding body forces. In our case these two different states, labeled (1) and (2), denote the two Onsager configurations O1 and O2. The experimental evidence of satisfied reciprocity relations is presented in Fig.2D of the main text. Using the solutions in polar coordinates given by Eq.C.10-C.11 and the body force given by Eq.C.7, the reciprocity identity becomes

$$\begin{aligned} \vec{f}^{(1)} \cdot \vec{u}^{(2)} &= -\left(\frac{K}{\tau}\frac{m^*}{q_e}\frac{\partial}{\partial r}\log\left(\frac{r^{(1)}}{r_{gnd}}\right) - \frac{1}{\tau}\frac{K}{r^{(1)}}\right)\left(\frac{K}{r^{(2)}}\right) \\ &= \frac{1}{r^{(1)}r^{(2)}}\frac{K^2}{\tau}\left(1 - \frac{m^*}{q_e}\right), \qquad \text{(C.15)} \\ \vec{f}^{(2)} \cdot \vec{u}^{(1)} &= -\left(\frac{K}{\tau}\frac{m^*}{q_e}\frac{\partial}{\partial r}\log\left(\frac{r^{(2)}}{r_{gnd}}\right) - \frac{1}{\tau}\frac{K}{r^{(2)}}\right)\left(\frac{K}{r^{(1)}}\right) \\ &= \frac{1}{r^{(2)}r^{(1)}}\frac{K^2}{\tau}\left(1 - \frac{m^*}{q_e}\right). \qquad \text{(C.16)} \end{aligned}$$

Thus the hydrodynamic reciprocity relation $\vec{f}^{(1)} \cdot \vec{u}^{(2)} = \vec{f}^{(2)} \cdot \vec{u}^{(1)}$ is satisfied. This support our experimental observation of nonlocal resistance using distinctive Onsager probe configurations.

C.5 Simulation

Numerical simulations of Eq.C.8-C.9 were performed in Python via Finite-Difference Method (FDM) in the 2D polar coordinate system. In FDM, first-order and second-order spatial derivatives are discretized using the central difference approximation,

$$\frac{\partial f}{\partial x} \approx \frac{f(x+h) - f(x-h)}{2h} + \mathcal{O}(h^2), \qquad \text{(C.17)}$$

$$\frac{\partial^2 f}{\partial x^2} \approx \frac{f(x+h) + f(x-h) - 2f(x)}{h^2} + \mathcal{O}(h^2). \qquad \text{(C.18)}$$

We employ a 2D uniformly spaced mesh grid for axes (r,θ) with dimension (N_r, N_θ) and constant spacing Δr and $\Delta\theta$. As the θ axis is periodic, the spatial derivatives take the following form:

$$\frac{\partial f_{i,j}}{\partial r} = \frac{f_{i+1,j} - f_{i-1,j}}{2\Delta r}, \tag{C.19}$$

$$\frac{\partial f_{i,j}}{\partial \theta} = \frac{f_{i,(j+1)\bmod N_\theta} - f_{i,(j-1)\bmod N_\theta}}{2\Delta\theta}, \tag{C.20}$$

$$\frac{\partial^2 f_{i,j}}{\partial r^2} = \frac{f_{i+1,j} + f_{i-1,j} - 2f_{i,j}}{(\Delta r)^2}, \tag{C.21}$$

$$\frac{\partial^2 f_{i,j}}{\partial \theta^2} = \frac{f_{i,(j+1)\bmod N_\theta} + f_{i,(j-1)\bmod N_\theta} - 2f_{i,j}}{(\Delta\theta)^2}, \tag{C.22}$$

where mod denotes the modulus operator.

C.5.1 Iterative Solution

Simulations were performed iteratively over time, with time step Δt, using the approximation

$$\frac{\partial u}{\partial t} \approx \frac{u^{t+1} - u^t}{\Delta t} + \mathcal{O}(\Delta t). \tag{C.23}$$

Substituting into Eq.C.6, we obtain

$$\frac{\vec{u}^{t+1} - \vec{u}^t}{\Delta t} = \nu\vec{\nabla}^2\vec{u}^t - \left(\vec{u}^t \cdot \vec{\nabla}\right)\vec{u}^t + \vec{f}^t, \tag{C.24}$$

and solving for $\vec{u}^{t+1}$, we derive the update rule for velocity field at each iteration:

$$\vec{u^{t+1}} = \vec{u}^t + \Delta t\left(\nu\vec{\nabla}^2\vec{u}^t - \left(\vec{u}^t \cdot \vec{\nabla}\right)\vec{u}^t + \vec{f}^t\right). \tag{C.25}$$

Factoring in for the body forces and substituting Eq.C.7 yields

$$u^{\vec{t+1}} = \vec{u}^t + \Delta t \left(\nu \vec{\nabla}^2 \vec{u}^t - \left(\vec{u}^t \cdot \vec{\nabla} \right) \vec{u}^t - \frac{q_e}{m^*} \vec{\nabla} \phi^t + \frac{\vec{u}^t}{\tau} \right). \tag{C.26}$$

To obtain a solution for ϕ^t concurrently, we define a "guess" solution at each iteration:

$$\vec{u}^P \equiv \vec{u}^t + \Delta t \left(\nu \vec{\nabla}^2 \vec{u}^t - \left(\vec{u}^t \cdot \vec{\nabla} \right) \vec{u}^t + \frac{\vec{u}^t}{\tau} \right). \tag{C.27}$$

Substituting this into Eq.C.26, we obtain:

$$\vec{u}^{t+1} = \vec{u}^P - \Delta t \frac{q_e}{m^*} \vec{\nabla} \phi^t. \tag{C.28}$$

A solution for ϕ^t is obtained by taking the divergence of both sides of Eq.C.28. Continuity equation (Eq.C.5) imposes the condition that $\vec{\nabla} \cdot \vec{u}^{t+1} = 0$, however this condition may not necessarily be true for our guess velocity $\vec{u}^P$ (Eq.C.27). We are left with the following Poisson equation:

$$\vec{\nabla}^2 \phi^t = \frac{1}{\Delta t} \frac{m^*}{q_e} \left(\vec{\nabla} \cdot \vec{u}^P \right). \tag{C.29}$$

In 2D cylindrical coordinates, the Laplacian term of Eq.C.29 can be written as

$$\vec{\nabla}^2 \phi^t = \frac{\partial^2 \phi^t}{\partial r^2} + \frac{1}{r} \frac{\partial \phi^t}{\partial r} + \frac{1}{r^2} \frac{\partial^2 \phi^t}{\partial \theta^2}. \tag{C.30}$$

Using the discretized spatial derivative forms Eq.C.19-C.21 of Eq.C.30 and solving for ϕ^t yields:

$$\phi^t_{i,j} = \frac{1}{2}\left(\frac{(\Delta r)^2 (r\Delta\theta)^2}{(\Delta r)^2 + (r\Delta\theta)^2}\right)\left(\frac{\phi^t_{i+1,j} + \phi^t_{i-1,j}}{(\Delta r)^2} + \frac{\phi^t_{i,(j+1)\bmod N_\theta} + \phi^t_{i,(j-1)\bmod N_\theta}}{(r\Delta\theta)^2} + \frac{1}{r}\frac{\phi^t_{i+1,j} - \phi^t_{i-1,j}}{2\Delta r} - \frac{1}{\Delta t}\frac{q_e}{m^*}\left(\vec{\nabla}\cdot\vec{u}^P_{i,j}\right)\right). \quad \text{(C.31)}$$

Denoted as Poisson iterations, Eq.C.31 is calculated multiple times per time step. In our simulations, 100 Poisson iterations for each 5000 time steps were performed. The simulation converges to the steady-state solution of Eq.C.8-C.9 when $\frac{\partial u^t}{\partial t} \to 0$. The convergence condition equivalently implies ϕ^t tends towards a constant value, which is shown in Fig.C.5 for CBM302 at $T = 1\ K$. Although we utilized the symmetries of our system to simplify equations Eq.C.5-C.6 and derive analytic solutions Eq.C.10-C.11, our simulation framework avoids such approximations to retain general applicability.

C.5.2 Nonlocal Simulations

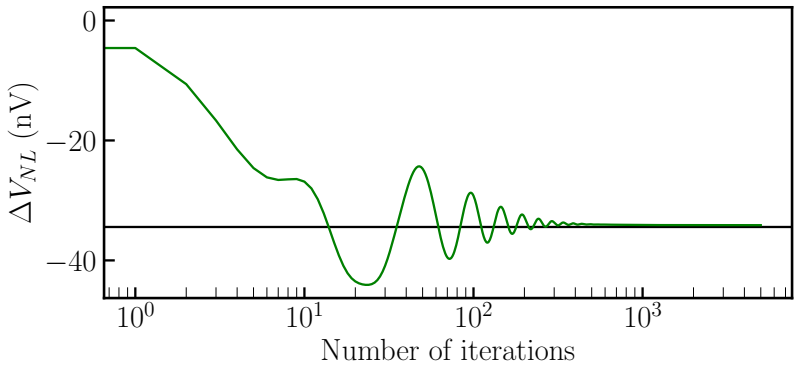

FIGURE C.5 – Convergence of nonlocal simulations to analytic solutions. ΔV for all 5000 time steps of $\Delta t = 10^{-15}\ s$ was recorded for CBM302 simulations at $T = 1\ K$. Simulations converge within acceptable limits to the analytic results (shown in black) after 1000 iterations.

For nonlocal simulations, we simulated only the region of the Corbino device with

driven current, using the same experimental parameters. We then extrapolated our electric potential profile to the nonlocal region by curve fitting to a general function resembling analytic solution C.11. Since we only simulate the active region of the 2DEG fluid (without Ohmic contacts), we measure the potential difference edge-to-edge between the voltage probes in the nonlocal region. Nonlocal simulations were performed on a 2D $N_r = 61$ by $N_\theta = 21$ grid, with $\Delta r = 10^{-5}$ and $\Delta\theta = \pi \cdot 10^{-1}$. A time step of $\Delta t = 10^{-15}$ was taken, and 5000 iterations per simulation, each with 100 Poisson steps, were performed.

Due to the substantial size difference between the inner and outer regions of the Corbino device, the resolution of extrapolated data for reciprocity simulations was limited so severely that we could not derive any meaningful conclusions.

C.5.3 AC Simulations

The simulations performed were under the quasi-DC regime, whereby the input current I_0 is proportional to the root-mean-square value set on the SR830 lock-in amplifier, I_{RMS}, by a factor of $\sqrt{2}$. In this regime, the output would be proportional to the root-mean-square value measured by our lock-in by the same factor.

To confirm our quasi-DC model, we performed AC simulations by simulating uniformly spaced points in our signal period. We then performed a root-mean-square calculation of our AC data points, which yielded *nearly* identical results to that of our quasi-DC simulations, shown in C.6. Each simulation was performed with the results of the previous one in the signal period, adjusted based on

$$\begin{aligned} I(t+\Delta t) &= I_0 \cos\big(\omega(t+\Delta t)\big) \\ &= I_0 \cos(\omega t)\cos(\omega\Delta t) - I_0 \sin(\omega t)\sin(\omega\Delta t) \\ &= I(t)\Big(\cos(\omega\Delta t) - \tan(\omega t)\sin(\omega\Delta t)\Big), \end{aligned} \tag{C.32}$$

where $\omega = 2\pi f$, and f is frequency.

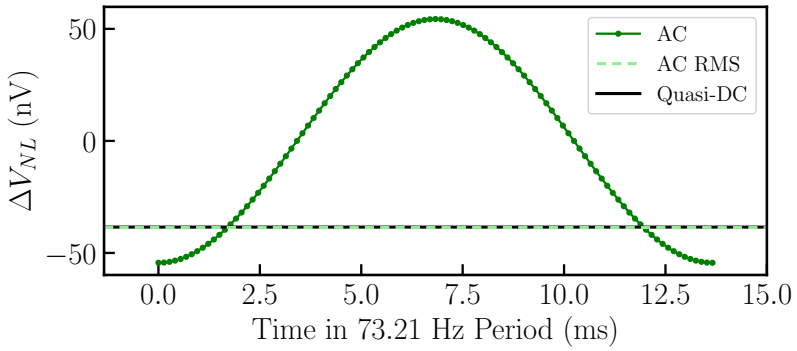

FIGURE C.6 – Comparison between AC and quasi-DC. Green points are the resulting ΔV along one period of a 73.21 Hz AC signal, simulated in CBM302 at base temperature $T = 1\ K$ for nonlocal configuration. The light green dashed line is the computed root-mean-square value of the AC signal simulated. The black line is the result of the quasi-DC simulation of the same sample and temperature, using the model described in this paper.

C.5.4 Validity of Extrapolation

To verify the extrapolation technique used in this study, we performed another set of simulations where we consider the entire annular rings. A key difference between this simulation and the previous one is that we don't assume that velocity $\vec{u} = \int \vec{v} f d\vec{v}$ is equal to the drift velocity $\vec{\lambda}$, defined as $J_r = n_e q_e \vec{\lambda}$. As such, starting

from the following Boltzmann equation

$$\frac{\partial f_{\vec{v}}}{\partial t} + \vec{v} \cdot \frac{\partial f_{\vec{v}}}{\partial \vec{r}} + \frac{q_e}{m^*} \vec{E} \cdot \frac{\partial f^0_{\vec{v}}}{\partial \vec{v}} = -\frac{f_{\vec{v}} - f^0_{\vec{v}}}{\tau_{MR}} - \frac{f_{\vec{v}} - f^0_{\vec{\lambda}}}{\tau_{MC}}, \tag{C.33}$$

the first velocity moment yields the following Navier-Stokes-like equation

$$\frac{\partial \vec{u}}{\partial t} + \left(\vec{u} \cdot \vec{\nabla}\right) \vec{u} = \nu \vec{\nabla}^2 \vec{u} - \frac{q_e}{m^*} \vec{\nabla} \phi - \frac{\vec{u}}{\tau_{MR}} - \frac{\vec{u} - \vec{\lambda}}{\tau_{MC}}. \tag{C.34}$$

Within the current path, we set $\vec{u} = \vec{\lambda}$. The potential $\phi = \int dr \frac{\partial \phi}{\partial r}$ is calculated directly from Eq.C.34 within the current path starting from zero at the grounded inner contact. Outside of the current path, all values are set to zero. The initial conditions are shown in black in Fig. C.7. The boundary conditions of the regions outside the current path region are calculated based on the taylor series centered at the boundary for adjacent values. To determine the derivatives of $\vec{u}$, the constant K from Eq.C.10 is determined for the adjacent value. For ϕ, derivatives are calculated directly from Eq.C.34 at the boundary.

To prevent errors caused by the discontinuity at the current source, we perform N_{sub} subiterations to determine our guess velocity $\vec{u}^P$ based on the following sequence

$$\vec{u}^P_0 = \vec{u}^t, \tag{C.35}$$

$$\vec{u}^P_{n+1} = \vec{u}^P_n + \frac{\Delta t}{N_{sub}} \left(\nu \vec{\nabla}^2 \vec{u}^P_n - \left(\vec{u}^P_n \cdot \vec{\nabla}\right) \vec{u}^P_n - \frac{\vec{u}^P_n}{\tau_{MR}} - \frac{\vec{u}^P_n - \vec{\lambda}}{\tau_{MC}} \right), \tag{C.36}$$

and use $\vec{u}^P_{N_{sub}}$ to solve the Poisson equation. We set $N_{sub} = \lfloor \sqrt{N_r} \rfloor$ as the discontinuity effects scale with $\Delta r \propto \frac{1}{N_r}$.

The potential profile and electron velocity, obtained from simulating the entire region over different iterations, along with the result from the extrapolation technique are shown in Fig.C.7. The potential difference between the outer two rings, calculated through the entire region simulation, after 20000 iteration was found to be $-36.5nV$, and the extrapolation technique gave a value of $-34.1nV$ after 1458 iterations.

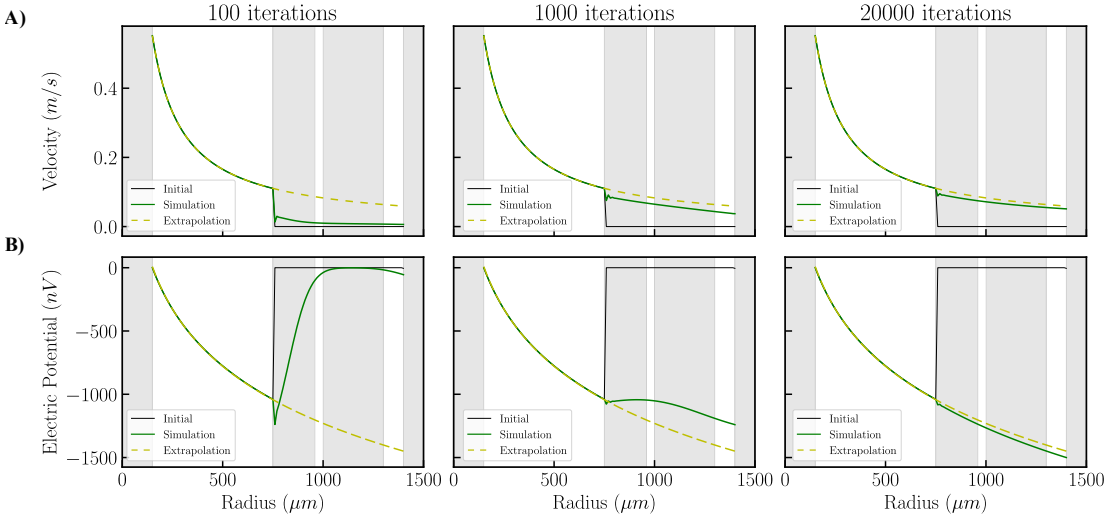

FIGURE C.7 – Comparison of velocity (A) and electric potential (B) between the extrapolation technique and full region simulation for CBM302 at $T = 1\ K$ at different number of iterations. The initial conditions of the full region simulation are shown in black, and converges just under 20000 iterations with $N_r = 126$, shown in green. The extrapolation technique, depicted by a dashed yellow line, converges after 1458 iterations with $N_r = 61$. Both simulations are performed with $\Delta r = 10^{-5}$. The potential profiles from both simulations are in agreement, with minor discrepancies likely due to error propagation from discontinuity at the contact.

C.6 References

[1] S. Vijayakrishnan, F. Poitevin, O. Yu, Z. Berkson-Korenberg, M. Petrescu, M. P. Lilly, T. Szkopek, K. Agarwal, K. W. West, L. N. Pfeiffer, and G. Gervais, Nat Commun **14**, 3906 (2023).

[2] Gabriele F. Giuliani, and John J. Quinn, Phys. Rev. B **26**, 4421 (1982).

[3] L. D. Landau, and E. M. Lifshitz, *Fluid Mechanics* : Volume 6 of Course of Theoretical Physics Series (Butterworth-Heinemann, Oxford, 1987), 2$^{\text{nd}}$ edition.

[4] D. A. Kleinman, A. L. Schawlow, J. Appl. Phys. **31**, 2176 (1960).

[5] W. E. Olmstead, Acta Mechanica **21**, 289 (1975).

References

[1] S. Sachdev, Quantum phase transitions, Cambridge Univ. Press, Massachusetts (2011).

[2] R. N. Gurzhi, Hydrodynamic effects in solids at low temperature, Sov. Phys. Usp. **94**, 689 (1968).

[3] B. I. Halperin, P. C. Hohenberg, Hydrodynamic theory of spin waves, Phys. Rev. **188**, 898 (1969).

[4] M. J. M. de Jong, and L. W. Molenkamp, Hydrodynamic electron flow in high-mobility wires, Phys. Rev. B **51**, 13389 (1995).

[5] R. Krishna Kumar, D. A. Bandurin, F. M. D. Pellegrino, Y. Cao, A. Principi, H. Guo, G. H. Auton, Shalom M. Ben Shalom, L. A. Ponomarenko, G. Falkovich, K. Watanabe, T. Taniguchi, I. V. Grigorieva, L. S. Levitov, M. Polini, and A. K. Geim, Superballistic flow of viscous electron fluid through graphene constrictions, Nat. Phys. **13**, 1182 (2017).

[6] D. A. Bandurin, A. V. Shytov, L. S. Levitov, R. K. Kumar, A. I. Berdyugin, M. Ben Shalom, I. V. Grigorieva, A. K. Geim, and G. Falkovich, Fluidity onset in graphene, Nat. Commun. **9**, 4533 (2018).

[7] G. M. Gusev, A. D. Levin, E. V. Levinson, and A. K. Bakarov, Viscous electron flow in mesoscopic two-dimensional electron gas, AIP Adv. **8**, 025318 (2018).

[8] A. Lucas, and K. C. Fong, J. Phys. Condens. Matter **30**, 053001 (2018).

[9] M. Polini, and A. K. Geim, Physics Today **73**, 28 (2020).

[10] A. Gupta, J. J. Heremans, G. Kataria, M. Chandra, S. Fallahi, G. C. Gardner, and M. J. Manfra, Hydrodynamic and ballistic transport over large length scales in GaAs/AlGaAs, Phys. Rev. Lett. **126**, 076803 (2021).

[11] A. C. Keser, D. Q. Wang, O. Klochan, D. Y. H. Ho, O. A. Tkachenko, V. A. Tkachenko, D. Culcer, S. Adam, I. Farrer, D. A. Ritchie, O. P. Sushkov, and A. R. Hamilton, Geometric control of universal hydrodynamic flow in a two-dimensional electron fluid, Phys. Rev. X **11**, 031030 (2021).

[12] G. M. Gusev, A. S. Jaroshevich, A. D. Levin, Z. D. Kvon, and A. K. Bakarov, Viscous magnetotransport and Gurzhi effect in bilayer electron system, Phys. Rev. B **103**, 075303 (2021).

[13] A. S. Kumar, C. Liu, S. Liu, L. N. Pfeiffer, K. W. West, A. Levchenko, and X. P. Gao, Anomalous high-temperature magnetoresistance in a dilute 2D hole system, Phys. Rev. Lett. **130**, 266302 (2023).

[14] A.A. Abrikosov, and I.M. Khalatnikov, The theory of a Fermi liquid (the properties of liquid ^{3}He at low temperatures), Rep. Prog. Phys. **22**, 329 (1959).

[15] D. Vollhardt, P. Wölfle, The superfluid phases of helium 3, CRC Press, London (1990).

[16] R. N. Gurzhi, Minimum of resistance in impurity-free conductors, Sov. Phys. JETP **17**, 521 (1963).

[17] S. Vijayakrishnan, F. Poitevin, O. Yu, Z. Berkson-Korenberg, M. Petrescu, M. P. Lilly, T. Szkopek, K. Agarwal, K. W. West, L. N. Pfeiffer, and G. Gervais, Anomalous electronic transport in high-mobility Corbino rings, Nat. Commun. **14**, 3906 (2023).

[18] S. Vijayakrishnan, Z. Berkson-Korenberg, J. Mainville, L. W. Engel, M. P. Lilly, K. W. West, L. N. Pfeiffer, and G. Gervais, Two-dimensional hydrodynamic viscous electron flow in annular Corbino rings, arXiv:2405.17588 (2024).

[19] J. E. Lilienfeld, Method and apparatus for controlling electric currents, U. S. Patent No. 1745175 (Issued January 18, 1930).

[20] A. S. Grove, and D. J. Fitzgerald, Surface effects on p-n junctions: characteristics of surface space-charge regions under non-equilibrium conditions, Solid-State Electronics **9**, 783 (1996).

[21] A. S. Grove, and D. J. Fitzgerald, Physics of semiconductor devices, Wiley-Interscience, New York (1996).

[22] H. L. Störmer, R. Dingle, A. Gossard, W. Wiegmann, and M. Sturge, Two-dimensional electron gas at a semiconductor-semiconductor interface, Solid State Commun. **29**, 705 (1979).

[23] H. L. Störmer, R. Dingle, A. C. Gossard, W. Wiegmann, Electron mobilities in modulation-doped semiconductor heterojunction superlattices, Appl. Phys. Lett. **33**, 665 (1978).

[24] H. L. Störmer, Nobel Lecture: The fractional quantum Hall effect, Rev. Mod. Phys. **71**, 875 (1999).

[25] J. H. English, A. C. Gossard, H. L. Störmer, and K. W. Baldwin, GaAs structures with electron mobility of 5×10^6 cm^2/Vs, Appl. Phys. Lett. **50**, 1826 (1987).

[26] M. Shayegan, V. J. Goldman, C. Jiang, T. Sajoto, and M. Santos, Growth of low-density two-dimensional electron system with very high mobility by molecular beam epitaxy, Appl. Phys. Lett. **52**, 1086 (1988).

[27] C. Jiang, D. C. Tsui, and G. Weimann, Threshold transport of high-mobility two-dimensional electron gas in GaAs/AlGaAs heterostructures, Appl. Phys. Lett. **53**, 1533 (1988).

[28] L. Pfeiffer, K. W. West, H. L. Störmer, and K. W. Baldwin, Electron mobilities exceeding 10^7 cm^2/Vs in modulation-doped, Appl. Phys. Lett. **55**, 1888 (1989).

[29] E. H. Hwang and S. Das Sarma, Limit to two-dimensional mobility in modulation-doped GaAs quantum structures: How to achieve a mobility of 100 million, Phys. Rev. B **77**, 235437 (2008).

[30] V. Umansky, M. Heiblum, Y. Levinson, J. Smet, J. Nübler, and M. Dolev, MBE growth of ultra-low disorder 2DEG with mobility exceeding $35 \times 10^6 cm/Vs$, J. Cryst. Growth **311**, 1658 (2009).

[31] D. G. Schlom and L. N. Pfeiffer, Upward mobility rocks, Nat. Mater. **9**, 881 (2010).

[32] Y. J. Chung, K. A. Villegas Rosales, K. W. Baldwin, K. W. West, M. Shayegan, and L. N. Pfeiffer, Working principles of doping-well structures for high-mobility two-dimensional electron systems, Phys. Rev. Mater. **4**, 044003 (2020).

[33] Y. J. Chung, K. A. Villegas-Rosales, K. W. Baldwin, P. T. Madathil, K. W. West, M. Shayegan, and L. N. Pfeiffer, Ultra-high-quality two-dimensional electron systems, Nat. Mater. **20**, 632 (2021).

[34] S. Ahn and S. Das Sarma, Density-dependent two-dimensional optimal mobility in ultra-high-quality semiconductor quantum wells, Phys. Rev. Mater. **6**, 014603 (2022).

[35] Y. Huang, B. I. Shklovskii, and M. A. Zudov, Scattering mechanisms in state-of-the-art GaAs/AlGaAs quantum wells, Phys. Rev. Mater. **6**, L061001 (2022).

[36] Y. J. Chung, A. Gupta, K. W. Baldwin, K. W. West, M. Shayegan, and L. N. Pfeiffer, Understanding limits to mobility in ultrahigh-mobility GaAs two-dimensional electron systems: 100 million cm^2/Vs and beyond, Phys. Rev. B **106**, 075134 (2022).

[37] L. Pfeiffer and K. W. West, The role of MBE in recent quantum Hall effect physics discoveries, Physica E: Low-dimensional Systems and Nanostructures **20**, 57 (2003).

[38] K. Ploog, Delta-($\delta-$) doping in MBE-grown GaAs : Concept and device application, J. Cryst. Growth **81**, 304 (1987).

[39] M. Santos, T. Sajoto, A. Zrenner, and M. Shayegan, Migration of Si in δ-doped GaAs and Al_xGa_{1-x} As: Effect of substrate temperature, Surf. Sci. **228**, 255 (1990).

[40] A. M. Lanzillotto, M. Santos, and M. Shayegan, Secondary-ion mass spectrometry study of the migration of Si in planar-doped GaAs and $Al_{0.25}Ga_{0.75}As$, Appl. Phys. Lett. **55**, 1445 (1989).

[41] E. F. Schubert, Delta doping of III-V compound semiconductors : Fundamentals and device applications, J. Vac. Sci. Technol. A **8**, 2980 (1990).

[42] N. W. Ashcroft and N. D. Mermin, Solid state physics, Harcourt college publishers, Boston (1976).

[43] S. Datta, Electronic transport in mesoscopic systems, Cambridge University Press, New York (1997).

[44] Cory R. Dean, A study of the fractional quantum Hall energy gap at half filling, PhD thesis, McGill University (2008).

[45] B. A. Schmidt, Specific heat in the fractional quantum Hall regime, PhD thesis, McGill University (2019).

[46] M. P. Marder, Condensed matter physics, John Wiley & Sons Inc. (2000).

[47] K. von Klitzing, G. Dorda, and M. Pepper, New method for high-accuracy determination of the fine-structure constant based on quantized Hall resistance, Phys. Rev. Lett. **45**, 494 (1980).

[48] D. C. Tsui, H. L. Störmer, and A. C. Gossard, Two-dimensional magnetotransport in the extreme quantum limit, Phys. Rev. Lett. **48**, 1559 (1982).

[49] J. K. Jain, Composite-fermion approach for the fractional quantum Hall effect, Phys. Rev. Lett. **63**, 199 (1989).

[50] J. K. Jain, Theory of the fractional quantum Hall effect, Phys. Rev. B **61**, 7653 (1990).

[51] G. Moore, N. Read, Non abelions in the fractional quantum hall effect, Nuclear Physics B **360**, 362 (1991).

[52] B. I. Halperin, Quantized Hall conductance, current-carrying edge states, and the existence of extended states in a two-dimensional disordered potential, Phys. Rev. B **25**, 2185 (1982).

[53] M. Petrescu, Z. Berkson-Korenberg, S. Vijayakrishnan, K. W. West, L. N. Pfeiffer and G. Gervais, Large composite fermion effective mass at filling factor 5/2, Nat. Commun. **14**, 7250 (2023).

[54] S. Vijayakrishnan, F. Poitevin, O. Yu, Z. Berkson-Korenberg, M. Petrescu, M. P. Lilly, T. Szkopek, K. Agarwal, K. W. West, L. N. Pfeiffer, and G. Gervais, Anomalous electronic transport in high-mobility Corbino rings, Nat. Commun. **14**, 3906 (2023).

[55] O. M. Corbino, Phys. Z. **12**, 561 (1911).

[56] B. J. van Wees, H. van Houten, C. W. J. Beenakker, J. G. Williamson, L. P. Kouwenhoven, D. van der Marel, and C. T. Foxon, Quantized conductance of point contacts in a two-dimensional electron gas, Phys. Rev. Lett. **60**, 848 (1988).

[57] D. A. Wharam, T. J. Thornton, R. Newbury, M. Pepper, H. Ahmed, J. E. F. Frost, D. G. Hasko, D. C. Peacock, D. A. Ritchie, and G. A. C. Jones, One-dimensional transport and the quantisation of the ballistic resistance, J. Phys. C: Sol. Stat. Phys. **21**, L209 (1988).

[58] R. de Picciotto, H. Stormer, L. Pfeiffer, K. Baldwin, and K. West, Four-terminal resistance of a ballistic quantum wire, Nature **411**, 6833 (2001).

[59] L.D. Landau, The Theory of a Fermi Liquid, Sov. Phys. JETP **3**, 920 (1957).

[60] I. Torre, A. Tomadin, A. K. Geim, and M. Polini, Nonlocal transport and the hydrodynamic shear viscosity in graphene, Phys. Rev. B **92**, 165433 (2015).

[61] L. Levitov and G. Falkovich, Electron viscosity, current vortices and negative nonlocal resistance in graphene, Nat. Phys. **12**, 672 (2016).

[62] J. C. Wheatley, O. Vilches, and W. Abel, Principles and methods of dilution refrigeration, Phys. Physique Fiz. **4**, 1 (1968).

[63] Y. Huang, Q. Yu, Q. Chen, and R. Wang, Viscosity of liquid and gaseous helium-3 from 3 mk to 500 k, Cryogenics **51**, 538 (2012).

[64] Sankar Das Sarma, and Yunxiang Liao, Know the enemy : 2D Fermi liquids, Annals of Physics **435**, 168495 (2021).

[65] L. D. Landau, and E. M. Lifshitz, Fluid mechanics : volume 6 of course of theoretical physics series, Butterworth-Heinemann, Oxford (1987).

[66] A. Tomadin, G. Vignale, and M. Polini, Corbino disk viscometer for 2D quantum electron liquids, Phys. Rev. Lett. **113**, 235901 (2014).

[67] A. C. Keser, D. Q. Wang, O. Klochan, D. Y. H. Ho, O. A. Tkachenko, V. A. Tkachenko, D. Culcer, S. Adam , I. Farrer , D. A. Ritchie, O. P. Sushkov, and A. R. Hamilton, Geometric control of universal hydrodynamic flow in a two-dimensional electron fluid, Phys. Rev. X **11**, 031030 (2021).

[68] D. A. Bandurin, I. Torre, R. K. Kumar, M. B. Shalom, A. Tomadin, A. Principi, G. Auton, E. Khestanova, K. S. Novoselov, I. V. Grigorieva, L. A. Ponomarenko, A. K. Geim, and M. Polini, Negative local resistance caused by viscous electron backflow in graphene, Science **351**, 1055 (2016).

[69] Z. -Z. Yu, M. Haerle, J. W. Zwart, J. Bass, W. P. Pratt, Jr., and P. A. Schroeder, Negative temperature derivative of resistivity in thin potassium samples : The Gurzhi effect ?, Phys. Rev. Lett. **52**, 368 (1984).

[70] R. N. Gurzhi, A. N. Kalinenko, and A. I. Kopeliovich, Electron-electron collisions and a new hydrodynamic effect in two-dimensional electron gas, Phys.

Rev. Lett. **74**, 3872 (1995).

[71] J. Crossno, J. K. Shi, K. Wang, X. Liu, A. Harzheim, A. Lucas, S. Sachdev, P. Kim, T. Taniguchi, K. Watanabe, T. A. Ohki, and J. G. Hone, Observation of the Dirac fluid and the breakdown of the Wiedemann-Franz law in graphene, Science **351**, 1058 (2016).

[72] P. J. W. Moll, P. Kushwaha, N. Nandi, B. Schmidt, and A. P. Mackenzie, Evidence for hydrodynamic electron flow in $PdCoO_2$, Science **351**, 1061 (2016).

[73] A. Shytov, J. F. Kong, G. Falkovich, and L. Levitov, Particle collisions and negative nonlocal response of ballistic electrons, Phys. Rev. Lett. **121**, 176805 (2018).

[74] M. Chandra, G. Kataria, D. Sahdev, and R. Sundararaman, Hydrodynamic and ballistic AC transport in two-dimensional Fermi liquids, Phys. Rev. B **99**, 165409 (2019).

[75] M. Chandra, G. Kataria, and D. Sahdev, Quantum critical ballistic transport in two-dimensional Fermi liquids, arXiv:1910.13737 (2019).

[76] M. J. H. Ku, T. X. Zhou, Q. Li, Y. J. Shin, J. K. Shi, C. Burch, L. E. Anderson, A. T. Pierce, Y. Xie, A. Hamo, U. Vool, H. Zhang, F. Casola, T. Taniguchi, K. Watanabe, M. M. Fogler, P. Kim, A. Yacoby and R. L. Walsworth, Imaging viscous flow of the Dirac fluid in graphene, Nature **583**, 537 (2020).

[77] J. A. Sulpizio, L. Ella, A. Rozen, J. Birkbeck, D. J. Perello, D. Dutta, M. Ben-Shalom, T. Taniguchi, K. Watanabe, T. Holder, R. Queiroz, A. Principi, A. Stern, T. Scaffidi, A. K. Geim and S. Ilani, Visualizing Poiseuille flow of hydrodynamic electrons, Nature **576**, 75 (2019).

[78] B. A. Braem, F. M. D. Pellegrino, A. Principi, M. Röösli, C. Gold, S. Hennel, J. V. Koski, M. Berl, W. Dietsche, W. Wegscheider, M. Polini, T. Ihn, and K. Ensslin, Scanning gate microscopy in a viscous electron fluid, Phys. Rev. B **98**, 241304 (2018).

[79] I. Torre, A. Tomadin, A. K. Geim, and M. Polini, Nonlocal transport and the hydrodynamic shear viscosity in graphene, Phys. Rev. B **92**, 165433 (2015).

[80] F. M. D. Pellegrino, I. Torre, A. K. Geim, and M. Polini, Electron hydrodynamics dilemma: Whirlpools or no whirlpools, Phys. Rev. B **94**, 155414 (2016).

[81] P. S. Alekseev, Negative magnetoresistance in viscous flow of two-dimensional electrons, Phys. Rev. Lett. **117**, 166601 (2016).

[82] T. Scaffidi, N. Nandi, B. Schmidt, A. P. Mackenzie, and J. E. Moore, Hydrodynamic electron flow and Hall viscosity, Phys. Rev. Lett. **118**, 226601 (2017).

[83] T. Holder, R. Queiroz, and A. Stern, Unified description of the classical Hall viscosity, Phys. Rev. Lett. **123**, 106801 (2019).

[84] A. Levchenko, S. Li, and A. V. Andreev, Hydrodynamic electron flow and its manifestations in 2D materials, Phys. Rev. B **106**, L201306 (2022).

[85] S. Ahn and S. Das Sarma, Hydrodynamics, viscous electron fluid, and Wiedeman-Franz law in two-dimensional semiconductors, Phys. Rev. B **106**, L081303 (2022).

[86] J. Gooth, F. Menges, N. Kumar, V. S$\ddot{u}\beta$, C. Shekhar, Y. Sun, U. Drechsler, R. Zierold, C. Felser, and B. Gotsmann, Thermal and electrical signatures of a hydrodynamic electron fluid in tungsten diphosphide Nat. Commun. **9**, 4093 (2018).

[87] G. M. Gusev, A. D. Levin, E. V. Levinson, and A. K. Bakarov, Viscous transport and Hall viscosity in a two-dimensional electron system, Phys. Rev. B **98**, 161303 (2018).

[88] A. D. Levin, G. M. Gusev, E. V. Levinson, Z. D. Kvon, and A. K. Bakarov, Vorticity-induced negative nonlocal resistance in a viscous two-dimensional electron system, Phys. Rev. B **97**, 245308 (2018).

[89] A. I. Berdyugin, S. G. Xu, F. M. D. Pellegrino, R. K. Kumar, A. Principi, I. Torre, M. B. Shalom, T. Taniguchi, K. Watanabe, I. V. Grigorieva, M. Polini, A.

K. Geim, and D. A. Bandurin, Measuring Hall viscosity of graphene's electron fluid, Science **364**, 162 (2019).

[90] M. Kim, S. G. Xu, A. I. Berdyugin, A. Principi, S. Slizovskiy, N. Xin, P. Kumaravadivel, W. Kuang, M. Hamer, R. Krishna Kumar, R. V. Gorbachev, K. Watanabe, T. Taniguchi, I. V. Grigorieva, V. I. Fal'ko, M. Polini and A. K. Geim., Control of electron-electron interaction in graphene by proximity screening, Nat. Commun. **11**, 1 (2020).

[91] O. E. Raichev, G. M. Gusev, A. D. Levin, and A. K. Bakarov, Manifestations of classical size effect and electronic viscosity in the magnetoresistance of narrow two-dimensional conductors : Theory and experiment, Phys. Rev. B **101**, 235314 (2020).

[92] L. V. Ginzburg, C. Gold, M. P. Röösli, C. Reichl, M. Berl, W. Wegscheider, T. Ihn, and K. Ensslin, Superballistic electron flow through a point contact in a Ga[Al]As heterostructure, Phys. Rev. Research **3**, 023033 (2021).

[93] L. Ella, A. Rozen, J. Birkbeck, M. B. Shalom, D. Perello, J. Zultak, T. Taniguchi, K. Watanabe, A. K. Geim, S. Ilani, and J. A. Sulpizio, Simultaneous voltage and current density imaging of flowing electrons in two dimensions, Nat. Nanotechnol. **14**, 480 (2019).

[94] C. Kumar, J. Birkbeck, J. A. Sulpizio, D. Perello, T. Taniguchi, K. Watanabe, O. Reuven, T. Scaffidi, A. Stern, A. K. Geim, and S. Ilani, Imaging hydrodynamic electrons flowing without Landauer–Sharvin resistance, Nature **609**, 276 (2022).

[95] A. Aharon-Steinberg, T. Völkl, A. Kaplan, A. K. Pariari, I. Roy, T. Holder, Y. Wolf, A. Y. Meltzer, Y. Myasoedov, M. E. Huber, B. Yan, G. Falkovich, L. S. Levitov, M. Hücker, and E. Zeldov, Direct observation of vortices in an electron fluid, Nature **607**, 74 (2022).

[96] Z. T. Wang, M. Hilke, N. Fong, D. G. Austing, S. A. Studenikin, K. W. West,

and L. N. Pfeiffer, Nonlinear transport phenomena and current-induced hydrodynamics in ultrahigh mobility two-dimensional electron gas, Phys. Rev. B **107**, 195406 (2023).

[97] A. D. Levin, G. M. Gusev, A. S. Yaroshevich, Z. D. Kvon, and A. K. Bakarov, Geometric engineering of viscous magnetotransport in a two-dimensional electron system, Phys. Rev. B **108**, 115310 (2023).

[98] M. Shavit, A. Shytov, and G. Falkovich, Freely flowing currents and electric field expulsion in viscous electronics, Phys. Rev. Lett. **123**, 026801 (2019).

[99] B. N. Narozhny, Hydrodynamic approach to two-dimensional electron systems, Nuovo Cim. **45**, 661 (2022).

[100] A. Stern, T. Scaffidi, O. Reuven, C. Kumar, J. Birkbeck, and S. Ilani, How electron hydrodynamics can eliminate the Landauer-Sharvin resistance, Phys. Rev. Lett. **129**, 157701 (2022).

[101] K. Bennaceur, C. Lupien, B. Reulet, G. Gervais, L. N. Pfeiffer, and K. W. West, Competing Charge Density Waves Probed by Nonlinear Transport and Noise in the Second and Third Landau Levels, Phys. Rev. Lett. **120**, 136801 (2018).

[102] Gabriele F. Giuliani, and John J. Quinn, Lifetime of a quasiparticle in a two-dimensional electron gas, Phys. Rev. B **26**, 4421 (1982).

[103] C. B. Beauchamp, S. Dimitriadis, J. T. Nicholls, L. V. Levitin, A. J. Casey, P. See, G. Creeth, J. Waldie, I. Farrer, H. E. Beere, and D. A. Ritchie, Superconductivity in AuNiGe Ohmic contacts to a GaAs-based high mobility two-dimensional electron gas, Appl. Phys. Lett. **117**, 162104 (2020).

[104] L. V. Levitin, T. Theisen, S. Dimitriadis, M. Lucas, A. D. Corcoles, J. Nyéki, A. J. Casey, G. Creeth, I. Farrer, D. A. Ritchie, J. T. Nicholls, and J. Saunders, Cooling low-dimensional electron systems into the microkelvin regime, Nat. Commun. **13**, 1-8 (2022).

[105] T. Kawamura and S. Das Sarma, Phonon-scattering-limited electron mobilities in $Al_xGa_{1-x}As$/GaAs heterojunctions, Phys. Rev. B **45**, 3612 (1992).

[106] J. E. Avron, R. Seiler, and P. G. Zograf, Viscosity of quantum Hall fluids, Phys. Rev. Lett. **75**, 697 (1995).

[107] S. Pu, M. Fremling, and J. K. Jain, Hall viscosity of composite fermions, Phys. Rev. Res. **2**, 013139 (2020).

[108] M. Shavit, A. Shytov, and G. Falkovich, Freely flowing currents and electric field expulsion in viscous electronics, Phys. Rev. Lett. **123**, 026801 (2019).

[109] Songci Li, Alex Levchenko, and A. V. Andreev, Hydrodynamic thermoelectric transport in Corbino geometry, Phys. Rev. B **105**, 125302 (2022).

[110] A. Levchenko, S. Li, and A. V. Andreev, Hydrodynamic magnetoresistance in graphene Corbino devices, Phys. Rev. B **106**, L201306 (2022).

[111] V. Gall, B. N. Narozhny, and I. V. Gornyi, Electronic viscosity and energy relaxation in neutral graphene, Phys. Rev. B **107**, 045413 (2023).